Strongly-interacting Fermions in an Optical Lattice

by

Jit Kee Chin

B.S., Physics (2001)
California Institute of Technology

Submitted to the Department of Physics
in partial fulfillment of the requirements for the degree of

Doctor of Philosophy

at the

MASSACHUSETTS INSTITUTE OF TECHNOLOGY

August 2007

Author .....
Department of Physics
August, 2007

Certified by .....
Wolfgang Ketterle
John D. MacAurthur Professor of Physics
Thesis Supervisor

Accepted by .....
Thomas J. Greytak
Professor of Physics, Associate Department Head for Education

Strongly-interacting Fermions in an Optical Lattice

by

Jit Kee Chin

Submitted to the Department of Physics
on August, 2007, in partial fulfillment of the
requirements for the degree of
Doctor of Philosophy

Abstract

Two sets of studies are described in this thesis. The first describes studies conducted with sodium Bose-Einstein condensates (BEC) while the second focuses on the pairing of fermionic lithium-6 pairs in an optical lattice within the strongly interacting BEC-BCS regime. Common to both sets of studies is the use of a magnetically tunable Feshbach resonance to manipulate interactions between the atoms.

In the first experiment, we destabilize a sodium BEC by switching its interactions from repulsive to attractive and studied the resulting dynamics. A local amplification of low momentum energetic instabilities was observed and the measured rate of amplification agreed well with theoretical predictions. For large condensates, this process depleted the condensate faster than the global inward collapse.

Subsequently, I describe the major construction effort that was undertaken to convert our BEC machine to a two-species machine capable of cooling fermionic lithium-6. Upon its completion, we obtained a resonance superfluid of loosely bound ^{6}Li pairs in the BEC-BCS crossover. When placed in a shallow optical lattice, long range phase coherence of this resonance superfluid was inferred from the presence of sharp interference peaks after ballistic expansion. With this observation we have obtained the first evidence of superfluidity of fermions in an optical lattice. A loss in phase coherence occurred when the lattice depth was increased past a critical value, possibly signaling a transition to an insulating state. Further preliminary explorations of this novel system is described followed by an outline of its potential for studying condensed matter phenomena like high temperature superconductivity.

Thesis Supervisor: Wolfgang Ketterle
Title: John D. MacAurthur Professor of Physics

To my father
the original Dr. Chin

and my mother,
who reared two more

And to my sister, who laughed at us all

Acknowledgments

I am deeply grateful to my advisor, Wolfgang Ketterle, for having faith in me and giving me the opportunity to work in his lab. His boundless optimism throughout my PhD was a reliable beacon that always illuminated the way forward, even when things seemed grim. I am also grateful to Dave Pritchard, who was a second unofficial authority in the hallway, and who was always willing to listen.

Thanks to those who preceded me in lab and showed me the ropes - Johnny Vogels, Takashi Mukaiyama, Jamil Abo-Shaeer and Kaiwen Xu. In particular, Johnny Vogels was a very generous mentor. Thanks also to Claudiu Stan, who taught me how to appreciate all things mechanical. Together, we started the machine conversion that enabled my thesis work. I am forever grateful for his endless patience and pedagogy, and for his timely friendship.

Dan Miller was always capable of putting lab life in its proper perspective, constantly leavening it with comic antics. His "outside-the-box", yet critical thinking was invaluable to the lab's progress, and his wisdom kept the lab cohesive. Together with Yingmei Liu, whose efforts in lab inspired us all to work harder, the three of us shared the thrills and satisfaction of chasing down the fast moving frontier of cutting edge research. When laser followed by vacuum followed by power supply followed by slower coil windings took their turn to test our experimental capabilities, we would look at each other, shrug, swill beer at the Miracle before rolling up our sleeves and getting down to business. Bonds forged under such conditions are not forgotten easily. Also not easily forgotten are the practical jokes, Google Earth, the Daily Show and late night 7-eleven runs. Widagdo (Weebs) Setiawan was the fourth Musketeer, not quite full time in the lab, but his presence was nonetheless deeply felt. His inquiring mind kept us on our toes, and his infatuation with all things digital kept us well-supplied with computers.

Christian Sanner joined two years ago, and the lab has been richer in serenity ever since. Wiser than his years, he took over the running of the lab with quiet efficiency. I particularly admire his fine tastes in movies, and his ability to make sense of the most obscure electronic problems. Aviv Keshet, followed by Ed Su joined the lab in subsequent years, and I've enjoyed working with them both. With Aviv around, I have no doubt the reservoir of lab humor will never run dry. Thanks Aviv, for the elephant.

For the first few years of my doctorate, Carol Costa was a motherly and caring figure in the hallway who could solve any administrative problem we brought her. Though she is no longer with us, her memory remains. Other friendly faces in the hallway provided both a community and technical assistance when necessary and include members of both the Ketterle and Vuletic group. Christian Schunck could always be relied on for a sunny smile, and was never too busy to lend a hand. Tom Pasquini made sure we all had health

insurance, and with whom I shared many a coffee and reflections on grad school while we were both writing up. Also Marko Cetina and Monika Schleier-Smith - one enriched my cultural paucity, the other my health. Elsewhere, the women in physics group at MIT was the conduit for many a friendship - in particular Michelle Povinelli and Bonna Newman.

Outside the lab, I happily whiled away the bulk of my twenties with a bunch of exceptional people: my roommates - Hui, Caroline and later Maylee; the longtime inhabitants of Hurley Mansion - Victor, Matteo and Cornelius. Also Seb, Raf, Manu and Eva. The ladies Julija, Aidita, and Neema. The refuge across the river and its occupants - Mirko, Natasa and Gojko. ECF 2007 - you know who you are. I am richer for the long summer evenings spent on an old wooden deck in Cambridgeport, a perfect road trip to Acadia, endless parties (with table) in an even older apartment in East Cambridge, the Green St Girls, learning about and cheering all events sporting, one rainy Christmas in London, getting lost in Ixtapaluca, Mexico and smoke-wreathed evenings engaging in speculation without reason, And I shall not forget my old friends Sam, Kathryn, Derrick, Ushma, Ania and Rick, who saw me off to grad school a long time ago with all their best wishes and good cheer. Here at the finish, I am glad to report that their blessings have been effective.

Unique amongst them all is Zoran Hadzibabic. He has been with me all these intense years, gifting me with priceless laughter and never-ending conversations. Through his looking-glass, I glimpsed a life less ordinary, but well worth living. I shall always cherish this vision.

Finally, this thesis is dedicated to my family. My father set me down this path before I ever knew that a future lurked behind the next transitory excitement, and he shepherds me still. However, nothing would have worked without my mother, with her discipline and unconditional love. My sister and brother-in-law kept me from starving over the past six years, and tolerated my shenanigans with long-suffering sighs. It's meant a lot for me to get know my sister again, after spending our teenage years far apart. My brother has grown up mostly out of sight, but his infectious grin and perky emails were like zephyrs from home, always cheering me up and always reminding me from whence I came.

This work was supported by the Army Research Office (ARO), the Defense advanced Research Projects Agency (DARPA), the National Science Foundation (NSF), the National Aeronautics and Space Administration (NASA), and the Office of Naval Research (ONR).

Contents

List of Figures

List of Tables

Chapter 1

Introduction

1.1 The allure of high temperature superconductors

Nothing better illustrates how deeply a scientific concept has penetrated the popular imagination than its ubiquitous presence in science fiction. Superconductivity is one such concept - its history is littered with Nobel prizes and Hugo awards alike. A superconductor supports current flow without dissipation, wasting no energy in the form of heat. This conceptual simplicity and its rich technological possibilities lends itself easily to futuristic visions of the world and emphasizes its potential applications.

In fiction, temperature is often a conveniently ignored detail. In reality, the first transition to the superconducting state was observed by Kamerlingh Onnes to happen in mercury at $T_c = 4.2$ K in 1911, for which he was awarded the Nobel prize in 1913. This was far too low for practical applications and for many decades, known T_c's stayed below 23 K. Fast forward to 1986, when Bednorz and Mueller [1] discovered high temperature superconductivity in a ceramic cuprate material with $T_c = 35$ K, and its significance was immediately acknowledged by a Nobel prize in 1987. Shortly thereafter, a similar material with $T_c = 92$ K was found, attaining an important practical milestone: cooling can now be done cheaply with liquid nitrogen at 77 K. The highest transition temperatures of these "high Tc" superconductors climbed quickly in the following decades, to stand now at 138 K. Clearly, another important milestone would be reached if a room temperature superconductor were to be discovered or constructed.

Yet to this day, the theory of high T_c stands incomplete. The complexity of real condensed matter systems makes them difficult to treat theoretically, yet without a good understanding, the search for ever higher T_c can only proceed through trial and error. Lately however, a new frontier has opened up - if we begin thinking about generalized charge carriers and artificial crystals, fresh angles with which to attack the problem began to appear.

Enter cold gases.

1.2 Of bosons and fermions...

When Bose and Einstein first demonstrated in 1924 that non-interacting, indistinguishable bosons could condense into the same quantum state [2, 3], it had merely been an idealized exercise in statistical mechanics and no one suspected the far-reaching ramifications. Everyone knew that electrons - the charge-carrying particles - were fermions and therefore forbidden to occupy the same quantum state. This made them ineligible for Bose condensation. It wasn't until 1935 that Fritz London linked superconductivity to Bose-Einstein condensation [4] .

The difference between bosons and fermions can be related to a simple sign change in the exchange symmetry of the wavefunction. If two particles A and B are identical, then the probability of finding particle A in state 1 and particle B in state 2 has to be equal to the probability of the converse. Their wavefunctions obey

$$|\psi(a_1, b_2)|^2 = |\psi(b_1, a_2)|^2 \tag{1.1}$$

$$\Rightarrow \psi(a_1, b_2) = \pm\psi(b_1, a_2) \tag{1.2}$$

By stipulating indistinguishability, all particles are grouped into two classes: bosons (plus sign) and fermions (minus sign). From quantum field theory, the fundamental property that is responsible for this difference in the exchange properties was identified as spin - bosons have integer spin, while fermions have half-integer spin. This gives rise to an additional constraint for fermions. Following eq. 1.2, the situation where two fermions occupies the same state implies

$$\psi(a_1, b_1) = -\psi(a_1, b_1) \tag{1.3}$$

$$\Rightarrow \psi(a_1, b_1) = 0 \tag{1.4}$$

Clearly, this is forbidden. This is known as the Pauli exclusion principle and it underpins the behavior of all matter, ranging from the everyday observation that matter occupies space, to the periodic table structure of elements.

However, if there exists many more accessible states than there are fermions or bosons, the difference in their quantum statistics would not manifest itself. Which is why in our everyday experience, both kinds of particles behave classically. It is not until the number of energetically available states become comparable to the number of particles do we begin to discern a difference and enter quantum degeneracy.

Bose-Einstein condensates (BEC)

For bosons, no constraint against occupying the same state exists and at zero temperature large numbers of particles do end up in the ground state of the system. In other words, at low temperatures the wavefunctions of particles begin to overlap and the particles are no longer separable. The temperature at which this phase transition occurs can be estimated by setting the spatial extent of the particle's wavefunction $\lambda_{dB} = \frac{h}{\sqrt{2\pi m k_B T}}$, to be equal to the interparticle spacing $n^{-1/3}$. This gives

$$T_c \sim \frac{2\pi\hbar^2}{k_B m} n^{2/3} \tag{1.5}$$

In other words, these bosons have become degenerate and are considered "condensed".

The observation of Bose-Einstein condensation of dilute atomic gases in 1995 [5, 6] was preceded by breakthroughs in laser cooling of atoms and heralded a new era in the research of cold gases. The promise of atomic systems lay in its simplicity - compared to traditional condensed matter systems, dilute gases were simpler to model and easier to control. Interactions were typically weak and easily incorporated as a perturbation. In addition, they opened up previously inaccessible parameter space, providing a new way of testing the validity of various theories.

Bardeen, Cooper and Schrieffer (BCS)

Due to Pauli exclusion, quantum degeneracy of ideal fermions at zero temperature manifests itself differently. As temperature is lowered, they will successively fill each available state beginning from the ground state, until all the fermions are accommodated. The highest filled level is known as the Fermi energy E_F, which depends only on the density of states and the number of fermions. Unlike the situation for bosons, the transition into quantum degeneracy is smooth for ideal fermions and a good way of measuring degeneracy is to define the relative "coldness" temperature T/T_F, where $T_F = E_F/k_B$.

The situation becomes much more interesting once we consider interactions. Fermions are unstable at $T = 0$ against the addition of the slightest attractive interactions, preferring to pair to lower their energy. This is the famous Bardeen-Cooper-Schrieffer state, named after they who first wrote down its wavefunction. In this state, the pairing is weak and long range, with the attractive interaction provided by the crystal lattice vibrations.

Driven by an interest in simulating real materials, efforts to cool fermions to quantum degeneracy began soon after the successful condensation of bosons. Fermions are inherently harder to cool than bosons, since the Pauli exclusion principle meant that interactions between identical fermions could not be exploited for cooling purposes. However, this restriction can be lifted by either using bosons as a 'refrigerant', or by cooling non-identical

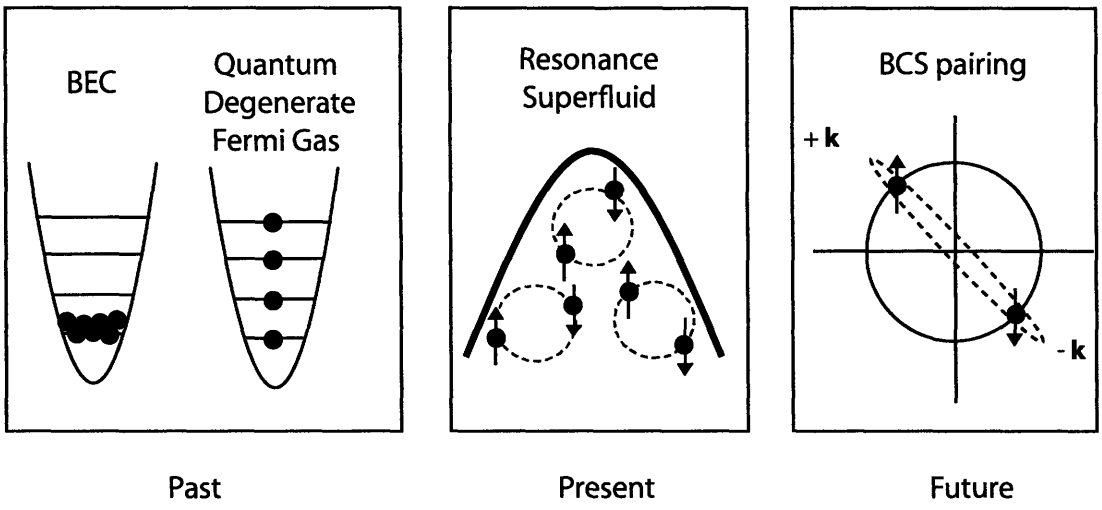

Figure 1-1: In 1995 and 1999, quantum degeneracy of ultracold Bose and Fermi gases was achieved, strikingly demonstrating the difference in quantum statistics between the two kinds of particles. Further innovations in fermion cooling led to the achievement of a "resonance superfluid" in 2003, comprising of fermions paired up at intermediate distances (see text). The goal of the future is to observe long range BCS pairing, where fermions close to the Fermi surface are correlated in momentum space, and to obtain insight into superconductivity.

fermions together. Using the latter method, a quantum degenerate Fermi gas was observed in 1999 [7] by using fermions in two different states.

1.3 ...and everything in-between

While neutrons, electrons and protons are all fermions with spin 1/2, two fermions tightly bound together behaves like a boson. Therefore what determines whether any given atom ends up as depends on the sum of its constituents particles - odds fermions, even bosons.

All atomic bosons are fermionic composites. The fermions are so tightly bound together that their individual behavior is irrelevant when viewed from a distance. This suggests that the barrier between the two classes of particles is not insurmountable. If two fermions can be persuaded to pair, we recover the physics of bosons. Cooper pairs of fermions correlated in momentum space which can bose-condense is an example of bose-fermi physics.

BEC-BCS crossover

One can imagine how in the limit of extremely high density, the slightest attraction between fermions would result in pairing [8]. In practice, it is easier to keep density constant and vary the strength of the attraction, induced by bringing in a two-body bound state (Feshbach resonance, see Chapter 2). Then there exists a smooth crossover between tightly bound molecules and long-range Cooper pairs [9], and in 2003, the first experiments within this crossover were reported [10, 11, 12, 13, 14]. Performed in the intermediate regime where the molecular size was on par with the interparticle spacing, these experiments highlighted the dual nature of particles within the crossover, where neither pure bosonic or fermionic physics was sufficient for complete understanding. Fermion pairs could condense, both where a true two-body bound state existed [10, 11, 12], and where it did not [13, 14], yet in both cases, the levels of the harmonic trap would be filled up to the Fermi surface.

1.4 Optical lattices, low dimensions and the cuprates

Thus stands the complicated story of bosons and fermions. There is much to understand and investigation is ongoing, but new challenges arise. Having created a resonance superfluid in bulk phase, we now ask how its behavior changes when placed in a non-trivial environment.

That the environment is crucial in determining the physics of ultracold atoms is not new. In BEC's, a simple harmonic trap confining the atoms modifies the density of states sufficiently to allow for condensation in two-dimensions where none was possible before [15, 16]. In one-dimension, a lineup of bosons where hopping across particles is not allowed results in the system taking on fermionic characteristics (Tonks gas) [17]. One of the most startling work comes from loading bosons in a periodic potential, and observing self-ordering of the atoms from a superfluid to an insulating state [18].

The idea is to model as closely as possible the situation in the superconducting cuprates, where square crystal lattices in two-dimensions are weakly linked together (Fig. 1-2). It is suspected that the mechanism that gives rise to their high transition temperature is dependent on its crystal structure. In atomic physics, nearly perfect periodic structures of many different geometries may be engineered through clever interference of light. By placing cold fermions within these structures, we reproduce the physics of electrons in a crystal, with the added advantage of having tunable effective inter-and intra-well interactions. This, combined with the new parameter space and observation tools that this system makes available, explains its widespread appeal. Through its study, we hope to move closer to the long-term goal of not only understanding, but perhaps also engineering a room-temperature superconductor.

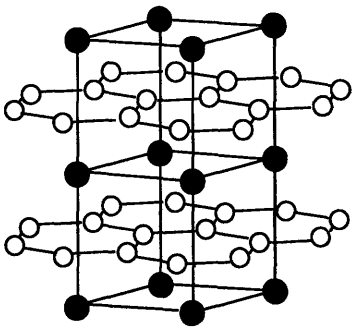

Figure 1-2: Crystal structure of a high Tc superconductor.

1.5 Outline

This thesis is comprised of two sections. The first section chronicles my apprenticeship in the techniques of manipulating ultracold gases and consists of experiments performed using bosons. The second section is the main focus of this thesis, documenting our efforts to build an apparatus capable of reaching the current frontier in ultracold fermion research, followed by a series of experiments on resonance superfluids in an optical lattice.

Chapter 2 gives an overview of the Feshbach resonance, an anomaly in the scattering properties that we use to tune interatomic interactions and a common theme of all the experiments documented in this thesis. Here I also give the technical details of manipulating and improving our magnetic field stability, which was necessary for working within the resonance. Chapter 3 describes how a Feshbach resonance is used to destabilize a sodium BEC by switching its interactions from repulsive to attractive, and documents one mechanism that contributes to the resulting condensate decay (publication reprinted in Appendix A). Not elaborated upon here is the subsequent series of experiments on sodium molecules formed near another Feshbach resonance [19, 20, 21], where the improved field control played a crucial role. Full descriptions are provided in the theses of Jamil Abo-Shaeer [22] and Kaiwen Xu [23], and the first of these publications are attached in Appendix C.

The latter half describes our progress in the much less well-understood regime of strongly-interacting, quantum degenerate fermions confined in optical lattices. The optical lattice setup was first set up to study the behavior of bosonic sodium in a periodic potential [24, 25], before we decided to use it to study fermions instead. Chapter 4 gives a brief theoretical overview of fermi physics, and Chapter 5 describes the two-species machine-building effort. With its completion, we were in the enviable position of possessing the sole apparatus capable of loading long-lived fermion pairs into a three-dimensional optical lattice. Chapter 6

discusses some peculiarities of this system we had to understand and overcome and chapter 7 presents the first evidence of superfluid pairing of ultracold fermions in an optical lattice. In a neat reversal, the optical lattice was then used as a tool to study the superfluid transport of the paired fermions. Blueprints and technical details for the machine is included in Appendix D and publication reprints are included in Appendices E and F.

Since this is very much a work in progress, this thesis wraps up with a lengthy chapter 8 exploring the behavior and potential of this system before concluding in chapter 9. Some intriguing initial observations about our system as well as long-term goals will be discussed.

Chapter 2

Feshbach Resonances

Feshbach resonances have become ubiquitous as a tool for tuning the scattering properties of ultracold atoms. In fact, it is the common thread that ties together the disparate parts of my thesis. This chapter gives a brief introduction and provides technical details of the magnetic field stabilization that was implemented in order to work near the Feshbach resonances of both ^{6}Li and ^{23}Na .

2.1 What is a Feshbach Resonance

In 1962, Herbert Feshbach predicted the presence of scattering resonances in nuclear physics [26]. Since then, it has found wide application in atomic physics and many excellent references has been written [27]. A Feshbach resonance occurs when the energy of the open scattering state is made to match that of a bound state, and a coupling exists between the two. Various means for inducing Feshbach resonances have been suggested, encompassing the use of radio-frequency fields [28], dc electric fields [29], optical fields [30] and magnetic fields. While both photoassociative [31] and magnetic Feshbach resonances [32] have now been observed, only the latter is relevant for this thesis. It works by exploiting the difference in the total magnetic moments of the open and bound states, bringing them into resonance at certain magnetic fields (see Fig. 2-1). Atoms in the open channel can then scatter into the intermediate bound state, before transitioning back to the open channel again.

2.1.1 The open channel

s-wave scattering length

In ultracold gases, two neutral atoms interact via the van der Waal's potential $V = -C_6/r^6$. Scattering is then dominated by spherically symmetric s-wave scattering if the particles are not identical fermions, since the energies involved are typically too low to allow significant

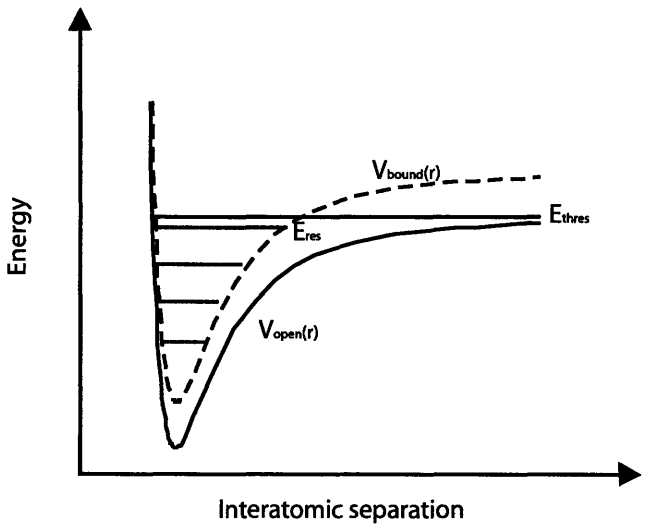

Figure 2-1: An s-wave feshbach resonance occurs when a level crossing between a bound and open scattering channel happens for certain values of the magnetic field. For ultracold collisions, the kinetic energy in the open channel is negligible.

higher partial-wave scattering. In this limit, the net effect of the central potential with range r_0 on an atom at distance $r > r_0$ is merely to bring about a constant phase shift in the asymptotic wave function. From scattering theory, this phase shift is given by

$$\delta = -\frac{ka}{1+ika} \tag{2.1}$$

where we have defined an s-wave scattering length a such that when ka is small, it completely parameterizes the scattering (see Fig. 2-2). The scattering amplitude f and hence cross-section σ can also be determined from Eq. 2.1 to be

$$f = \delta/k \tag{2.2}$$

$$d\sigma = |f|^2 d\Omega \tag{2.3}$$

$$\Rightarrow \sigma = 4\pi a^2 \tag{2.4}$$

Close to a Feshbach resonance, the bound state affects the open channel atoms by adding to this phase shift, since atoms can now accumulate additional phase shifts while temporarily residing in the bound state. From second order perturbation theory, the modification of the s-wave scattering length would follow (neglecting contributions from other bound states that are far-detuned)

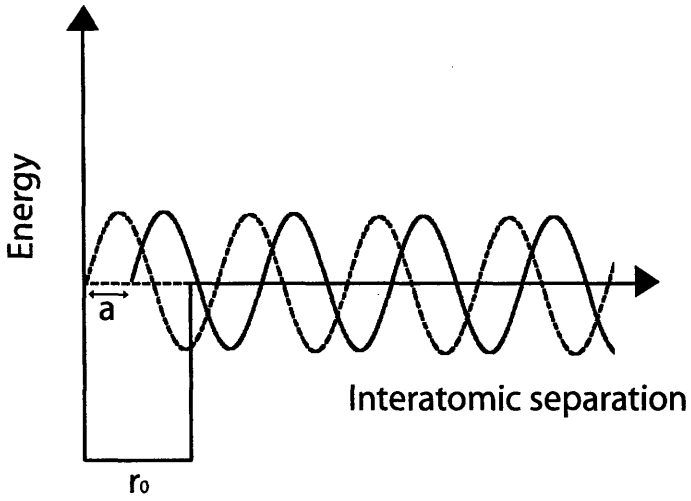

Figure 2-2: Relation between phase shifts and s-wave scattering lengths. For simplicity, we have neglected the $1/r$ decay of the wavefunction. Dashed line gives the wavefunction for $V = 0$, while solid line depicts the asymptotic wave-function for a square well potential of finite depth V. For $r < r_0$, the wavefunction depicted is an extrapolation of its asymptotic form since details at $r < r_0$ is unimportant for the long-range behavior.

$$a \sim \frac{C}{E_{thres} - E_{res}} \tag{2.5}$$

It follows that when $E_{res} > E_{thres}$, corresponding to a virtual bound state, $a < 0$ and when $E_{res} < E_{thres}$, corresponding to a real bound state, $a > 0$. This distinction becomes important in Chapter 6, where we discuss the pairing of fermions in the vicinity of a Feshbach resonance.

This microscopic description of the interatomic interactions may be parameterized in terms of the experimentally accessible magnetic field as

$$a(B) = a_0 \left(1 - \frac{\Delta B}{B - B_0}\right) \tag{2.6}$$

where a_0 is the background (unperturbed) scattering length far away from the Feshbach resonance, B_0 the position of the resonance and ΔB the width of the resonance (effective range over which resonant scattering dominates). Eq. 2.6 clearly demonstrates how the atom-atom scattering properties can be tuned at will in the vicinity of a Feshbach resonance.

2.1.2 The closed channel

In addition to its effect on the open channel, the bound molecular state is also interesting in its own right. If a significant and stable population of the bound state can be engineered from an ultracold atomic sample with no or little increase in the temperature, then we have succeeded in performing 'quantum chemistry'. Ultracold molecules formed this way neatly circumvents the traditional difficulty of laser cooling of molecules arising from their complicated energy structure. The first direct observation of ultracold molecules produced this way comprised of fermionic ^{6}Li [33] and shortly thereafter we successfully produced ultracold bosonic ^{23}Na molecules [19]. Since Feshbach resonances between different atomic species also exists, one can imagine forming ultracold hetero-nuclear molecules, with direct application to various topics, for example the search for a permanent electric dipole moment [34].

However, dimers formed in the vicinity of a Feshbach resonance are in the highest ro-vibrational state. If their constituent atoms are bosons, this state is unstable against collisions, which are greatly enhanced when a is large. As a result, they quickly decay into deeper bound states tightly localized with size R_0, releasing a correspondingly large kinetic energy $\approx \hbar^2/mR_0^2$ in the process. This energy is carried away by the colliding atoms, which heat and leave the system. This is the source of the inelastic losses first used to infer the presence of Feshbach resonances in bosons [32].

For dimers with fermionic constituents, the atom-dimer collisional relaxation is suppressed close to the resonance, since in order to collide, all three particles need to come

close together but two out of the three participants will be identical and this is forbidden by Pauli exclusion. This significantly lengthens the lifetime of such dimers, making them a better candidate for studies of pairing as well as for down-conversion into the ground state.

2.2 Manipulating Interatomic Interactions

Theoretical calculations for the approximate locations of the ^{23}Na and ^{6}Li Feshbach resonances were done by [35, 36], and the first experimental observations reported in [32] and [37] provided a more accurate determination. Table 2.2 lists the Feshbach resonances for ^{23}Na and ^{6}Li .To utilize Feshbach resonances however, one has to have very good control of the magnetic fields. There are two practical conditions to fulfill:

1. If electromagnets are used (almost always true to enable fast dynamic control), there has to be sufficient capacity in the Feshbach coils to access the resonance. For resonances occurring at high fields (true for both ^{23}Na and ^{6}Li), the coils must either be very close to the position of the atoms, or have very high current-carrying capacity.

2. The stability of the magnetic field has to be such that there is sufficient resolution within the width of the Feshbach resonance, on top of the resonance position. As we will see, this can impose a requirement of better than 4 orders of magnitude stability in the current, a performance not easily achieved by off-the-shelf power supplies.

In the following section, I will give details of the modifications to our machine that was necessary to work close to resonance. While this section is highly technical, it is meant to serve as a future reference. Since the modifications were made throughout my graduate career and put into place whenever the need arose, I will indicate where each scheme was used where appropriate.

2.2.1 Electromagnet configuration

Fig. 2-3 shows the geometry of our modified Ioffe-Pritchard type magnetic trap. It consists of four main pairs of coils: the pinch coils which provide axial curvature, the ioffe bars which provide radial gradient, the anti-bias coils which cancel out the high bias fields provided by the curvature coils, and the bias coils, wound concentrically with the anti-bias coils, which provide additional bias fields when needed. Further details regarding the magnetic trap can be found in Dallin Durfee's thesis [40].

When accessing the Feshbach resonances in ^{23}Na and ^{6}Li , the atoms are trapped using optical fields, thereby freeing up the coils for Feshbach manipulation. Parallel currents running in Helmholtz configuration in the bias and anti-bias coils provide bias fields at a

^{23}Na

$\|F, m_F\rangle$	$\|m_J, m_I\rangle$	$B_0(G)$	ΔB (G)
$\|1,1\rangle$	$\|-1/2, 3/2\rangle$	853	1
$\|1,1\rangle$	$\|-1/2, 3/2\rangle$	907	1
$\|1,-1\rangle$	$\|-1/2,-1/2\rangle$	1195	4

^{6}Li

$(\|F, m_F\rangle, \|F, m_F\rangle)$	$(\|m_J, m_I\rangle, \|m_J, m_I\rangle)$	$B_0(G)$	ΔB (G)
$(\|1/2,1/2\rangle, \|1/2,-1/2\rangle)$	$(\|-1/2,1\rangle, \|-1/2,0\rangle)$	834.149	300
$(\|1/2,1/2\rangle, \|3/2,-3/2\rangle)$	$(\|1/2,1/2\rangle, \|3/2,-3/2\rangle)$	690.43	122.3
$(\|1/2,-1/2\rangle, \|3/2,-3/2\rangle)$	$(\|1/2,-1/2\rangle, \|3/2,-3/2\rangle)$	811.22	222.3

Table 2.1: s-wave Feshbach resonances for ^{23}Na (intra-state) [32, 38] and ^{6}Li (inter-state) [39]. Intra-state s-wave Feshbach resonances for ^{6}Li do not exist due to Pauli exclusion. The scattering states are labelled by both their $|F, m_F\rangle$ and their $|m_J, m_I\rangle$ numbers - the latter are good quantum numbers at the high magnetic fields of Feshbach resonances while the same is true for the former at low magnetic fields where we trap and cool.

rate of 2.5 G/A, (1 G/A for bias coils, 1.5 G/A for anti-bias coils). Each coil is water cooled and capable of supporting 500 A of current. Together they can easily reach magnetic fields in the vicinity of 1200 G and they are referred to as the Feshbach coils. Additional current in the pinch coils can add a small amount ($\approx$ 10 G) to this value.

Nested within the pinch coils is the rectangular glass cell where all trapping, cooling, and manipulation of the atoms take place. The glass cell is suspended between two bellows, and the coils are clamped to aluminum bars surrounding the glass cell. The mounting of these coils is neither rigid enough to withstand fast field ramps, nor perfect enough to ensure a uniform bias field. The former problem gives rise to mechanical vibrations when the current in the coils are ramped quickly, resulting in more background noise when we take an absorption image of the atoms (see Widagdo Setiawan's thesis [41] for detailed analysis). The latter problem gives rise to radial field gradients when only a uniform bias field is desired. This problem is addressed by winding an additional coil and inserting it off center to the pinch coils (nulling coil in Fig. 2-3). By judicious manipulation of the current in the nulling coil and the pinch coils (to offset axial gradients introduced), the magnetic field can be made free of gradients at the location of the atoms.

2.2.2 Stabilization of Feshbach fields (^{23}Na)

The widest Feshbach resonance in ^{23}Na is found at 1195G resonance, with a width of a few Gauss. In order work within the resonance with reasonable resolution, it is necessary to stabilize the magnetic field to sub-Gauss precision, i.e. a part in 10^4. Rapid switching and control of the magnetic field was also necessary to avoid collisional decay for the series of

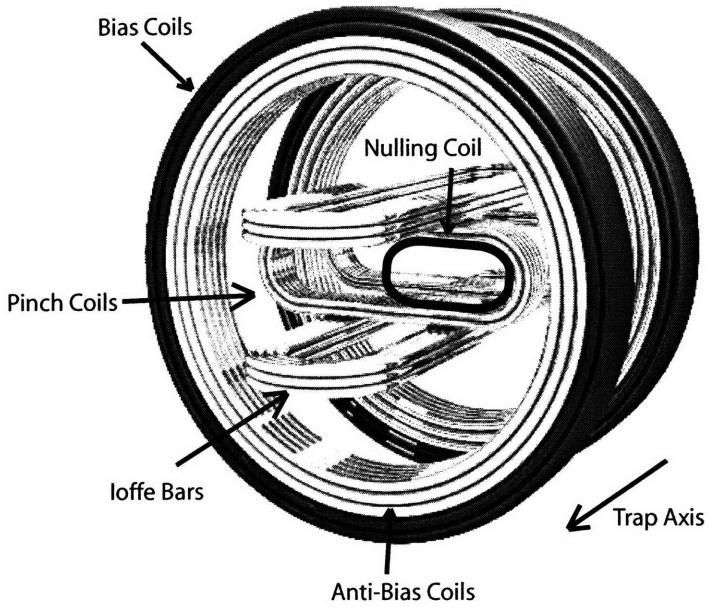

Figure 2-3: Modified Ioffe-Pritchard style trap. Also shown is the additional off-axis field-nulling coil used to correct for radial gradients at the high bias fields during Feshbach resonances.

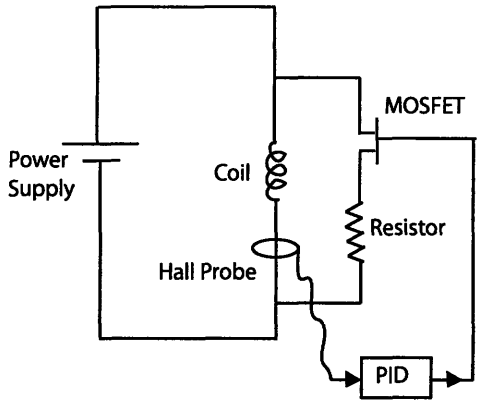

Figure 2-4: Magnetic field stabilization for ^{23}Na Feshbach work using shunt currents. This scheme was used for the work reported in Appendix C

experiments with quantum degenerate ^{23}Na molecules.

The stabilization scheme used was modeled after that described by Brian deMarco in his thesis [42]. A fast servo on each one of the Feshbach coils can be achieved by shunting out a few amps of current in a bypass circuit (see Fig. 2-4) and changing the effective resistance by operating a MOSFET in the analog region. A closed loop Hall probe measured the currents going through the coils and the signal compared to the desired setpoint. A simple PID circuit then drove the gate voltage of the analog MOSFET, which actually consisted of an array of high power, thin film MOSFETs, wired in parallel and mounted on a copper heatsink.

Without active stabilization of the shunt current, the DC peak-to-peak ripple (V_{pp}) of the bias coils in current control mode was measured to be about 1A, with similar performance in the anti-bias coils. After the bypass stabilization, V_{pp} was reduced to 200mA. The transient response to sudden induced emf (tested by switching off current in the pinch coils, a step necessary for our experiments) improved from a sharp dip of 1A and a recovery time of 7ms, to a recovery time of 2ms with no change in the amplitude of the dip. This stabilization circuit was used for the work described in [19], included here in Appendix C.

Drawbacks of the shunt current stabilization include a daily drift of the setpoint needed to achieve a fixed current, as well as the relatively poor transient response. Further improvement of the stabilization scheme was achieved by implementing a total current servo on the bias coil by using an IGBT as a variable resistor (see Fig. 2-5) and operating the power supply in voltage control mode.

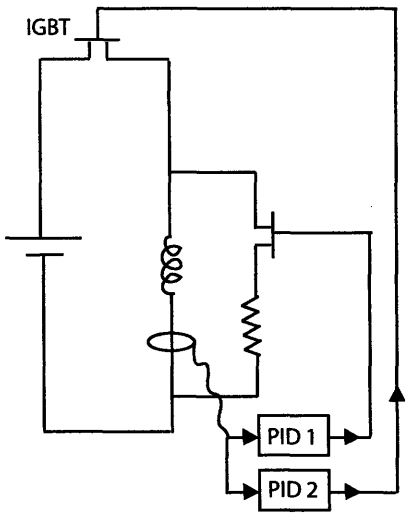

Figure 2-5: Magnetic field stabilization for ^{23}Na Feshbach work using shunt and total current control. This scheme gave the best transient response for the field (see Fig. 2-6)

With just the total current servo, recovery time improved to 500 μs with no change in the transient amplitude. However, fast oscillations on the order of 10kHz was seen during the transient. With both total and shunt current servo in place, the fast oscillations were servoed out, with no change in the transient recovery time or amplitude response. In DC mode, V_{pp} was reduced to less than 33mA, and the slow drifts of the setpoint was eliminated.

To a large extent, the total current servo acts as a slow control knob, with the shunt servo acting as a fast, fine control. The improvement in the transient response is summarized in Fig. 2-6. Altogether, the performance of our magnetic field has improved by an order of magnitude, allowing us to perform field-sensitive experiments.

2.2.3 Stabilization of Feshbach fields (^{6}Li)

One problem remains. Since the bias and anti-bias coils were wound concentrically and driven by separate power supplies, their mutual inductance was very large and fluctuations in one invariably affected the other. This crosstalk made stabilizing out current fluctuations at the same time very tricky. Therefore, when the scientific focus of the lab was changed to fermions, a major reconfiguration of the coils was done.

Feshbach resonances in ^{6}Li are quite different from those of ^{23}Na (for a discussion on exactly how unusual the situation in ^{6}Li is, see [43]). Between the two lowest hyperfine states of ^{6}Li there exists a 300G wide Feshbach resonance centered at 834G. This meant that fast transient response was no longer necessary since switching the pinch coils would only

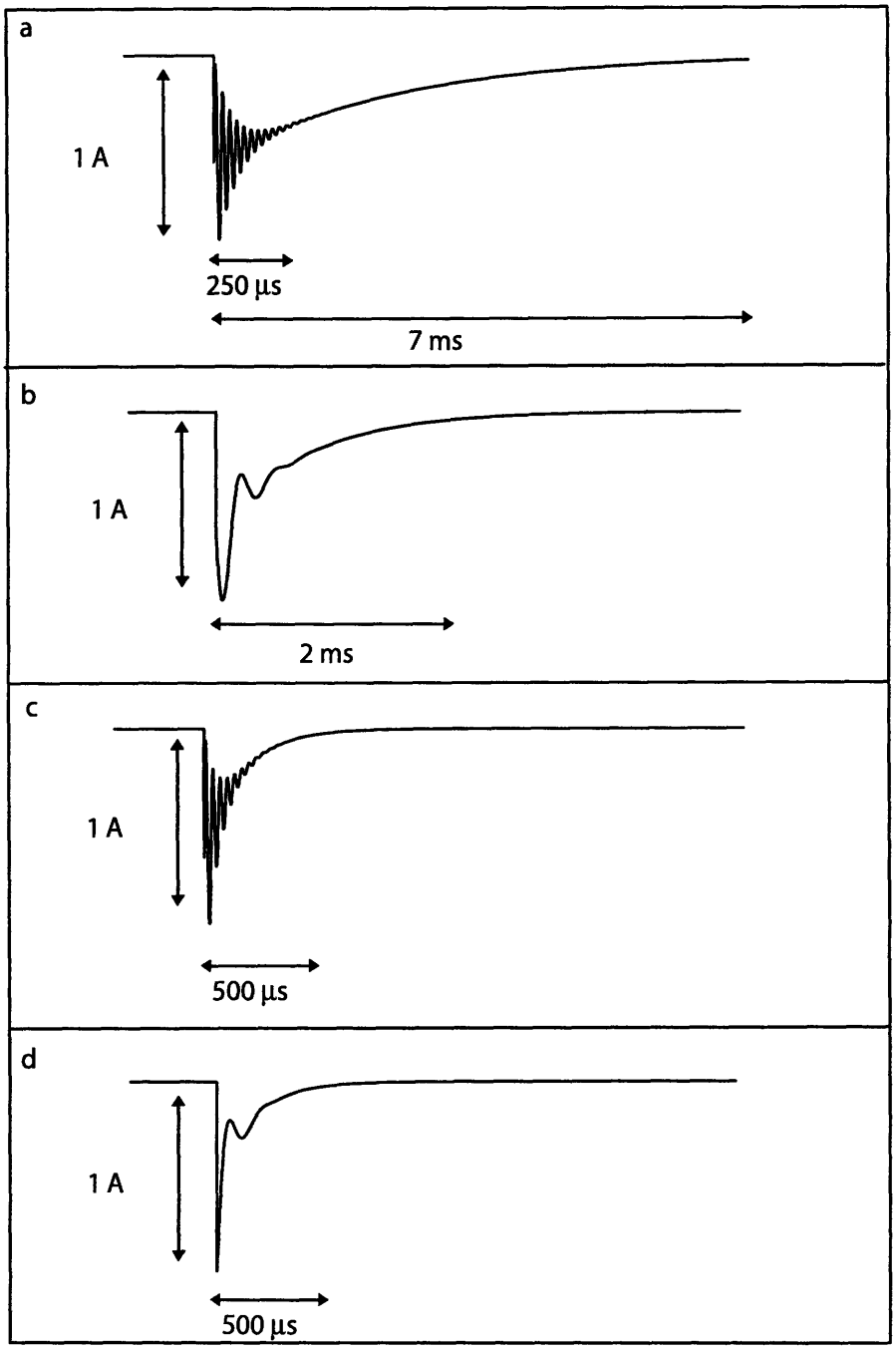

Figure 2-6: The characteristic transient response of the Feshbach coils under different stabilization schemes are shown here (not to scale). The baseline is set by panel (a), where no active stabilization is used. Panel (d) shows the best performance, with both total and shunt current stabilization. Panel (b) and (c) are the intermediate results, with just shunt and just total current stabilization respectively.

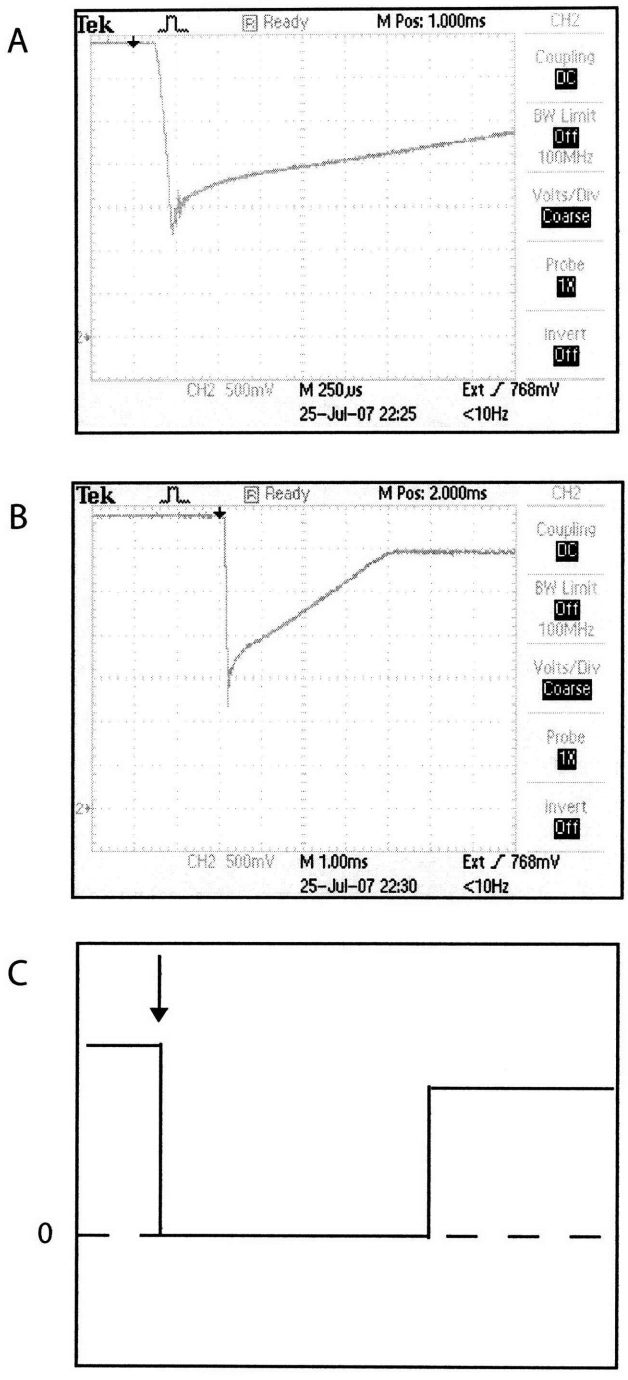

Figure 2-7: Scope trace from the current monitor of the Feshbach coils. Here, 500mV $\equiv$ 50A $\simeq$ 125G. Trigger indicates when the control sequence begins to ramp. (A) shows a close up of the initiation of the field ramp, including a slight (100 μs) delay before the analog IGBT begins to clamp the current. This delay varies from shot to shot, and is not controllable. Field ramps down $\approx$ 500 G in 100 μs. (B) shows the full ramp, where it takes 4 ms to ramp up $\approx$ 400 G. (C) shows the sequence we would like to have, where field ramps take no time.

produce a change in magnetic field of a few Gauss, which would not change the scattering length significantly. For the same reason, the requirement for DC stability was also relaxed. Instead, we now needed to change the field quickly by a few hundred Gauss.

The system was improved and simplified by rewiring the coils such that a single dedicated power supply drove both the bias and anti-bias coils. The power supply used was an ESS 30-500 model from Lambda, capable of going up to 500 A of current or a maximum voltage of 30V. While we were now limited by the voltage to running only 450A through both coils, it was still sufficient for our needs (see Appendix D for wiring diagram). Active total current stabilization was implemented to ensure rapid control over the magnetic field while an additional feedback path to the voltage control of the power supply ensured that the analog IGBT regulating the total current was never dissipating too much heat [44]. In effect, the analog IGBT now served as the fast servo, while the voltage control of the power supply served as the slow servo. The bypass MOSFETs previously used for ^{23}Na were no longer necessary and were taken out.

Chapter 3

Bose Einstein Condensates with Attractive Interactions

Interactions in any given atomic species depends only on its internal structure and varies greatly. Without tunability, the only option is to switch atomic species each time a different interaction is desired. The first two alkali species to be cooled and Bose-condensed in 1995 both had repulsive interactions [5, 6]. The first alkali species with attractive interactions to be successfully cooled to condensation was ^{7}Li, in 1997 [45]. As we shall see, cooling, with its accompanying enhancement of phase space density, is more difficult for atoms with attractive interactions and only small samples could be obtained. Beyond that, instability of the atom cloud and loss invariably occurred.

BEC's with attractive interactions have been likened to supernovas [46], in spite of the vast differences in length, time and energy scales. The stabilizing and destabilizing forces are now given by quantum degenerate fermi pressure and gravitational attraction respectively, but both systems possess the same stability criterion. By creating an attractive BEC and watching it decay, it can be said that one has simulated an astrophysical event in the lab.

Since the observation of magnetically tunable Feshbach resonances in 1998 [32], the number of experimental testing grounds for attractive atoms have multiplied. Now large condensates could first be formed with repulsive interactions before switching to attractive interactions using the resonance. In this chapter, I will describe our studies of large sodium BEC's with attractive interactions. At the time, the steady state properties of an attractive BEC was already fairly well-understood. Debate centered instead around the loss dynamics when the system became unstable. Many processes are likely to play a part [47, 48] but we focus on the role of amplified local instabilities [49]. Our experiment was reported in:

J.K. Chin, J.M. Vogels and W. Ketterle, "Amplification of Local Instabilities in a Bose-Einstein Condensate with Attractive Interactions, Phys. Rev. Lett. **90**" *160405 (2003)*

[50]. Included in Appendix A.

3.1 Mean-Field Interactions

In dilute gases, the length scales of the system are almost always well separated, with

$$r_0(\text{sub nm's}) << a(\text{nm's}) << n^{-1/3}(\text{sub } \mu\text{m}) \tag{3.1}$$

where r_0 is the effective range of the interatomic potential and $n^{-1/3}$ gives interparticle spacing. This simplifies the determination of the interactions considerably, since atoms that spend most of their time far apart do not care much about the details of short-range scattering. A pseudopotential that reproduces the long-range scattering length a can then be constructed, and takes the form of a zero-range delta function potential $V(\mathbf{r}) = U_0\delta(\mathbf{r})(\delta/\delta r)r$, where

$$U_0 = \frac{4\pi\hbar^2}{m}a \tag{3.2}$$

In turn, the many-body interaction can be approximated by averaging the two-body effective interactions of all other atoms (so called Hartree-Fock approximation), since the diluteness condition implies that all three and higher-order scattering is very unlikely. This constant mean-field term is given by $U = nU_0$, and appears in the Gross-Pitaevskii equation governing the evolution of a BEC as

$$-\frac{\hbar^2}{2m}\nabla^2\psi(r) + V(r)\psi(r) + U_0|\psi(r)|^2 = \mu\psi(r) \tag{3.3}$$

where $V(r)$ is the external trapping potential and μ the chemical potential.

3.2 Steady-state Behavior

In the simplest case, $V(r) = 0$, and the kinetic energy term is small for a large homogeneous condensate. The GP equation then reduces to

$$U_0|\psi(r)|^2 = \mu\psi(r) \tag{3.4}$$

leading to a trivial condition for stability. If $a > 0$, the interactions are repulsive and the BEC is stable. If $a < 0$, the atoms self-attract and implosion of the BEC occurs.

For a trapped BEC in a harmonic potential (by far the most experimentally relevant), it is possible to have a small stable condensate with attractive interactions. In this case, the negative mean-field energy is stabilized by the zero point kinetic energy of the harmonic

potential. For fixed a, the maximum atom number an attractive BEC can support in equilibrium is given by

$$N_{cr} = \frac{k a_{ho}}{|a|} \tag{3.5}$$

where $a_{ho} = \sqrt{\hbar/m\omega}$ is the harmonic oscillator length and k is a stability coefficient that depends on the external trapping frequencies [51]. Condensates of ^{7}Li with a small negative background scattering length of -27 Bohr radii have been made, with $N_{cr} \approx 1250$ atoms [45, 52]. Once the condensates grow larger than N_{cr}, a sharp reduction in the number of atoms via a sudden collapse is seen. The functional form of Eq. 3.5 has also been verified by [53] using ^{85}Rb.

3.3 Dynamics - Local Amplification of Instabilities

Closer study of the dynamics of attractive BEC's have indicated that many processes contribute to condensate decay, including bursts and jets of spin-polarized atoms as well as invisible loss [54]. The former effect is mainly phenomenological and not well explained by any existing theory. On the other hand, the latter has been shown to be due to molecule conversion - i.e. atoms have populated the resonant bound state in the vicinity of the Feshbach resonance, and likely decayed to more deeply bound states subsequently [55].

We add to the discussion by demonstrating yet another mechanism that contributes to the loss of zero-momentum condensate atoms. In 2002, Yurovsky pointed out that large attractive condensates have unstable modes with "imaginary eigenenergies" which undergo exponential growth [49]. Contrary to the global collapse observed in [54], this amplification of instabilities, or "quantum evaporation" for short (to borrow a term from the field of liquid Helium), is a purely local process.

3.3.1 Bogoliubov theory of elementary excitations

Mean-field interactions in a weakly-interacting BEC modify its excitation spectrum and cause it to deviate from ideal gas behavior. In particular, it couples the different free momentum states $p_i's$, such that they are no longer good eigen-states of the system. Bogoliubov theory can be used to find the new eigenstates and eigen-energies of the system, which we outline below:

In second quantized notation, the Hamiltonian for a uniform interacting bose gas system is

$$H = \sum_p \epsilon_p^0 a_p^\dagger a_p + \frac{U_0}{2V} \sum_{p,p',q} a_{p+q}^\dagger a_{p'-q}^\dagger a_{p'} a_p \tag{3.6}$$

where $\epsilon_p^0 = p^2/2m$ and the operators $a_p^\dagger$ and a_p create or destroy one quantum of excitation in the free space momentum mode p, q. By performing the canonical transformation

$$\begin{aligned} b_p^\dagger &= u_p a_p^\dagger + v_p a_{-p} \\ b_p &= u_p a_p + v_p a_{-p}^\dagger \end{aligned}$$

where

$$u_p^2, v_p^2 = \frac{\epsilon_p^0 + n_0 U_0 \pm \epsilon(p)}{2\epsilon(p)}$$

the Hamiltonian becomes diagonal again in the new Bose operators $b_p^\dagger$ and b_p, with eigenenergy

$$\epsilon(\mathbf{p}) = \sqrt{\frac{|\mathbf{p}|^2}{2m}(2n_0 U_0 + \frac{|\mathbf{p}|^2}{2m})} \tag{3.7}$$

The "good modes" $b_p^\dagger$ and b_p are now superpositions of the free particle operators $a_p^\dagger$ and a_p. For each free momentum state $p \neq 0$, the ground state population $\langle a_p^\dagger a_p \rangle$ is finite, and given by v_p^2 (see Appendix B). This occupation of non-zero momentum states in the ground state of an interacting BEC is known as quantum depletion.

3.3.2 Qualitative predictions

From Eq. 3.7, we can deduce most of the qualitative results from a few basic principles.

Exponential growth of unstable modes

Imaginary $\epsilon(p)$ exist for all negative U_0, given arbitrarily low momentum $\mathbf{p}$. For these modes, the time evolution governed by $\exp[i\epsilon/\hbar t]$ goes from stable oscillatory behavior to exponential growth as U_0 becomes more negative.

Number squeezing

Momentum conservation demands that the increase in atom number in each $+p$ mode be accompanied by a corresponding increase in each $-p$ mode.

Depletion of the condensate

The zero momentum state condensate is increasingly depleted due to number conservation.

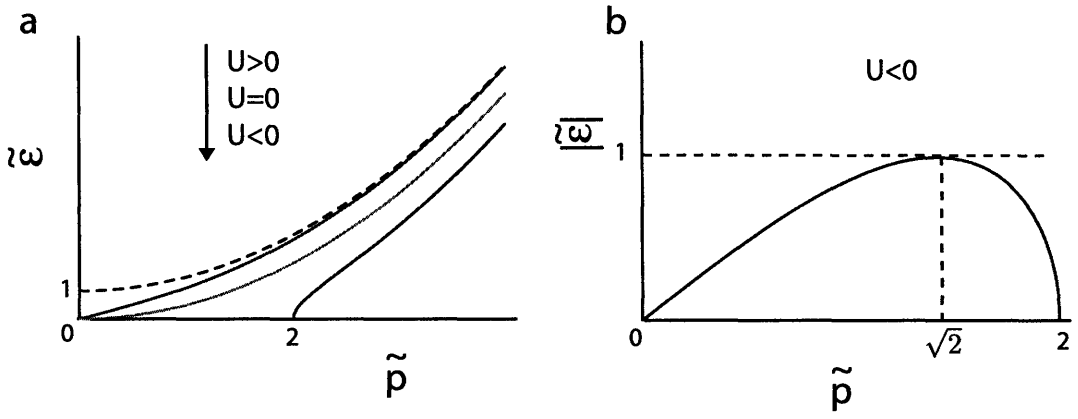

Figure 3-1: (Color in electronic version) Panel (a) shows the dispersion relation (Eq. 3.7) for $U > 0$ (red), $U = 0$ (green) and $U < 0$ (blue) plotted in dimensionless energy and momentum units ($\tilde{\varepsilon} = \frac{\varepsilon}{U}$, $\tilde{p} = \frac{p}{mc}$, $c = \sqrt{\frac{U}{m}}$). Dashed line shows the asymptotic form for $U > 0$, where the extrapolation down to $p = 0$ shows an energy offset equal to U. When $U < 0$, there exists real eigen-energies only for $\tilde{p} > 2$. Panel (b) shows the behavior of $|\tilde{\varepsilon}(\tilde{p})|$ when it becomes imaginary. As discussed, all modes with $\tilde{p} < 2$ will grow exponentially. For a fixed negative a, there exists a mode $|p|$ which has maximum growth rate.

3.4 Experiment

For a real system, $V(r)$ is never zero. However, the previous formalism still holds as long as the sample is large and the density does not vary quickly across the length of the sample. This is valid as long as the interactions U is much greater than the zero-point motion $\hbar\omega$ of the atoms (often called the Thomas-Fermi regime [56]). The experiment described below makes use of large sodium BEC's which are well in this limit. The gist of is given in the publication [50], reproduced here in Appendix A, and only the highlights and some details will be provided here.

3.4.1 Mode selection

We isolate a single mode for observation in order to obtain a clear signature of quantum evaporation. Experimentally, it is much easier to change U_0 than $|\mathbf{p}|$, so the condition for unstable modes becomes $|U_0| > |\mathbf{p}|^2/4mn_0$ for fixed $|\mathbf{p}|$. A small population is seeded in a low momentum mode p before switching on the attractive interactions, thus favoring its growth over the others. The growth of the $-p$ mode then provides an unambiguous visualization of the process (see Fig. 3-3).

A two-photon Bragg process (Fig. 3-2) was used as the seeding mechanism. Two light beams with momentum $\mathbf{k}_1$ and $\mathbf{k}_2$ and energy difference $\hbar\Delta\omega$ are incident upon the atoms

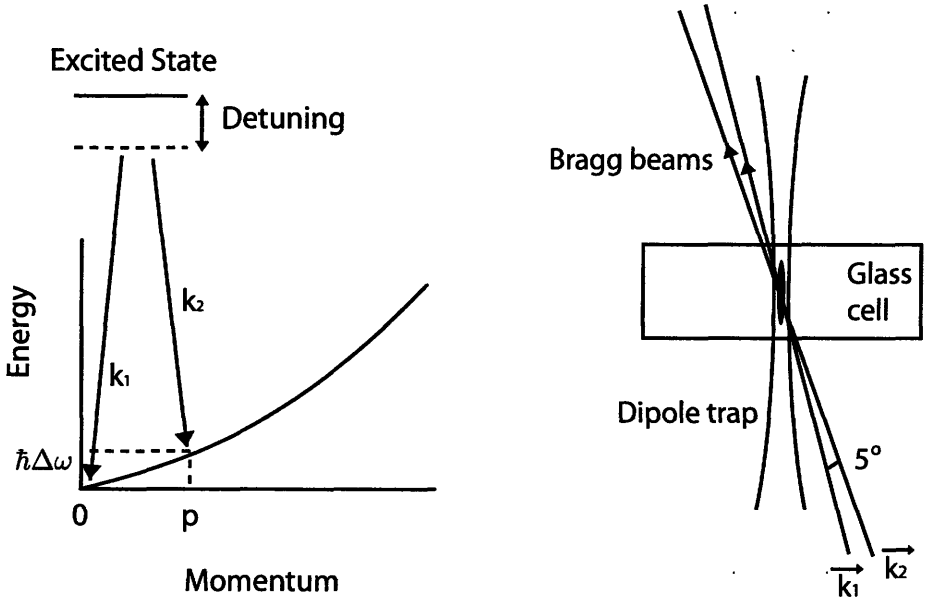

Figure 3-2: Shown on the left is the dispersion for a BEC with $U > 0$ (from Eq. 3.7) together with the energy matching condition for two-photon Bragg scattering. This process is used to preselect a mode for observation of quantum evaporation. Shown on the right is the corresponding experimental setup. For clarity, the Bragg beams are drawn as vectors with infinitesimal width. In actuality, their beam waists were fairly wide and encompassed the length of the BEC. Effort was made to have $\Delta\mathbf{k} = \mathbf{k_1} - \mathbf{k_2}$ to be predominantly in the radial direction of the BEC. For optical access reasons, the orientation of $\mathbf{k_1}$ was limited to 15^o to the long axis.

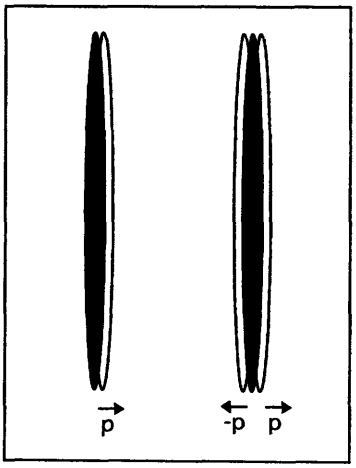

Figure 3-3: The expected momentum of the phonon amplification scheme. The appearance of the $-p$ momentum component provides a clear qualitative signature of quantum evaporation, and the separation of both momentum components from the zero momentum condensate makes it possible to quantitatively track its evolution.

initially at zero momentum. For given $p = \hbar(k_1 - k_2)$, if the energy matching condition $\Delta\omega = \varepsilon(p)$ is satisfied, then atoms will be transferred from the zero momentum state to the p momentum state. The duration and intensity of the light beams determine the rate and selectivity of the transfer, and a large detuning ensures only virtual population in the excited state. For a more complete description, please see the thesis of Daniel Miller [57]

3.4.2 Direct determination of scattering length

In order to make quantitative comparisons with theory, it was necessary to obtain a very good measurement of the scattering length in the vicinity of the Feshbach resonance. Traditionally the signature for Feshbach resonance, inelastic loss did not directly yield a value for the scattering length, which was rather inferred from calculated widths.

A novel scheme for directly measuring the negative scattering length was implemented by using a blue-detuned laser that acts to repel atoms via the AC Stark shift (see section 7.2). Fig. 3-4 illustrates how this works. The force produced by the anti-trapping optical potential compensates for the attractive interaction and helps stabilize the condensate. From this we can extract the scattering length a:

$$a \propto F_{attractive} = F_{repulsive} \propto I \tag{3.8}$$

where I is the intensity of the antitrap. By only assuming the form of Eq. 2.6 and the high field background scattering length of $a_0 = 3.3$ nm [58], the scattering length is completely determined by the variation of I vs magnetic field for any given field.

3.4.3 Observations

The resulting observation of quantum evaporation (Fig. 3-5) agreed well with theoretical estimates of the evaporation rate as well as the minimum $|a|$ required for instability to set in.

3.5 Analysis

Here we give details of the analysis not covered in [50]. Ideally, the formal expression for the evolution of an unstable mode p is given by [49]

$$\langle \xi^\dagger_{\mathbf{p}} \xi_{\mathbf{p}} \rangle(t) = \frac{|U|^2}{\hbar^2 \lambda^2(\mathbf{p})} \sinh^2[\lambda(\mathbf{p})t] \tag{3.9}$$

where $\lambda(\mathbf{p}) = |\epsilon(\mathbf{p})|/\hbar$ and we have used $\xi^\dagger_p, \xi_p$ to denote the creation and annihilation operators of the unstable free momentum states $a^\dagger_p, a_p$, in line with the notation in [49]. Modifications to this expression due to seeding a small population v^2 and initial quantum

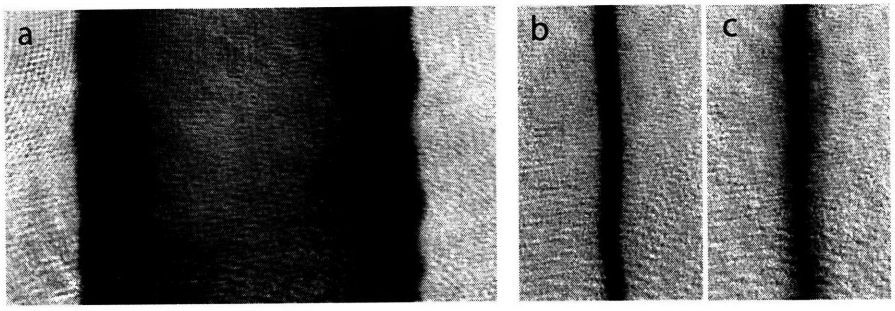

Figure 3-4: Absorption images reveal the effect of a blue detuned laser beam on a BEC with attractive interactions. Accurate alignment was achieved by making sure the atoms with $a > 0$ were evenly split after holding in the anti-trap for 2 ms (a). When $a < 0$, the application of the anti-trap stabilizes the global contraction of the condensate (b), which would begin to shrink otherwise (c).

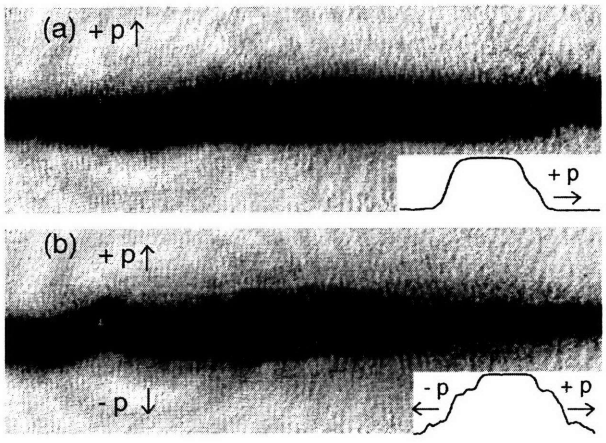

Figure 3-5: Observation of quantum evaporation. Insets show the density profile of a radial slice through the condensate. In (a), a condensate with $a > 0$ has been seeded with a small population in momentum state p. In time-of-flight, atoms in state p move out of the condensate in a predominantly radial direction. In (b), the interactions in the condensate has been switched to $a < 0$ after seeding momentum state p. Now $\pm p$ components are seen, with higher population than the initial seed in the $+p$ momentum state.

depletion of the condensate can be obtained by evaluating $\langle v^2|\xi_p^\dagger(t)\xi_p(t)|v^2\rangle$, beginning with the previously derived time-evolution of the annihilation operator (see Appendix B),

$$\xi_p(t) = (\cosh[\lambda(p)t] - i\frac{d(p)}{\lambda(p)}\sinh[\lambda(p)t])\xi_p(0) - i\frac{U}{\hbar\lambda(p)}\sinh[\lambda(p)t]\xi_{-p}^\dagger(0) \tag{3.10}$$

where the detuning $d(p) = (\frac{p^2}{2m} + U)/\hbar$ and the coupling is given by $U/\hbar$.

3.5.1 Seeding

In this case, the mode p has initial population v^2 with all other modes having population zero:

$$\begin{aligned}
\langle v^2|\xi_p^\dagger(t)\xi_p(t)|v^2\rangle &= \left(\cosh^2[\lambda(p)t] + \left(\frac{d(p)}{\lambda(p)}\sinh[\lambda(p)t]\right)^2\right)v^2 + \frac{U^2}{\hbar^2\lambda^2(p)}\sinh^2(\lambda t) \\
&= v^2\left(1 + \sinh^2(\lambda t) + \left(\frac{d(p)}{\lambda(p)}\sinh[\lambda(p)t]\right)^2\right) + \frac{U^2}{\hbar^2\lambda^2(p)}\sinh^2(\lambda t) \\
&= \left(1 + \frac{g^2(p)}{\lambda^2(p)}\sinh^2(\lambda t)\right)v^2 + \frac{U^2}{\hbar^2\lambda^2(p)}\sinh^2(\lambda t) \\
&= v^2 + (v^2+1)\frac{U^2}{\hbar^2\lambda^2(p)}\sinh^2(\lambda t)
\end{aligned}$$

Note that $\lambda^2(p) + d^2(p) = U^2/\hbar^2$. As expected, the rate of growth does not change. Instead, there is merely an offset corresponding to the initial seed population, and an enhancement of the population in the seeded mode vs. unseeded modes by a factor (v^2+1).

3.5.2 Quantum Depletion

The effects of quantum depletion is more complicated, since now all modes are initially populated. Since all the modes are also coherent, the phase correlations can interfere either constructively or destructively to affect the evolution. We simulate the effect of quantum depletion in Fig. 3-6 using our experimental parameters and include the full calculation in Appendix B. We see that the growth of the unstable mode actually slows down due to quantum depletion.

However, the total fraction of quantum depleted atoms in a BEC with density n_0 can be estimated by $\eta_0 = 1.505\sqrt{n_0 a^3}$ [25]. For our parameters, this gives a quantum depleted fraction of $0.5 \approx 1\%$, and we conclude that its effect is negligible.

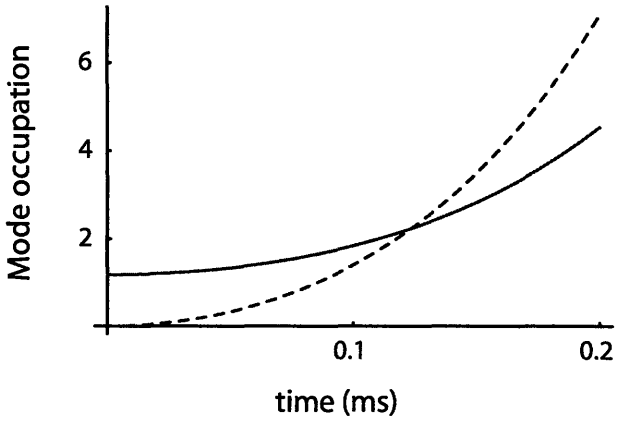

Figure 3-6: (Color in electronic version) Solid (red) curve shows the exponential growth of a mode p with finite initial population due to quantum depletion. Dashed (blue) curve shows the growth without quantum depletion (Equation 3.9).

3.5.3 Contribution to condensate decay

Finally, we place quantum evaporation in context amid the other decay processes by considering their respective time scales. In particular, we will compare it to global collapse. Since the rate of quantum evaporation is a predominantly local effect, we expect that it will dominate when the condensate is large enough for the Thomas-Fermi approximation to apply. Conversely, if the condensate is small, the local description is invalid and global collapse occurs. This is also supported by our observations.

Chapter 4

Quantum Degenerate Fermions

The rest of this thesis will focus on work done with ultracold fermions and this chapter gives a brief overview of the quantum degenerate fermi gas.

4.1 Non-interacting spin-polarized gas of fermions

To a very good approximation, a spin-polarized gas of ultracold fermions is non-interacting, since Pauli-exclusion forbids their interacting via symmetric s-wave collisions and higher partial wave scattering is inhibited due to the low energies. This makes theoretical calculations simple and exact.

4.1.1 Zero temperature description

At $T = 0$, the expression for Fermi energy and distribution for an ideal Fermi gas may be derived from the fully-filled Fermi sea distribution function: $f(\mathbf{r}, \mathbf{p}) = 1$ if $p \leq p_F$ (or equivalently if $E_{total}(r, p) \leq E_F$) and is zero otherwise. In a harmonic trap with spherical trapping frequencies $\omega_{x,y,z} = \omega$, all distribution functions can be derived from the pair of equations

$$\frac{\hbar^2 k(\mathbf{x})^2}{2m} + \sum_i \frac{1}{2} m\omega^2 x_i^2 = E_F \tag{4.1}$$

$$n(\mathbf{r}) = \int_{k<k_F} \frac{d^3k}{(2\pi\hbar)^3} f(\mathbf{r}, \mathbf{p}) \tag{4.2}$$

Then the spatial distribution $n(\mathbf{r})$ and the local Fermi energy $\epsilon(\mathbf{r})$ defined in terms of the local Fermi wavevector $k_F(\mathbf{r})$ becomes

$$n(\mathbf{r}) \quad = \quad \frac{1}{6\pi^2} k_F(\mathbf{r})^3 \tag{4.3}$$

$$= \frac{1}{6\pi^2}k_F^3\left(1-\sum_i \frac{x_i^2}{R_i^2}\right)^{3/2} \tag{4.4}$$

where (4.5)

$$\epsilon_F(\mathbf{r}) = \frac{\hbar^2 k_F(\mathbf{r})^2}{2m} \tag{4.6}$$

$$= E_F - V(\mathbf{r}) \tag{4.7}$$

Eq. 4.4 is known as the Thomas-Fermi distribution where E_F is the Fermi energy. For a total number of particles N, E_F only depends on the number of fermions and the trapping potential as

$$N = \int d^3r n_F(\mathbf{r}) \tag{4.8}$$

$$= \frac{1}{6}\left(\frac{E_F}{\hbar\overline{\omega}}\right)^3 \tag{4.9}$$

or alternatively, $E_F = (6N)^{1/3}\hbar\overline{\omega}$, corresponding to $k_F = \sqrt{2mE_F/\hbar^2}$ at the center of the trap where $V = 0$, and the spatial extent of the cloud in the trap is given by the Thomas-Fermi radius $R_i = \sqrt{\frac{2E_F}{m\omega_i^2}}$. For a homogeneous system, the local Fermi energy and wavevector is just E_F and k_F.

4.1.2 Finite temperature

For a finite temperature analysis of the properties of a non-interacting Fermi gas, we turn to Fermi-Dirac statistics. In a semi-classical description, the Fermi distribution function in a harmonic potential can be written as

$$f(\mathbf{r},\mathbf{p}) = \frac{1}{\exp[\beta(\mathbf{p}^2/2m + V_{ho}(\mathbf{r}) - \mu)] + 1} \tag{4.10}$$

where $\beta = k_B T$, μ is the chemical potential and $V_{ho} = \sum 1/2m\omega^2\mathbf{r}^2$. The spatial distribution is given by integrating over the momentum p, giving

$$n(\mathbf{r}) = \frac{1}{2\pi\hbar^3}\int d^3p f(\mathbf{r},\mathbf{p}) \tag{4.11}$$

$$= -\frac{1}{\lambda_{dB}^3}\mathrm{PolyLog}(3/2, -e^{(\mu - V(\mathbf{r})/k_B T)}) \tag{4.12}$$

where (4.13)

$$\mathrm{PolyLog}(n,\lambda) = \frac{1}{\pi^n}\int d^{2n}\frac{1}{e^{r^2}/\lambda - 1} \tag{4.14}$$

is a a standard integral, and $\lambda_{dB} = \sqrt{\frac{2\pi\hbar^2}{mk_B T}}$ is the de Broglie wavelength. The total number of particles may be recovered by integrating over the remaining spatial coordinates, giving

$$N = \int d^3 r n(\mathbf{r}) \tag{4.15}$$

Using a convenient property of the PolyLog functions,

$$\int \text{PolyLog}(n, \lambda e^{-x^2}) = \sqrt{\pi}\text{PolyLog}(n + 1/2, \lambda) \tag{4.16}$$

the total number of particles may be expressed as

$$N = -\left(\frac{k_B T}{\hbar\omega}\right)^3 \text{PolyLog}(3, -e^{\mu/kBT}) \tag{4.17}$$

When $T \to 0$, there is no drastic change in the distribution function. Instead, it smoothly interpolates from a classical gaussian shape to a PolyLog function before finally reaching the Thomas-Fermi profile (Eq. 4.4) at zero temperature.

4.1.3 Time of flight

By definition, a non-interacting gas expands ballistically in time-of-flight. The spatial distribution can then be obtained by making the substitution

$$x_i(t) \to \frac{x_i(0)}{\sqrt{1 + \omega_i^2 t^2}} \tag{4.18}$$

$$V \to \frac{V}{\Pi_i \sqrt{1 + \omega_i^2 t^2}} \tag{4.19}$$

leading to an expression for the spatial distribution $n(\mathbf{x}, t)$

$$n(x,t) = -\frac{1}{\lambda_{dB}^3} \frac{1}{\Pi_i \sqrt{1 + \omega_i^2 t^2}} \text{PolyLog}_{3/2}(-e^{-\beta(V-\mu)}) \tag{4.20}$$

4.2 Interacting two-component fermions

When we have a mixture of fermions in two different spin states, s-wave scattering between them is permitted, and we have to include interactions. Of these, attractive interactions are the most interesting since they give rise to pairing. For convenience, the two different spin states are often referred to as spin-up ($\uparrow$) or spin down ($\downarrow$). For repulsive interaction, the qualitative behavior in the bulk phase does not change even at zero temperature.

4.2.1 Weak attractive interactions - BCS state

For weak interactions where the range of the interactions a is much smaller than the interparticle spacing $n^{-1/3}$, the ground state of the system can be solved [59] and corresponds to the famous BCS state first introduced to describe superconductivity. It turns out that the three-dimensional Fermi sea is unstable even against the weakest attractive interactions, preferring to form bound states (Cooper pairs) with exponentially small binding energy. The pairs can then Bose-condense at a critical temperature given by

$$T_c \approx 0.28 T_F e^{\pi/2k_F a} \tag{4.21}$$

This superfluid Fermi gas exhibits frictionless flow, due to the presence of a finite gap Δ_{gap} in the single-particle excitation spectrum

$$\epsilon(k) = \sqrt{\Delta_{gap}^2 + [\hbar v_F(k - k_F)]^2} \tag{4.22}$$

$$\text{where} \tag{4.23}$$

$$\Delta_{gap} \approx 1.76 k_B T_c \tag{4.24}$$

For realistic values of $k_F a$, the transition temperature for dilute gases quickly becomes very small, making observation of the true BCS state difficult.

4.2.2 Strong interactions - Unitarity

One obvious solution is to increase $k_F a$. Naively, we would expect T_c to approach $0.28 T_F$ when $1/k_F a$ tends towards zero. However, when a diverges in the vicinity of a Feshbach resonance, the gas is no longer weakly interacting and standard derivations of BCS theory are no longer valid. On resonance, a greatly exceeds all other length scales in the problem and the only length scale left is the interparticle spacing $n^{-1/3}$. This is known as the unitarity regime.

Within this regime, the corresponding energy scale must be the Fermi energy $\epsilon_F = \frac{\hbar^2}{2m}(6\pi^2 n)$. The chemical potential of the gas is then ϵ_F times a universal constant:

$$\mu = \xi \epsilon_F \tag{4.25}$$

Calculations of ξ [60] are being constantly refined as new measurements are made [61, 62, 63], but it is approximately

$$\xi \approx 0.45 \tag{4.26}$$

In a harmonic trap, the spatial distribution of the cloud in the unitarity regime again must have the Thomas-Fermi profile (Eq. 4.4) except now we substitute in the chemical potential

μ for the total energy E_F. Then the Thomas-Fermi radius becomes $R_{TF} = \sqrt{2\mu/m\omega^2}$ and normalization to the total number of particles yields

$$\mu = \sqrt{\xi} E_F \tag{4.27}$$

where E_F is again the non-interacting Fermi energy $(6N)^{1/3}\hbar\omega$. The expression for peak density in the Thomas-Fermi profile becomes

$$n_0 = \frac{1}{6\pi^2}\left(\frac{2m\epsilon}{\hbar^2}\right)^{2/3} \tag{4.28}$$

$$= \frac{1}{6\pi^2}\left(\frac{2mE_F}{\hbar^2\sqrt{\xi}}\right)^{3/2} \tag{4.29}$$

A similar argument can be used for the critical temperature in the unitarity regime, asserting that

$$T_c = \alpha T_F \tag{4.30}$$

where α is also a universal dimensionless parameter. Without knowing its precise value, this linear scaling with T_F is already a vast improvement over the exponential suppression with $1/k_F a$ in Eq. 4.21. Experimental observations of condensates in the unitarity regime have placed α to be ≈ 0.2 [14].

Chapter 5

Experimental Setup for cooling ^{6}Li

When the focus switched to studying fermions in optical lattices in 2004, there were already many indications that ^{6}Li would be a good choice. In 2003 - the "Year of the Molecules" - one group after another had successfully obtained fermionic pair condensates [13, 14]. In all these studies, the seconds-long lifetimes of ^{6}Li condensates stood out. The only other fermionic species cooled to condensation, ^{40}K, had much shorter lifetimes of milliseconds [10]. The longer lifetimes allowed for more efficient cooling, and ^{6}Li pair condensates with $T/T_F < 0.05$ were routinely obtained.

In addition, a ^{23}Na -^{6}Li machine had previously been constructed in a neighboring lab (BEC I) with great success [64, 65, 66, 44], and significant in-house expertise had accumulated. This chapter documents our building effort, highlighting peculiarities specific to our machine and provides some useful technical information.

5.1 Light

5.1.1 Power and Frequency Requirements

In laser cooling and trapping (^{6}Li), all optical power considerations begin from the saturation intensity (2.5 mW/cm^2), while frequency considerations stem from the D_2 line cycling transition (671.977 nm) and excited state linewidth (6 MHz). More specifically, the linewidth of the laser needs to be significantly less (< 1 MHz) than the excited state linewidth, and actively locked to the atomic transition.

Additionally, the total desired power is determined by the frequency generation design. We list our requirements below:

1. The MOT is formed from 6 independent beams each with radius 1 cm^2. The independent beam setup mirrors our ^{23}Na MOT setup, and allows for easy MOT optimization. Similarly, the large ^{6}Li beam size matches the beam size for ^{23}Na .

	Power (mW)
MOT	$6\times\pi\times(1\text{ cm})^2 \times 2.5 = 45$
Repump	45
Slower	30
SubTotal	120
Pre-optical fiber (50%)	240
Pre-switching AOM's (80%)	300
Pre-Locking setup + Misc. Inefficiencies (10%)	350
Total power needed	> 350

Table 5.1: Power needed from a ^{6}Li laser source. Efficiencies of various stages are indicated in parentheses.

2. An equal amount of repump and MOT light is needed. Unlike ^{23}Na , repumping ^{6}Li is difficult due to its unresolved excited state (see Fig. 5-2). Because of this, repumping light up to the saturation intensity is needed in all 6 MOT beams.

3. Light delivery to the MOT is decoupled from the laser output and frequency generation table via polarization maintaining, single-mode optical fibers.

4. Acousto-optical modulators (AOM's) are used for fast switching ($< 1\mu$s).

5. 15 mW of light is needed for stable frequency locking using pump-probe spectroscopy. Enough power is needed to obtain saturated absorption features.

These considerations are summarized in Table 5.1 and gives a total power requirement of > 350mW.

5.1.2 Possible laser systems

The possible laser systems considered were:

Distributed low power sources

In a so-called "master-slave" configuration, light from a frequency-locked, low power source (master) is divided up and frequency shifted before acting as a reference for several higher power diodes (slaves). The maximum power obtainable in any one beam is then determined by the power of a single diode. This was the scheme previously used in a separate lab within our group.

However, the availability of high power (50-100 mW) slave diodes is driven by commercial demand (e.g. DVD manufacturers), and fluctuates greatly. As diode technology improved, the available wavelengths kept shifting lower, as shorter wavelength light meant that the density of encoded data could be pushed higher. Wavelengths fell below 671nm, to

peak at about 660 or 650 nm. While heating the laser diodes could shift the lasing frequency by a few nm's, shifting by >10 nm caused too much instability. After testing numerous diodes, we concluded that their performance was inadequate. Moreover, a known problem with multiple slaves was that the probability of any one of them becoming unlocked in a given time period goes up rapidly with the number of slaves.

High power sources

Ideally we would like a single high-power source, capable of hassle-free operation for hours at a time. Options considered include

- **Tapered amplifier**

  This system derives its frequency characteristics from a diode where the linewidth has been narrowed by active feedback. Power is then boosted by injecting the light into a tapered amplifier. One such system was the TA100 with initial power estimates of 250 mW from Toptica Photonics. Though the power was somewhat low for our purposes, it could have been made to work in combination with one slave diode, but finally indefinite delays in the fabrication of the amplifier chip forced us to consider alternatives.

- **Frequency doubled solid state laser**

  Another intriguing option is a solid state, frequency doubled red laser. The Nd^{3+} ion has a secondary lasing line near 1338 nm, which could be temperature tuned to 1343.95 nm, the fundamental wavelength for frequency doubling to 671.977nm (see Fig. 5-1). In principle, such a laser would provide turn-key operation, good stability and a TEM (0,0) mode.

  Crystalaser had some initial success developing this laser in consultation with us. By pumping a $NbVO_4$ crystal at 808 nm and intracavity doubling with an LBO crystal, a preliminary model lasing at 671 nm with 250 mW of power and sub-MHz bandwidth was obtained. Upon testing however, some problems with the continuous frequency-tuning of the laser were discovered. Ultimately, this scheme was also not adopted, although further development could yield a viable model in the future.

5.1.3 Final choice - Dye laser

The final selection of a 699 Coherent Ring Dye laser model was meant to be a temporary solution until better solid state options became available. It ended up staying in place for over two years, until a tapered amplifier system was successfully developed and substituted in (see the undergraduate thesis of Widagdo Setiawan [41]). While no longer in place, the

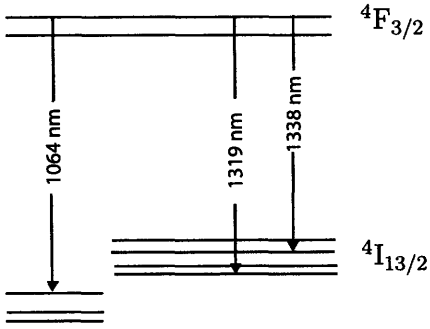

Figure 5-1: Energy levels and the first three lasing lines of Nd^{3+} ion. Strongest emission comes from the 1064 nm line, followed by emission on the 1319 and 1338 nm lines, both with a factor of 5 lower stimulated emission cross sections [67]. In order to have sustained CW emission on the 1338 nm line, the other two have to be suppressed.

dye laser system was used to obtain most of the results reported in this thesis, and I will give a brief description of its operation here. This may also come in useful if an auxiliary tunable red light source is needed for future experiments.

- **Dye recipe** (courtesy of John Thomas): 1g LD688 dissolved in 1 liter of 2-phenoxy-ethanol (EPH) and ultra-sounded overnight, since the dye is only slightly soluble in EPH. Both can be obtained from Exciton Inc, and EPH is additionally available from Penta Manufacturing (preferred).

- **Pump laser**: For good conversion efficiency, the pump should be close to in frequency, but have higher energy than the output. In addition, the transverse spatial mode of the pump beam also has to be perfectly Gaussian. Limited high power options lead to a common choice of green light for the pump. Initially, we used an old Coherent Innova 100 Argon-ion laser. However, a sagging filament in the aging ion tube resulted in a deformed transverse mode and frequent pointing shifts. A newer model of Ar-ion laser - the Saber TSM-15, encountered similar problems. Finally, a solid state Millenia X system from Spectra-Physics with 10W of output power at 532 nm was used.

- **Alignment**: The high viscosity of EPH meant that the jet stream was fairly thick. In addition, the 699 model had old and poorly designed mirror mounts, resulting in a laser that was very difficult to align and optimize. The tweeter mirror focus was a particularly sensitive knob. Small changes could result in dramatic improvement in power and mode.

- **Frequency noise**: Initially, the dye laser exhibited frequency noise at 60 Hz. When viewed on a 300 MHz scanning Fabry-Perot cavity, the sub-MHz linewidth of the light was seen to break up periodically. This noise could also be seen directly - with the laser locked to the reference cavity, the error signal showed jagged structure at 60 Hz. The problem was finally solved by replacing the aging electrolytic capacitors (10mF) that filtered the AC power input.

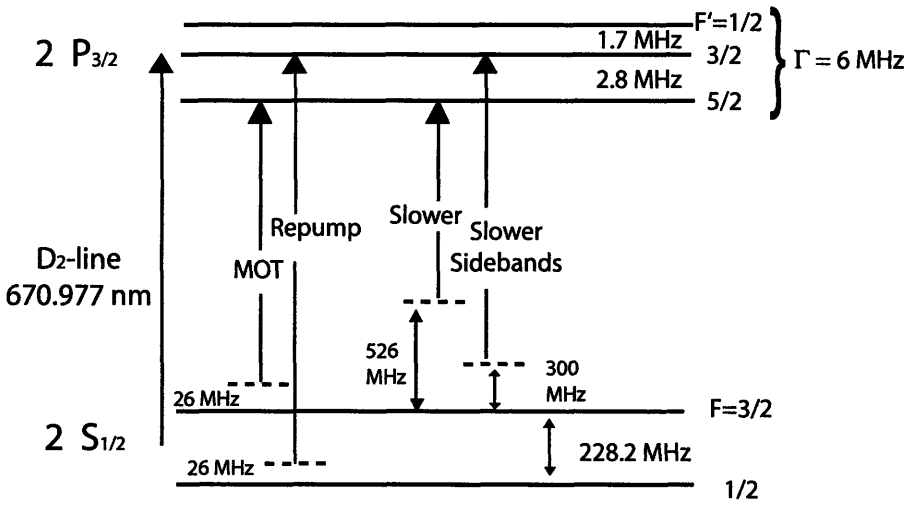

Figure 5-2: Level structure of ^{6}Li and the frequencies needed for slowing and magneto-optic trapping. The excited states of ^{6}Li are not resolved, which makes it difficult to repump ^{6}Li atoms from the F= 1/2 manifold.

Dye laser performance

In the end, we managed to obtain a relatively stable, high power light source. The laser had sub-MHz linewidth, good transverse mode and produced up to 500 mW of power.

5.1.4 Frequency generation scheme

The physics of slowing a hot atomic beam and magneto-optic trapping has been treated extensively elsewhere [68]. Here I summarize in Fig. 5-2 the concrete frequencies needed for trapping and cooling ^{6}Li , and outline our scheme for generating it in Fig. 5-3. Generally, acousto-optic modulators (AOM's) were used to shift frequencies, save for the sidebands on the slower, which were generated using an electro-optic modulator (EOM). An optics table layout is also provided in Fig. D-3.

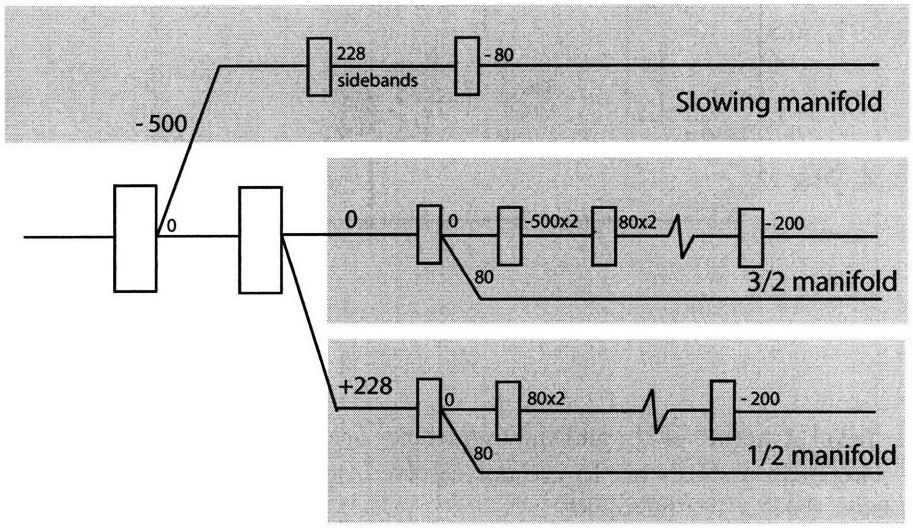

Figure 5-3: Frequency generation of the light required for cooling and imaging ^{6}Li atoms and molecules. Rectangles represent frequency shifters. The frequency of the slowing manifold was determined by the detuning of the Zeeman slower at the oven, while the 3/2 and 1/2 manifold provided the MOT and repump light respectively. They also provided the light needed for imaging atoms in both hyperfine states, tuned by a double-passed 80 MHz AOM. The optional use of an additional double-passed 500 MHz AOM in the 3/2 manifold made it possible to image atoms at high magnetic fields.

5.2 Vacuum

The vacuum system is similar to that previously developed by Claudiu Stan [69] (see Fig. D-1). Two separate alkali reservoirs are used, each heated to a different temperature (420 ^{o}C for ^{6}Li and 350 ^{o}C for ^{23}Na) to enable independent tuning of the two vapor pressures (2.5×10^{-4} mmHg and 8×10^{-2} mmHg respectively). The two alkali species were then overlapped by passing them through the same nozzle.

An additional stage of differential pumping was also added between the oven and the main chamber where our experiments are conducted. It consists of an intermediate chamber pumped by an ion pump and sandwiched between two low conductance differential pumping tubes. Before, we had less than 3 orders of magnitude of differential pumping. After, the sustainable pressure differential rose to 4 orders of magnitude. In the worse case scenario, we could run the experiment when the oven pressure was in the low 10^{-6} Torr.

5.2.1 Baking out

Due to multiple gate valve failures, the main chamber had to be vented a number of times over the years and we have accumulated quite a bit of vacuum lore. As a benchmark, I include here a log of how the pressure typically comes down during a bake of a clean system after a controlled vent with Argon gas with 5.0 (99.999%) purity.

Fig. 5-4 was recorded after a sodium change, performed when the main chamber could not be fully isolated from the oven due to a gate valve failure. However, the intermediate gate valve (IGV, second from the main chamber, see Fig. D-1) was still closing though not sealing. The vent was therefore done with the main chamber filled with Ar gas and the IGV closed, resulting in a very low conductance to the oven when it was opened and the sodium reservoir refilled.

The log starts after the system has been pumped on for several hours by the turbo pump mounted in the oven and the temperature of the bake had stabilized. This bake consisted of heating the whole vacuum system to a temperature between 100 and 150 degrees Celsius, the ion pumps in the main, slower, and intermediate chamber running and the intermediate gate valve closed. After three days of baking, the system was cooled and the titanium sublimation pump in the main chamber brought the pressure down to operating levels.

5.3 Cooling of fermionic ^{6}Li

The actual cooling procedure has been extensively described in multiple theses from this group and I will only give a brief description and include relevant experimental parameters. For details, please refer to [70, 12].

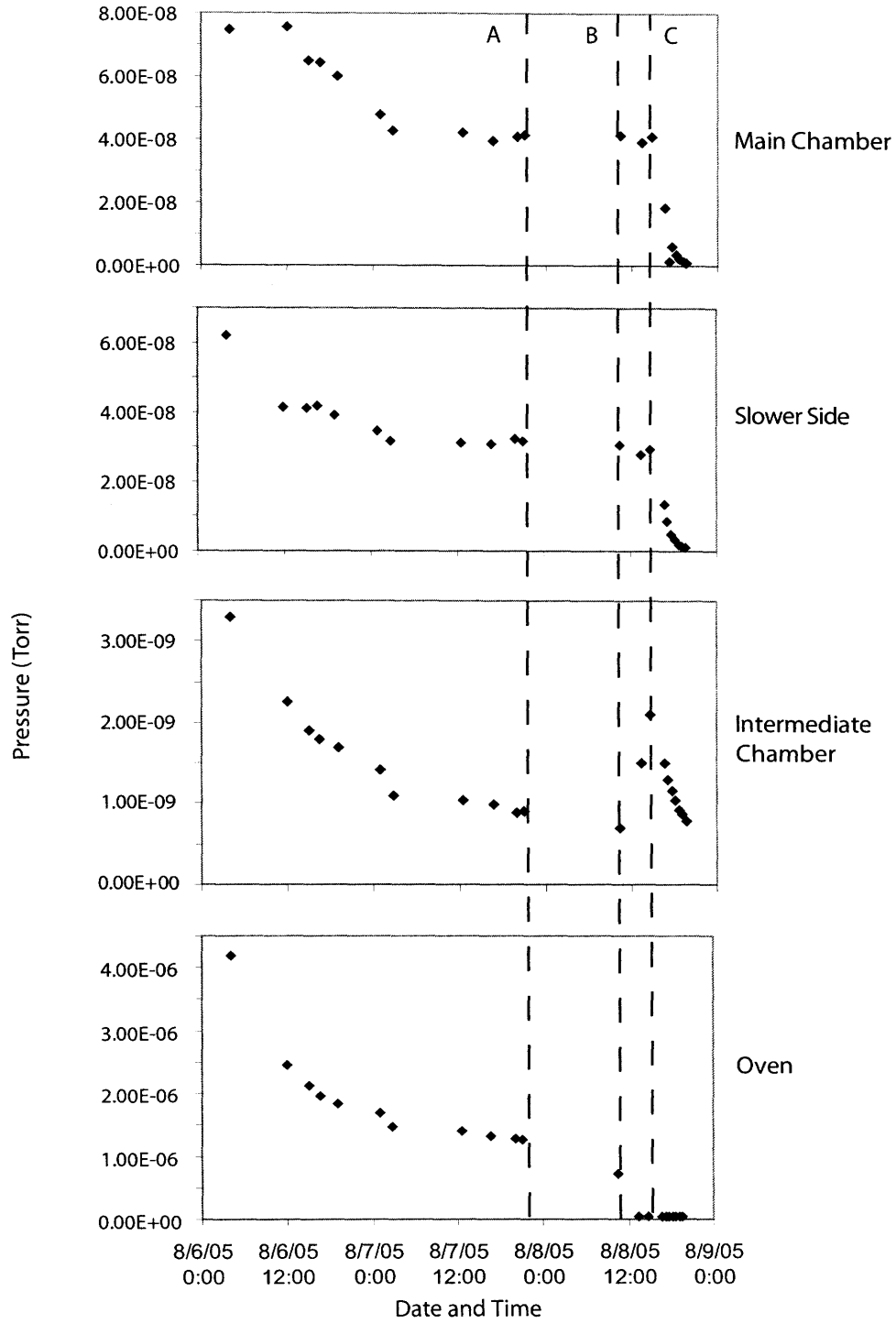

Figure 5-4: Pressure log of our vacuum system during a gentle bake (see text). Dashed line A indicates when the oven temperature (set high during the bake) was turned down, leading to a drop in the oven pressure. B indicates when the ion gauges were degassed, the turbo pump in the oven was valved off and the ion pump started. Between B and C, the IGV was opened, causing a spike in the intermediate chamber pressure. C marks the time we began cooling down the whole system, and the log ends when the pressure in the main chamber has fallen to the 10^{-10} Torr range and the Titanium sublimation pump was fired.

Figure 5-5: (Color in electronic version). Magneto-optically trapped ^{6}Li atoms.

5.3.1 Sympathetic cooling

Optical cooling of individual atoms is limited by the momentum "kick" that each atom experiences when they re-emit the absorbed photon in a random direction [68]. This "recoil limit" can be estimated by setting it equal the recoil energy $k_B T_r = \hbar^2 k^2 / 2m$. Typically, this is on the order of a few μK. This is still far away from the BEC temperatures, which are in the nK range for dilute gases.

While some tricks can be played to achieve sub-Doppler cooling using lasers, the most robust form of further cooling is a form of evaporation. By ejecting the more energetic atoms from the sample, the average energy is lowered. The key to cooling here is the interatomic interactions - elastic collisions are needed to rethermalize the sample and drive the system to a lower entropy state. If there are no interactions, the number of atoms in the low energy states will not be increased even as the hot atoms leave.

For spin-polarized fermions, this is a problem since low-temperature (s-wave) collisions are forbidden by the Pauli exclusion principle. One solution is to cool fermions by placing them in thermal contact with bosons. At the cost of additional complexity, fermion number is conserved as only bosons are evaporated. Given our existing ^{23}Na BEC machine, this was the most natural choice.

Our scheme for sympathetic cooling follows closely the method reported in [70] and is summarized in Fig. 5-6. We start with a dual-species MOT obtained by first loading Li atoms (see Fig. 5-5) for 10 to 15 s before loading Na atoms for another 1 to 2 s. Hyperfine state selection using optical pumping then takes place for a few hundred μs during time-of-flight from the MOT before the atoms are loaded into the magnetic trap. If both ^{6}Li and ^{23}Na are in their doubly polarized states ((3/2, 3/2 for ^{6}Li and (2, 2) for ^{23}Na), the spin mixture will be stable against spin-exchange collisions since there are no distinct pair of states with the same total spin. Initially, the trap is fairly weak, with a high bias field of 80 G. This ensures good separation between the different hyperfine states of Na (see Fig. 5-7), allowing for additional optical pumping followed by a microwave field sweep to fully eliminate population in the other magnetically trappable (2, 1) state. The trap is then

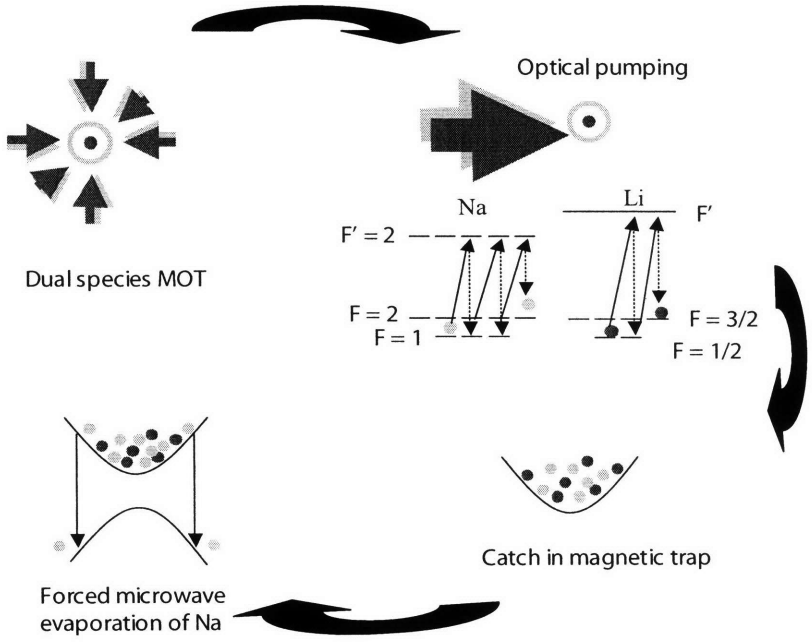

Figure 5-6: (Color in electronic version). The stages of sympathetic cooling. Atoms slowed by a Zeeman slower is loaded into a two-species MOT. Optical pumping of both ^{6}Li and ^{23}Na using σ^+ light transfers atoms into the fully stretched state, before they are caught in a magnetic trap. Forced microwave evaporation of hot ^{23}Na atoms lowers the total energy, and rethermalization cools the remaining ^{23}Na and ^{6}Li atoms.

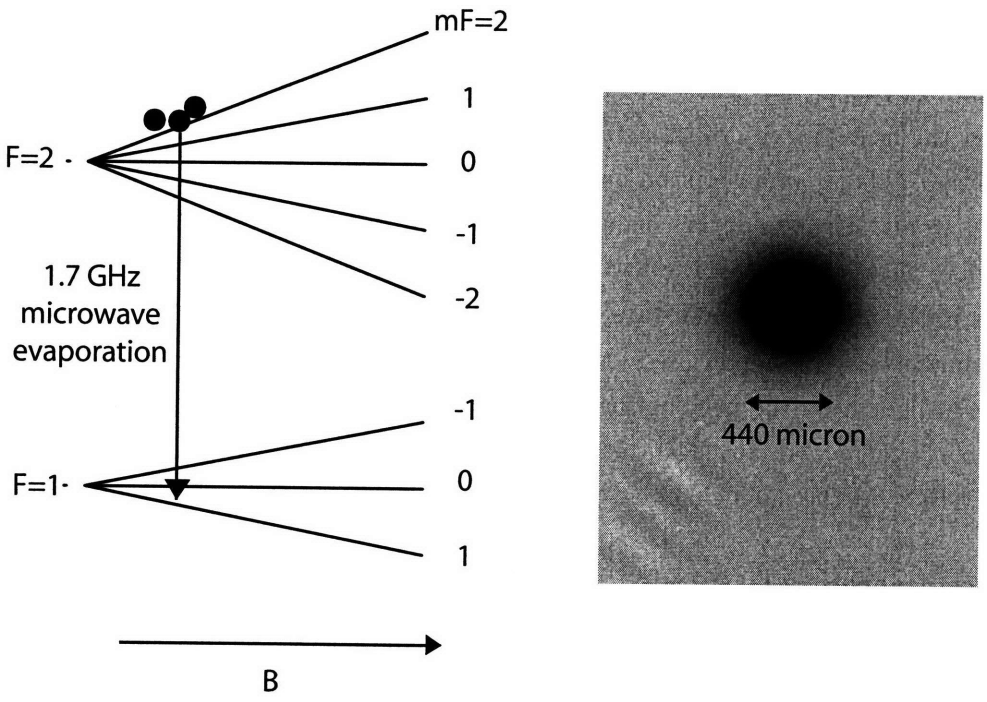

Figure 5-7: Shown on the left is the hyperfine structure of ^{23}Na as a function of magnetic field. Evaporation takes place in the $F = 2, m_F = 2$ hyperfine level by microwave transfer of the energetic atoms to the untrapped $F = 1, m_F = 1$ hyperfine level. The result is a BEC of ^{23}Na atoms in the (2,2) state, shown right in an absorption image taken after 20 ms time-of-flight. The condensate displays clear bimodality of the density distribution, where a diffuse thermal cloud is seen to surround the much denser central condensate core. The total number of condensed atoms is about 10 million, and the trapping frequencies are $\nu_{x,y,z} = (110, 110, 26)$ Hz.

adiabatically compressed by lowering the bias field down to a few gauss once evaporation commences for fast rethermalization.

A microwave transition resonant with the untrappable (1,1) state of ^{23}Na and far detuned from all possible ^{6}Li hyperfine transitions is swept from 1.95 to 1.77 GHz in 11s to eject hot ^{23}Na atoms. To obtain a maximally degenerate Fermi sea, all the ^{23}Na atoms are evaporated away.

F=2 BEC

The amount of cooling possible with this scheme depends on the size of the 'refrigerant'. The larger the heat capacity of the refrigerant, the more ^{6}Li we can cool and the colder it will be. Fig 5-7 shows an absorption image of our F=2 BEC, which contains a respectable 10 million atoms. The size of the condensate in the upper hyperfine state is unsurprisingly smaller than that prepared in the lower hyperfine (1, -1) state, since now the atoms are no longer in the absolute ground state and losses are worse. It is useful to note that since the sodium dye laser is locked close to the D_2 line, the evaporation process is very sensitive to scattered light from the neighboring laser table. Care was taken to mask off all light, particularly if there were any beam paths that could inadvertently collect scattered light and direct them at the main chamber.

Quantum degenerate Fermi sea

At the end of sympathetic cooling we obtain a quantum degenerate sample of spin-polarized ^{6}Li fermions. Fig. 5-8 shows an absorption image of the cold Li cloud taken after ballistic expansion. Around 15 million Li atoms at a temperature of 0.26 T/T_F are obtained.

5.3.2 Cooling near a Feshbach resonance

Close to a Feshbach resonance, two fermions with opposite spin can pair up and populate the bound molecular state with energy close to the open channel energy. Since the resulting composite bosons are quite robust (see Chapter 2), they open up a further avenue for cooling - the composite bosons can be directly evaporated to below the critical temperature for Bose-Einstein condensation.

The hyperfine structure of ^{6}Li is shown in Fig. 5-9 as a function of magnetic field. The various stages involved in cooling are marked from **a** to **f**. After sympathetic cooling, we load about 10 million degenerate Li atoms into a tightly focused optical trap (TOT) (**a**). Using a microwave pulse, we transfer the Li atoms into the lowest hyperfine state (**b**) before ramping up the magnetic field to 822 G (**c**), close to a broad Feshbach resonance at 834 G. In its vicinity, interactions can be made very strong, allowing for efficient evaporation. A

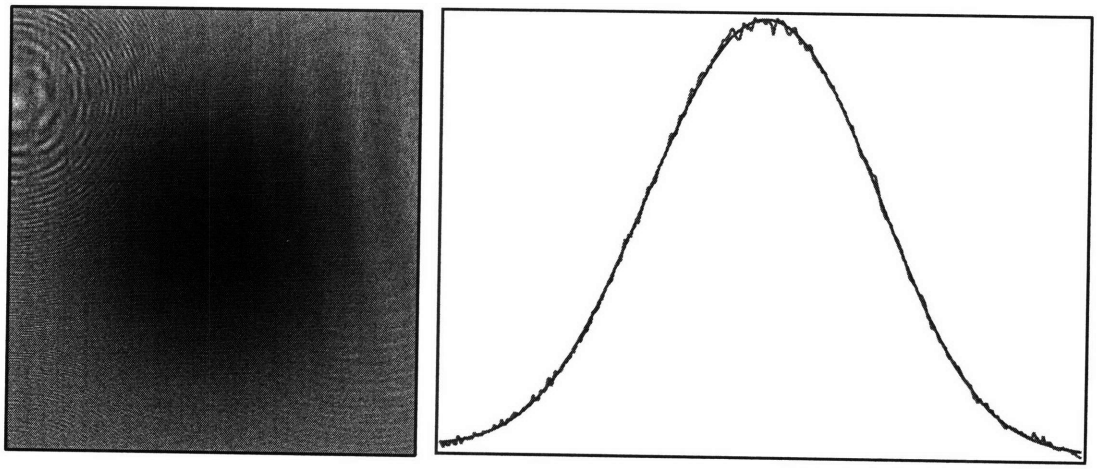

Figure 5-8: (Color in electronic version) Quantum degenerate sea of spin polarized ^{6}Li atoms after 9 ms time-of-flight. The twice-integrated density profile is shown on the right (red jagged curve), fitted to the expected density profile according to Eq. 5.1. Fit parameters yield a temperature T/T_F of 0.26. A gaussian fit to the same density profile yields a χ^2-squared value that is still low, but twice higher, in accordance with the expectation of a smooth transition into quantum degeneracy.

very shallow crossed dipole trap with beam waists of about 60 microns (COT) and depth of $\approx 3\mu$K is also turned on at the same time in order to "catch" the $^6Li_2$ pairs as they cool. A 1 MHz wide, non-adiabatic radio-frequency sweep around 80 MHz transferred 50 % of the atoms into the (1/2, -1/2) state (**d**), and after waiting 100ms for the atoms to decohere, we directly evaporate the two component mixture, by lowering the power of the TOT. As the atoms cool, they pair (**e**) and thermally populate the bound molecular state. Below a critical temperature, the fermion pairs Bose-condense. We lower the optical potential logarithmically for 500 ms before switching off the TOT, leaving all the atoms in the COT. Further evaporation for 200 ms in the COT to a depth of 1.7 μK ensured the lowest temperatures. Absorption imaging after ballistic expansion is done at 730 G on the atomic line (**f**).

Shaping magnetic fields

By themselves, the Feshbach coils anti-confine the ^{6}Li atoms in the relevant hyperfine states along the trap axis [40], also the weakly confining axis of the TOT. Additional curvature has to be provided by the pinch coils. Radial gradients are compensated for by running current in the nulling coil, and by placing the optical trap in the position where gravity

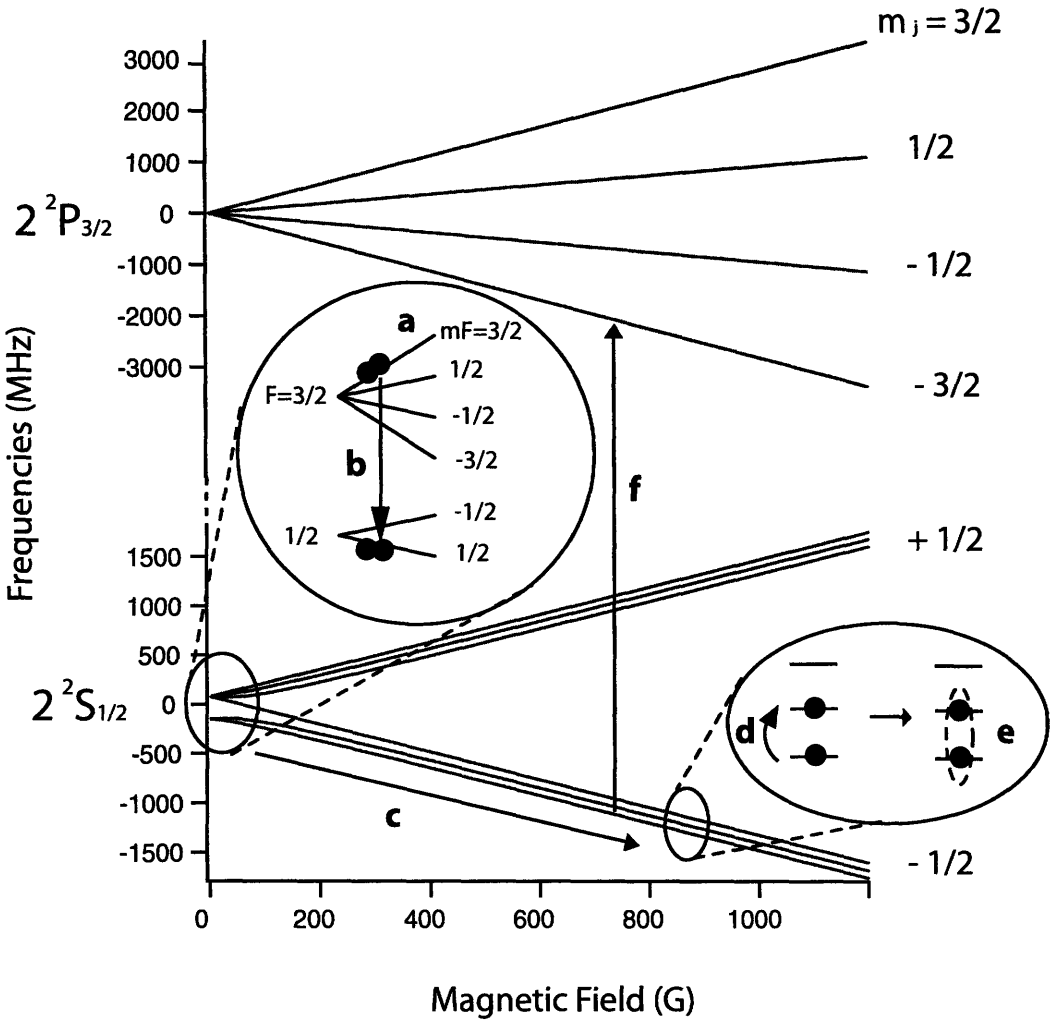

Figure 5-9: Hyperfine structure of ^{6}Li at different magnetic fields. Picking up from where sympathetic cooling left off, the stages for cooling near a Feshbach resonance are indicated in bold (see text for detailed description).

cancels out any remaining vertical gradients. In the end, we managed to create condensates in a very localized region where all field gradients were zero even with imperfect magnetic field coils.

5.3.3 $^6Li_2$ pair condensate

The first observation of a $^6Li_2$ condensate was actually done without transfer into the COT, and is shown in Fig. 5-10. Ballistic expansion followed by absorption imaging reveals the momentum distribution characteristic of a BEC. Implementation of the COT with its nearly spherical trapping frequencies came later, necessitated by mode-matching considerations with the three-dimensional optical lattice. The form of the density profile does not change with the COT and we obtain about 200, 000 Bose-condensed $^6Li_2$ pairs. This is the starting point of all our experiments on fermions in optical lattices.

Lifetime

We investigated the lifetime of the first pair condensate obtained in the COT (Fig. 5-11). The decay is well fitted by a double exponential with decay times $\tau_1 = 67$ms and $\tau_2 = 1$s respectively. While the observed lifetime is rather short relative to previously reported lifetimes of 10 s [14], it is nonetheless sufficiently long for the experiments documented in this thesis. The reason for its brevity is most likely misalignment of the two component beams of the COT relative to each other. A second possibility is the presence of magnetic field gradients due to the imperfect Feshbach coils (see Chapter 2). Subsequent improvements to the alignment and magnetic field shaping extended the lifetime to approach several seconds.

5.4 Fitting formulas

From Chapter 4, we have all the information we need to evaluate our cooling of ^{6}Li . For a quantum degenerate Fermi sea e.g. Fig. 5-8, the spatial distribution of the twice-integrated density profile is given by [44],

$$n(x) = n_F \mathrm{PolyLog}_{5/2}[\mu - \frac{(x-x_0)^2}{R_F^2} \ln(1+\lambda)/\lambda \times (1+\lambda)] \tag{5.1}$$

where $\lambda = \exp[\mu\beta]$ is a fit parameter. The first integration is done automatically when we image, and the second integration is done during the analysis.

From this, we can extract the temperature T/T_F from λ using the relation

$$\left(\frac{T}{T_F}\right)^3 = -\frac{1}{6}\frac{1}{\mathrm{PolyLog}_3(-\lambda)} \tag{5.2}$$

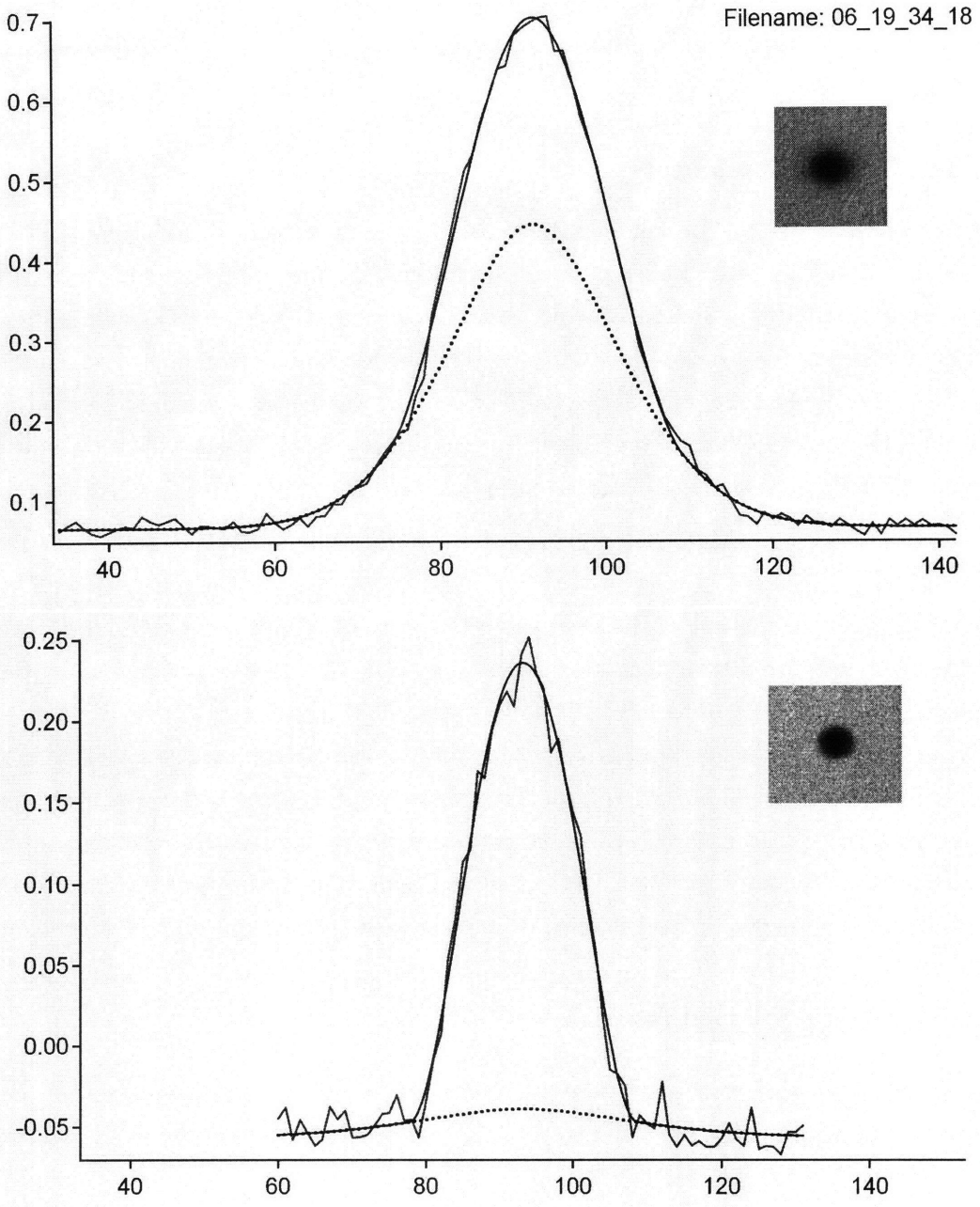

Figure 5-10: The first observation of Bose-Einstein condensate of $^6Li_2$ molecules. This sample was created by evaporating only in the TOT, without transfer into the COT (see text). The temperature of the final condensate obtained can be varied by evaporating to different final optical power. Shown in red jagged lines are density plots of two condensates at different temperatures after ballistic expansion. Solid blue lines are bimodal fits to the data, comprising of a gaussian thermal component (separately plotted in a dashed line) and a Thomas-Fermi fit to the BEC. Top plot shows a condensate emerging from the thermal cloud while bottom plot shows a nearly pure condensate with estimated pair number of 500,000. Insets show absorption images taken along the axial direction.

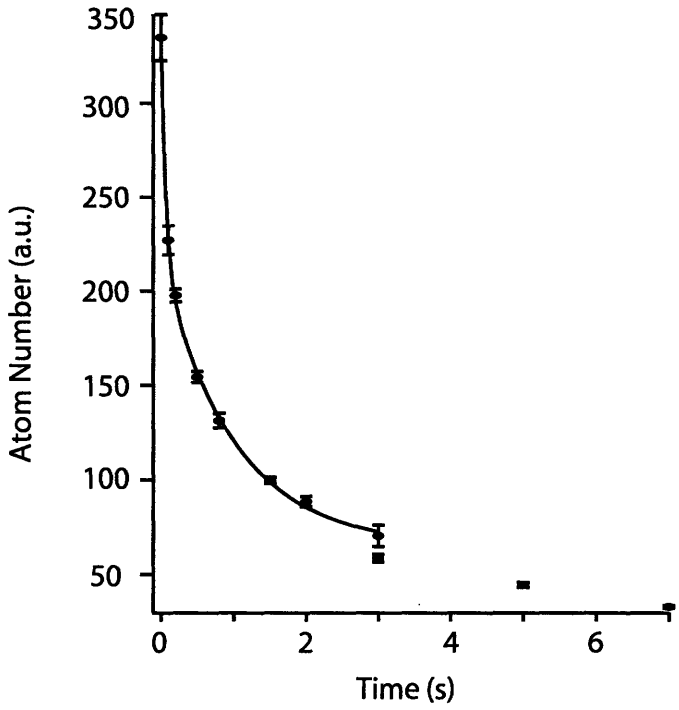

Figure 5-11: Lifetime of pairs in the crossed-dipole trap. The decay is fit to a double exponential with two characteristic time scales, $\tau_1 = 67$ms and $\tau_2 = 1$s. For this data, the background pressure was 1.1 E-10 Torr, and the trapping frequencies of the COT were $\nu_{x,y,z} = (95, 97, 135)Hz$. Error bars show the standard deviation of 5 data points, and last 3 points were excluded from the fit due to slight differences in the condensate production.

derived from equating the two different expressions for N, Eq. 4.9 and Eq. 4.17. Note that this extraction of temperature depends solely on the shape of the cloud, and does not require previous knowledge of T_F.

Chapter 6

Effects of Strong Interactions

This chapter examines in greater detail the key obstacle to observing phase coherence of a fermi superfluid in an optical lattice. A highly abbreviated version is included in Appendix E, but due to space constraints much of the material had to be edited out. Here we present in full the discussions at the time.

In the course of seeking a signature of a superfluid Fermi gas in an optical lattice, the question arose as to whether or not the standard signature - sharp interference peaks during time-of-flight expansion - would indeed be observable. This observation relies on ballistic expansion, where atoms freely expand with their initial momentum, such that an absorption image after long time-of-flight yields a snapshot of the initial momentum distribution. For this description to hold in real systems, scattering events arising from interatomic interactions have to be minimal. For strongly interacting fermions, the fear was that collisions would redistribute momentum during the expansion and smear out all evidence of distinct components before they had a chance to separate out.

Interference was first used to prove the existence of a macroscopic order parameter in a BEC [71] and has since become a standard tool in investigations of BECs. However, it had never previously been observed in a fermionic superfluid system. Thus far, proof of the superfluid nature of the Fermi gas have instead been obtained through observations of anisotropic expansion and condensate fraction inferred from a characteristic density profile in the low-collision limit [13, 14], observation of the pairing gap [72], and the most conclusively through the observation of vortices [73]. With the possible exception of [73], none of them required ballistic expansion.

6.1 The Nature of ^{6}Li Pairs near the Feshbach resonance

To predict how the composite bosons would behave in free expansion, we take a closer look at their nature. The Feshbach resonance of ^{6}Li at 834 G is a broad resonance - i.e. one

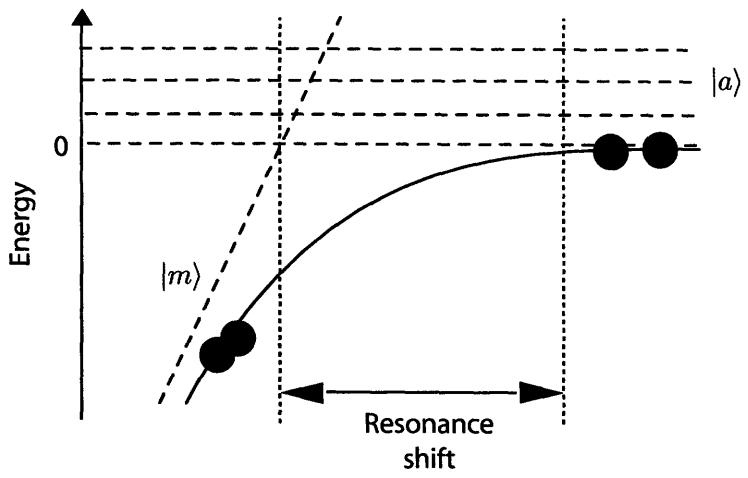

Figure 6-1: This figure shows in greater detail the behavior of the binding energy (solid line) on detuning near a Feshbach resonance. The true resonance position is shifted from the crossing of the bare molecular state $|m\rangle$ (slanted, dashed line) with the atomic continuum states $|a\rangle$ (horizontal dashed lines) due to strong coupling. Far away from the resonance, the pairs are tightly bound and are almost purely molecular in character. Close to the resonance however, the pairs are loosely bound and there is a strong admixture of atomic character.

that satisfies

$$k_F|R^*| << 1 \tag{6.1}$$

where the effective range of the interaction $|R^*|$ is proportional to the inverse width of the Feshbach resonance. This implies that the effective range is unimportant at the many-body level, and macroscopic properties of the gas only depend on the dimensionless parameter $k_F|a|$. For the rest of this thesis, $1/k_Fa$, also known as the interaction parameter, will be used to parameterize our location within the strongly interacting regime.

Other notable characteristics of these composite bosons include

Binding energy Close to resonance, the binding energy of the pairs is

$$\epsilon_b = -\frac{\hbar^2}{ma^2} \tag{6.2}$$

Fig. 6-1 shows how it varies close to the resonance.

Size From Eq. 6.2, the size of the two-body bound state is just the scattering length

a. However, in a many-body system, a can become larger than the interparticle separation $n^{-1/3}$ and therefore ceases to be a relevant length scale. The pairing then becomes mediated by the many-body physics, and the size of the pair is rather given by $n^{-1/3}$.

Atomic character Since the coupling is not diagonal in $|a\rangle$ and $|m\rangle$, the solution $|\psi\rangle$ to the coupled problem $H|\psi\rangle = E|\psi\rangle$ generally comprises of a superposition of both atomic and molecular states. Due to the unusually strong coupling for ^{6}Li , the estimated fraction of molecular character close to resonance is actually less than 1% [74]. The large shift in Fig. 6-1 in the resonance position is also a direct result of the coupling strength. Experimentally, this property is exploited when we image the molecules on the atomic transition close to resonance.

6.2 Collisions in Unitarity-Limited Fermi Superfluids

When $1/k_F a < 1$, we enter the strongly interacting regime and a falls out of the determination of scattering amplitude. Eq. 2.4 instead becomes

$$\sigma = \frac{4\pi}{k^2} \tag{6.3}$$

$1/k_F$ is in turn on the order of interparticle spacing $n^{-1/3}$, in keeping with our initial expectation.

In its simplest case, we would like to understand how a unitarity-limited superfluid Fermi gas with two distinct and well separated momentum components (Δp on the order of Fermi momentum p_F) expands. There are two ways to think about this. As we shall see, they are consistent with each other and result in the same observable behavior.

6.2.1 Collisions in a two-component Fermi gas

The strong admixture of the atomic channel in the paired state suggests that we can ignore their bosonic nature and just treat the problem as that of a two-component, strongly interacting Fermi system. In this case, it has been well established that the high elastic collision rate can give rise to classical collisional hydrodynamics, independent of pairing. Quantum statistics play a part only if there are no empty states for the fermions to scatter into and collisions are therefore Pauli-blocked [75].

The effect of collisions on the phase space distribution $f(x, p, t)$ can be calculated from the Boltzmann transport equation [76]

$$\frac{\partial f}{\partial t} + \mathbf{v} \cdot \frac{\partial f}{\partial \mathbf{x}} = \Gamma_{coll}[f] \tag{6.4}$$

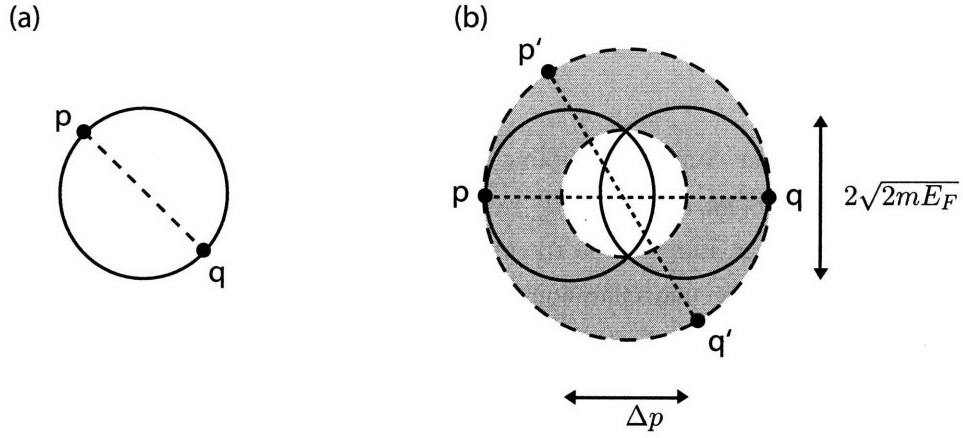

Figure 6-2: Collisions in a two-component Fermi gas in momentum space. Assume that the two components have equal distributions and are labeled with p and q. In (a), there are no empty final states in an isotropic, filled Fermi sea for particles p and q to scatter into. (b) shows two filled Fermi distributions (say distribution A and B) with central momentum $\Delta p = \sqrt{2mE_F}$ apart. Within the gray area, particles from A (e.g. p) can always collide with a particle from B (e.g. q) into initially empty final states (p' and q').

where $\mathbf{v} = \mathbf{p}/m$ and $\Gamma_{coll}[f]$ is the collision integral. The collisions act to restore local equilibrium, and for sufficiently fast collisional relaxation, would always drive the system towards an isotropic momentum distribution, leading to the hydrodynamic equations. Collisional hydrodynamics is responsible for the anisotropic expansion of a strongly interacting Fermi gas [61], where the deformation of the Fermi surface in time-of-flight opens up available states for scattering. As Fig. 6-2 illustrates, the situation we are investigating starts out already highly anisotropic. No time is needed before the atoms begin to collide and redistribute momentum.

6.2.2 Collisions in a BEC

Alternatively, we could choose to ignore the underlying fermionic nature of the superfluid $^6Li_2$ pairs and instead treat them like a regular BEC, keeping in mind the unusually strong interactions. In that case, they should evolve according to the Gross-Pitaevskii equation 3.3, where the dimer-dimer scattering length has been calculated to be $a_{dd} \approx 0.6a$ [77].

Collisions between weakly interacting BEC's with high relative momenta have been discussed in the literature [78], and observed [79]. It can be treated by incorporating the next highest k term in the scattering amplitude, and re-writing the non-linear coupling

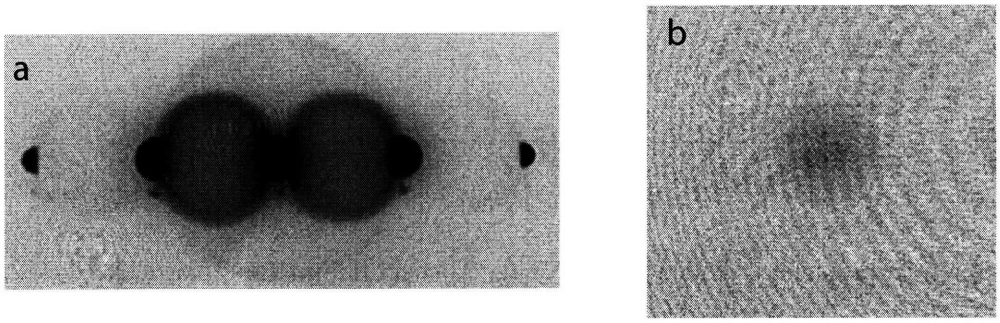

Figure 6-3: The effect of collisions on ballistic expansion. (a) shows a time-of-flight image of a sodium BEC with 5 momentum components, 0, $\pm 2\hbar k$ and $\pm 4\hbar k$. s-wave halos can be seen between neighboring momentum components, most prominently between 0 and each of the $\pm 2\hbar k$ momentum components. Faint second order s-wave halos between the $\pm 2\hbar k$ components can also be seen. (b) In the case of strongly interacting fermions, multiple collisions result in the smearing out of any distinct momentum components.

constant U_0 in Eq. 3.3 more generally as

$$U_0 = -\frac{4\pi\hbar^2}{m}(-a + ika^2) \tag{6.5}$$

For two condensates colliding with large momentum difference k, the second term becomes significant and introduces an elastic scattering loss from the colliding condensates into initially unpopulated states. The beautiful 's-wave halos' which have been observed (see Fig. 6-3 (a)) is described thus.

If we extrapolate from this and allow the scattered atoms to re-scatter and undergo multiple collisions, then even the s-wave halos will smear out, ultimately approaching a uniform gaussian, reflecting the isotropy in momentum space. This is the same end result reached by considering the system as a two-component Fermi gas, and is indeed what we see in Fig. 6-3 (b).

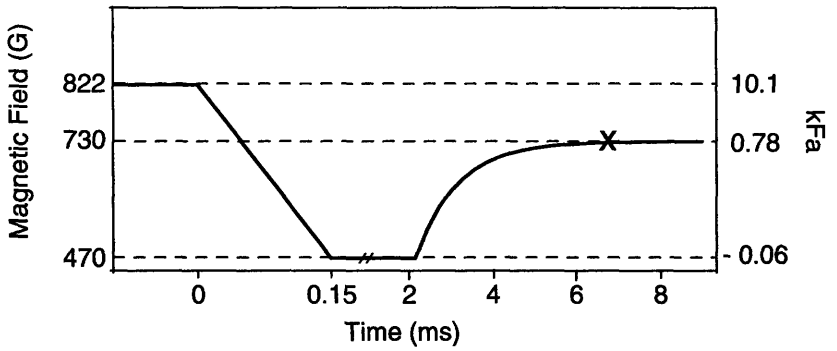

Figure 6-4: Experimental sequence of the magnetic field ramp. Ramp down speed is limited by the clamp voltage of the varister used and ramp up speed is limited by the maximum voltage of our power supplies. Also shown is the inverse interaction parameter $k_F a$ corresponding to each magnetic field for the Kapitza-Dirac experiment.

6.3 Solving the collision problem

6.3.1 Magnetic field ramp

Collisions have been problematic before, when initial observations of anisotropic expansion [61] turned out not to be due to superfluid hydrodynamics, but probably rather to collisional hydrodynamics [80, 81, 75]. The ambiguity was eventually resolved by a rapid magnetic field ramp which quickly brought the system out of the strongly interacting regime and collisions became negligible.

If the magnetic field ramp is sufficiently slow with respect to the coupling, its effect is to transform the loosely bound two-body state close to the Feshbach resonance into a deeply bound molecular state far from the resonance. Due to the strong coupling in ^{6}Li , this condition is always fulfilled. However, the response of the many-body system is much slower than the field ramp [82], and the deeply bound molecules can be treated as weakly interacting bosons having the center of mass momentum distribution of the initial $^6Li_2$ pairs.

Out of the strongly interacting regime, the persistence of anisotropy then proved superfluid hydrodynamics. After sufficient expansion, the magnetic field can be ramped up close to the resonance again for imaging on the atomic line. During time-of-flight, the density of the pairs falls significantly, such that collisions do not recur. This technique was used to observe the characteristic momentum distributions for a condensate of $^6Li_2$ pairs shown in Fig. 5-10. The sequence of magnetic field ramp is also shown in Fig. 6-4. With slight differences in the specific values, this is the general form of magnetic field ramp commonly used to study strongly interacting superfluids.

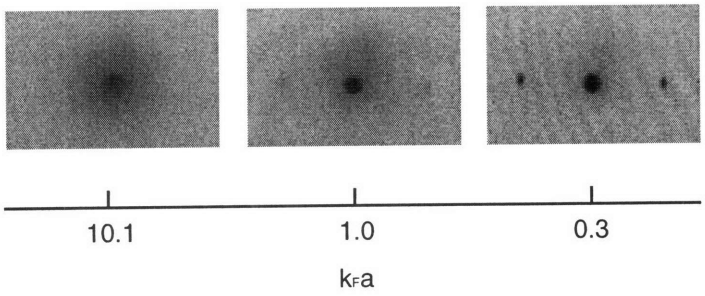

Figure 6-5: Visibility of distinct momentum peaks for different $k_F a$. Within the strongly interacting regime ($k_F a$ large), the different momentum peaks are smeared out.

6.3.2 Kapitza Dirac scattering at different $k_F a$'s

Using this magnetic field ramp, we perform a simple experiment to study how ballistic expansion of different momentum components in a $^6Li_2$ superfluid is affected by collisions, as a function of when they were imprinted. A straightforward way to introduce different momentum components into the system that relies only on single-particle physics is to perform Kapitza-Dirac scattering [83, 84]. This is very similar to the two-photon Bragg process described in subsection 3.4.1. The main difference lies in the duration of the light pulse applied - if it is made very short, then energy is not conserved and the energy spread is given by $\Delta E = h/\Delta t$. The atoms can then acquire several momentum components in multiples of $\pm 2\hbar k$.

Our light pulse was made up of a single, retro-reflected, 1064 nm light beam, lasting only 10 μs, with an energy spread of $h \times$ 100kHz, imparting momenta of $\pm$15kHz onto the system. The shortness of the pulse meant that we could pulse on the light at different values of the magnetic field during the 100 to 150 μs field ramp, thereby imprinting momenta at different $k_F a$. The field ramp for all the experiments are the same, differing only in the timing of the pulse.

Fig. 6-5 shows the results obtained. Deep in the strongly interacting regime the distinct momentum components were smeared out into a broad featureless Gaussian, which is almost isotropic. At $k_F a \approx 1$, distinct momentum peaks begin to appear, becoming even more distinct at lower fields, where interactions are weak. For our system, the mean free path of a weakly bound pair while in the strongly interacting regime ($\sim 1/k_F$) is always less than the size of the sample.

6.3.3 Collisional product?

A natural question to ask is what is the collisional product? The dimers are colliding with energies $\hbar^2k^2/2m$ which can be larger than the binding energy (Eq. 6.2) close to resonance. Energetically, it is possible for the dimers could break up into atoms, with each fragment taking a part of the remaining kinetic energy. Less likely, but still possible, the dimers could remain bound, and merely heat.

One way to distinguish between atoms and dimers would be to image at low magnetic fields where the molecular transition is far detuned from the atomic transition. We attempted to do this but unfortunately the results were ambiguous. There was evidence that there was a slight increase in the atomic signal, but finally signal-to-noise was not good enough for a firm conclusion. This measurement is also complicated by the fact that even if the molecules broke apart during a collision, they can easily recombine again during the field ramp and disappear from the atomic signal.

6.3.4 Interpretation

Collisions within the superfluid are only able to take place if the relative velocities of the colliding particles exceed the critical velocity. This became the subject of a further investigation, expounded upon in the thesis of Daniel Miller, and appended here in Appendix F. While details are not provided here, our measured critical velocity of a Fermi superfluid was indeed much lower than the recoil momentum of $2\hbar k$.

6.4 Necessity of rapid field ramps

This demonstrates that collisions during the first few moments of expansion of a strongly interacting system do inhibit observation of distinct momentum peaks. From [85], the inverse collision rate at unitarity is estimated to be $0.23\hbar E_F/(k_BT)^2$, which evaluates to $\approx 40\mu$s for a conservative estimate of $T/T_F = 0.1$, faster than we are able to ramp out of the strongly interacting regime.

In previous studies of strongly interacting Fermi gases, magnetic field sweeps were applied to prevent fermion pairs from dissociating, since T_c drops when density drops. However, it has recently been shown that fermion pairs survive during the first few milliseconds of expansion even on the BCS side of the Feshbach resonance [86]. In the work presented here, the suppression of collisions early during the expansion required a faster magnetic field switch off and was necessary on both sides of the Feshbach resonance.

Chapter 7

Paired fermions in an Optical Lattice

In this chapter, I will expand upon the work reported in the publication:

J.K. Chin, D.E. Miller, Y. Liu, C. Stan, W. Setiawan, C. Sanner, K. Xu and W. Ketterle, "Evidence for Superfluidity of Ultracold Fermions in an Optical Lattice, Nature **443**" *961-964 (2006)* [87]. Included in Appendix E

7.1 The Promise of Optical Lattices

An easy way to see the potential of fermions in optical lattices is to consider T_c again for weak attractive interactions. From section 4.2.1, we have $T_C \approx 0.28 T_F e^{\pi/2k_F a}$ in the bulk Fermi gas. It is this exponential suppression of T_c with increasing $k_F a$ that makes BCS pairing so difficult to observe in the bulk system. In a periodic system however, the dependence of the exponent changes. For a three-dimensional lattice, it has been predicted that $T_c \approx te^{-7t/|U|}$ in a shallow lattice where $t >> U$, t being the tunneling energy and U the interaction energy [88, 89]. As the lattice is ramped up, pairing is promoted through increased localization, leading to an enhancement of T_c. A turning point in the value of T_c comes when the localization becomes so strong that it inhibits the establishment of a macroscopic order parameter necessary for superfluidity. In terms of the microscopic scattering length a, the maximum T_c has been simulated to be $\approx 0.3 T_F k_F |a|$. T_c is now expected to scale linearly with a, a dramatic improvement over the situation in the bulk.

7.2 Optical Lattices

To form a periodic potential for neutral atoms, the easiest way is to use light. Optical lattices make use of a spatially varying AC Stark shift from far-detuned light and the interference of two or more beams to form a conservative and periodic trapping potential for atoms. In the limit when the detuning of the light $\Delta = \omega_0 - \omega_{laser}$ is much larger than the decay rate of the excited state, $\Delta >> \Gamma$, the dipole potential depends on the intensity profile $I(r)$ as

$$V_{dip}(R) = \frac{3\pi c^2}{2\omega_0^3}\frac{\Gamma}{\Delta}I(r) \tag{7.1}$$

For a gaussian laser beam, the intensity profile for a beam propagating along z is

$$I(r,z) = \frac{2P}{\pi w^2(z)}e^{-2r^2/w^2(z)} \tag{7.2}$$

where P is power, r is the distance from the axis of propagation, and w is the $1/e^2$ radius. w and z are related by $w(z) = w_0\sqrt{1 + z^2/z_R^2}$, and the entire beam can be characterized by the Rayleigh range z_R and beam waist w_0 which are related by $z_R = \pi w_0^2/\lambda_L$.

Optical lattices are typically formed by light beams intersecting at their beam waists, where intensity is at a maximum and the phase wavefronts are parallel. A standard beam waist of about 100 μm leads to a Rayleigh range on the order of mm's. For cold atom sizes of less than 100 μm, this ensures that the optical lattice is relatively uniform across the entire sample.

In the simplest configuration, two counterpropagating laser beams will give a dipole potential of

$$V_{dip}(r,z) = -V_0 \cdot e^{-2r^2/w_0^2} \cdot \sin^2(k_L z) \tag{7.3}$$

where $k = 2\pi/\lambda_L$ is the wave vector of the light and $V_0 = 4 \cdot (2P/\pi w_0^2)$ is four times larger than that of a single beam due to constructive interference.

7.2.1 Non-interacting systems in optical lattices

For a uniform system confined in volume V, the eigenstates to the free Hamiltonian H_0 are just plane waves:

$$\begin{aligned} H_0 &= -\frac{\hbar^2}{2m}\nabla^2 \\ |p\rangle &= e^{ip/\hbar x} \end{aligned}$$

When a periodic potential with spatial periodicity of a_L is present, the solutions must also be invariant under translation by a unit a_L, differing at most by a phase shift. Assuming a

periodic potential of the form

$$\begin{aligned} V &= \frac{V_0}{2}(\sin^2(k_L x)) \\ k_L &= \frac{\pi}{a_L} \end{aligned}$$

From Bloch's theorem, the solutions then become

$$\phi_{q,n}(x + a_L) = e^{iqa_L}\phi_{q,n}(x) \tag{7.4}$$

These are the Bloch functions and they are labeled by their band index n and the quasi-momentum q. Their energies are plotted in Fig. 7-1. The recoil energy, defined as

$$E_R = \frac{\hbar^2\pi^2}{2ma_L^2} \tag{7.5}$$

becomes a natural unit for energy, and the depth of the lattice can be parameterized as

$$V_0 = sE_R \tag{7.6}$$

From Fig. 7-1, we can get a qualitative understanding of how the dispersion of a periodic potential changes as a function of lattice depth. For a vanishingly shallow lattice, the dispersion is just that of a free particle $\epsilon(p) = p^2/2m$. As the lattice depth is increased, gaps begin to open up at the band edges and the bands begin to flatten. Already for a $5E_r$ deep lattice, the lowest band is almost completely flat.

Ground state in a shallow lattice

For a shallow lattice, the problem for $H = H_0 + V$ can be solved by perturbation theory. Since the perturbing periodic potential V has non-vanishing components only between states spaced k_L apart, we need only consider the plane waves $|q\rangle, |q \pm mk_L\rangle$ where m is an integer. To solve for the ground state where $n = 0$, we can already obtain a good approximate solution by considering plane waves with $m = 0, \pm 1$.

The Bloch functions $\phi_{q,0}$ are now superpositions of the free-momentum states $|q\rangle$, $|q+k_L\rangle$ and $|q - k_L\rangle$,

$$\phi_{q,0} = \sum_{m=0,\pm 1} u_m e^{imk_L x} \tag{7.7}$$

Tight binding limit

In the situation where the lattice height is high and the tunneling between wells are small, the expression for the dispersion $\epsilon(p)$ assumes a simple analytic form:

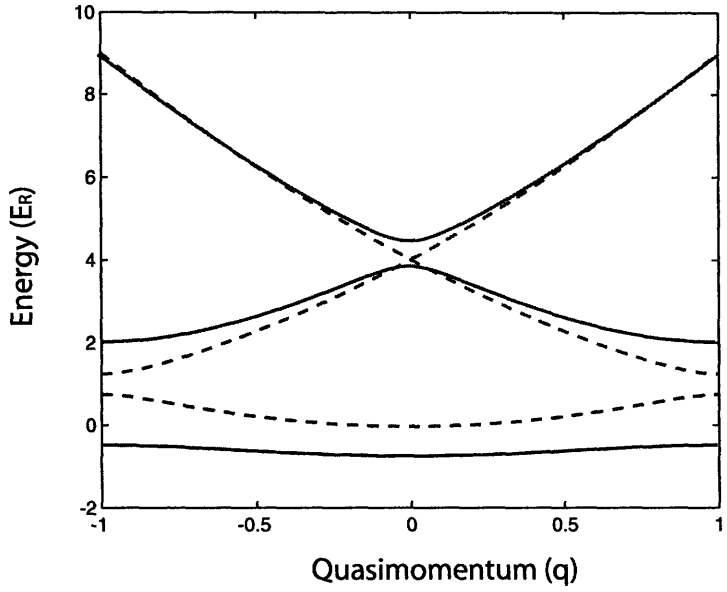

Figure 7-1: (Color in electronic version) Band structure of optical lattice for $n = 0$ (blue), 1 (green) and 2 (red). Solid lines show the level structure of a 5 E_r deep lattice, while dotted lines show that of a 1 E_r deep lattice.

$$\epsilon(p) = 2\delta[\sin^2(\frac{p_x d}{2\hbar}) + \sin^2(\frac{p_x d}{2\hbar}) + \sin^2(\frac{p_x d}{2\hbar})] \tag{7.8}$$

where the bandwidth of the lowest band is 2δ and decreases exponentially for large s as

$$\delta = \frac{8}{\pi} E_R s^{3/4} \exp(-2\sqrt{s}) \tag{7.9}$$

and the energy gap between the first and second band becomes

$$\hbar\omega_L = 2\sqrt{s}E_R \tag{7.10}$$

This formalism is easily generalizable to two and three dimensions, and the presence of an external trapping potential does not significantly change the solution as long as it varies slowly compared to the lattice period. It can also tolerate weak inter-atomic interactions as long as they are weak relative to the tunneling. Since spin-polarized fermions are close to an ideal non-interacting gas, the above description has been shown to work well from direct observations of the Fermi surface filling the first Brillioun zone [90], oscillation measurements [91, 92], and anti-bunching reflecting the Pauli exclusion principle [93].

7.2.2 The single-band Hubbard model

However, the above model fails to capture the physics of phase transitions, when interactions between particles become significant. This can happen in two ways - in the tight binding limit, the on-site interactions can dominate over the tunneling energy, and when the s wave scattering length a becomes so large that interactions can dominate even in a weak lattice.

To treat the first case, a second quantized, microscopic theory of particles in a periodic potential has been developed. Known as the single band discrete Hubbard model, it was originally a phenomenological model for studying solid state systems. In its simplest form, it assumes that the atoms are very cold and only occupy the lowest band of a deep lattice (valid when $kT, E_F << \hbar\omega_L$). Then the Hamiltonian of the system can be written as

$$H = -t\sum_{(i,j)}(c_{i\uparrow}^\dagger c_{j\uparrow} + c_{i\downarrow}^\dagger c_{j\downarrow}) + U\sum_i n_{i\uparrow}n_{i\downarrow} \tag{7.11}$$

where the indices i and j are over the sites in the lattice, and (i,j) correspond to neighboring sites. The parameter t corresponds to the tunneling, and can be identified with the parameter $1/2\delta$ in the previous model, while the parameter U describes the on-site interactions between two fermions when they are localized on the same site. Using the effective interaction given by Eq. 3.2, U can be expressed as

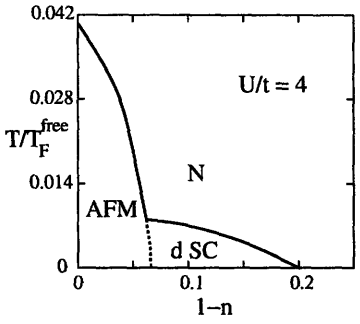

Figure 7-2: Phase diagram in a square lattice for repulsive interactions in an optical lattice, taken from [88]. On the abscissa is the filling factor while the ordinate gives temperature.

$$U = \frac{4\pi\hbar^2 a}{m} \int dr |\psi_0|^4 \tag{7.12}$$

and can take both positive and negative values.

Quantum phase transitions

It is the interplay of t, U and the filling factor ρ in an optical lattice that gives rise to the different ground states (or phases) of the system. At the beginning of this chapter, we saw how for moderate tunneling and $U < 0$, a BCS state at much higher T_c's become possible. Additional rich physics also arise for $U > 0$ (see Fig. 7-2).

$U > 0, \rho = 1$: Antiferromagnetic ordering If the pairs repel each other and there is exactly one fermion per site, then the lowest energy state for a bipartite lattice (e.g. cubic) is a regular array of alternating spins (see Fig. 7-3).

$U > 0, \rho < 1$: d-wave superfluidity A d-wave superfluid is expected to form when the filling factor is much less than 1 fermion per site. Since this is a suggested pairing mechanism responsible for high T_c superconductors, it is particularly intriguing.

Limitations of the single-band Hubbard model

One of the limitations of the single-band Hubbard model is its inability to model systems where the s-wave scattering length is larger than the lattice length scales (a_{ho}, a_L). All the aforementioned phase transitions take place at fairly low $(T/T_F << 1)$ temperatures, and currently, state-of-the-art cooling has been most successful within the BEC-BCS crossover, where temperatures in the bulk phase have reached $T/T_F \approx 0.05$. However, interactions within the crossover are in the unitarity regime and single band models no longer suffice, since U can now be on the order of $\hbar\omega_L$. Moreover, the Feshbach resonances that make it possible to tune interactions also bring into close proximity a closed channel bound state,

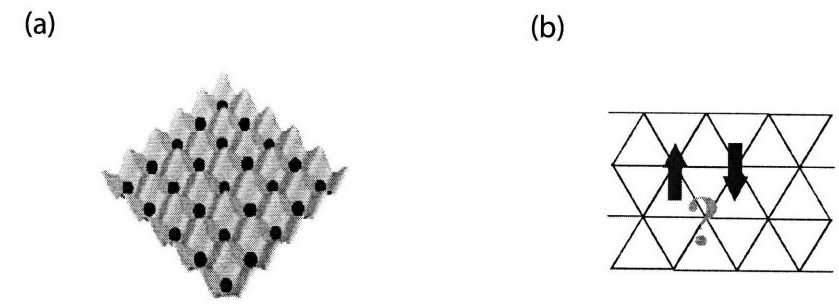

Figure 7-3: Visualizations of (a) antiferromagnetic ordering in a square lattice and (b) spin frustration in a triangular lattice.

which has to be taken into account explicitly. Some theoretical work is beginning to address this problem, but as yet there is no real consensus [94, 95, 96].

7.3 Experiments with Strongly Interacting Fermions in Optical Lattices

Our optical lattice setup was inherited from the previous generation of graduate students, who had set it up to study the physics of bosons in optical lattices [24, 25]. Fig. 7-4 shows the configuration of all the lattice and optical dipole beams. The details of aligning invisible lattice beams is given in the thesis of Kaiwen Xu [23] and will not be elaborated on here. I will only note that our alignment procedure for experiments with ^{6}Li still began with aligning the beams to the sodium BEC as it was simpler to produce and contained many more atoms, making it much easier to observe slight perturbations to the sample when the infra-red beam came close. Fine alignment is then completed using $^6Li_2$ molecules.

7.3.1 Techniques

Instead I will focus on the additional tricks involved in loading strongly interacting fermions into an optical lattice. Not surprisingly, this turned out to be more complicated than simply loading superfluid bosons.

If we restrict ourselves to using ballistic expansion as a diagnostic tool, there are three ways to know that one has succeeded in loading fermions into an optical lattice without significant heating. One can observe the sharp edges of a filled Brillouin zone [90] or see anti-correlation peaks in the second-order correlation function [93]. For superfluid systems which reside in the ground state of the lattice, an additional signature comes from the

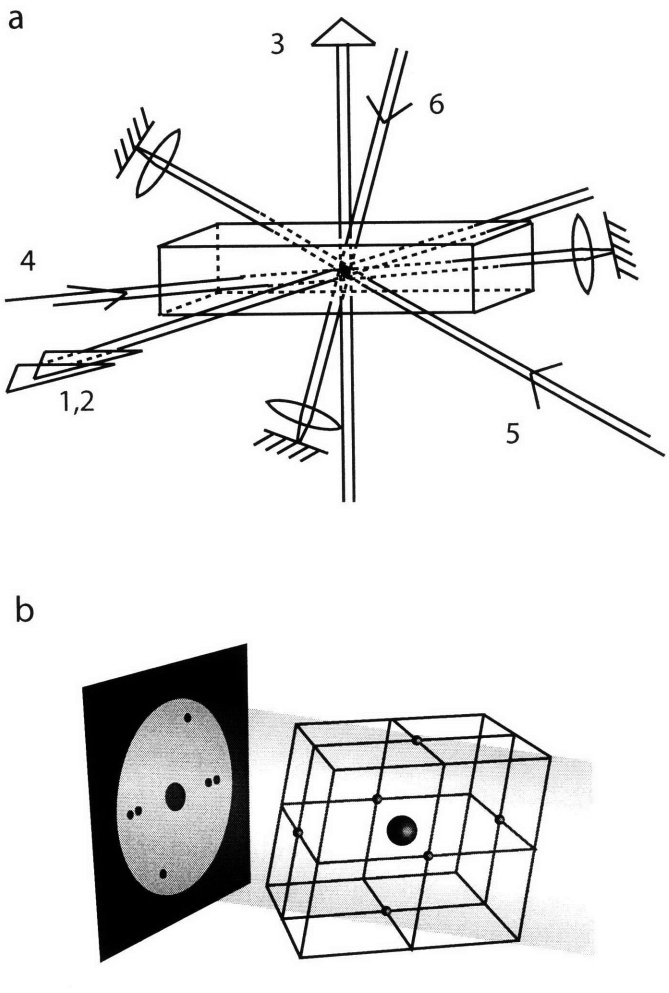

Figure 7-4: The complicated optical setup of the far detuned 1064 nm light, used both for creating a crossed optical trap and a three-dimensional lattice. Shown in (a) is their relative paths to the rectangular glass cell, where, in lab terminology, they are (1) tight ODT, (2) horizontal ODT, (3) vertical ODT, (4) left lattice, (5) right lattice, and (6) top lattice. The top lattice beam is at a 20^o angle to the vertical. For the lattice beams, lenses focus the forward propagating beam down before retro-reflection from a mirror. (b) shows the lattice geometry in momentum space and the expected image in time-of-flight.

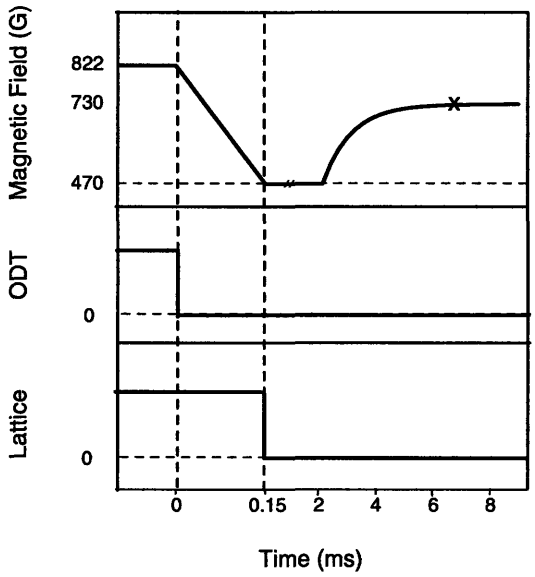

Figure 7-5: The timing sequence that ensures the ballistic expansion for observation of distinct momentum peaks. By quickly ramping to 470 G, strongly interacting $^6Li_2$ pairs are projected into weakly interacting, deeply bound molecules. The fastest ramp we can achieve is 150 μs due to technical limitations.

sudden projection from the lattice ground state into the free momentum states according to Eq. 7.7, yielding a characteristic interference pattern after ballistic expansion [18]. We choose to observe the third.

Switch off procedure

During time-of-flight out of the lattice, a very precise timing sequence was used to ensure optimal fringe contrast (see Fig. 7-5). The optical dipole trap was switched off as soon as the magnetic field began to ramp down, while the optical lattice potential was kept on until the magnetic field had fallen sufficiently to take the system out of the strongly-interacting regime. The latter measure was necessary to solve the problem of collisions, as discussed in Chapter 6.

In order to determine if the switch off procedure affected the many-body dynamics of the system, the other time-scales present in the system has to be considered [44]:

Two body dynamics Given by $\hbar/\langle\phi_b|V|\phi_a\rangle \approx \hbar/g_0\sqrt{n}$, where $\langle V\rangle$ is the coupling between the molecular and atomic state (Fig. 6-1) [97]. For ^{6}Li parameters and typical densities on the order of 10^{13} cm^{-3}, this evaluates to 20 ns.

Magnetic Field ramp Given by $g_0\sqrt{2\pi n}/\Delta\mu\dot{B} \approx 1.2\mu$s, where $\dot{B} \approx 5\text{G}/\mu$s for the rate of our magnetic field ramp (Fig. 2-7). Therefore a long range molecule can always adiabatically follow the field ramp and project into a short range composite boson, thus revealing the center of mass distribution of the pairs within the resonance.

Fermi energy Evaluates to $\hbar/E_F \approx 5\mu$s for our Fermi energy of $E_F = k_B \times 1.4\mu$K.

Evaporation rate Given by trapping frequency, ≈ 4 ms.

Recoherence rate This is likely bounded by the trapping frequency to be > 4 ms, although there is some dispute [18]. We argue that if the sample has dephased, it has to take the phase information finite time to disseminate throughout the system, and the only global time scale available is the trapping frequency. Moreover, this is likely a lower bound on the time it takes to recohere, since the presence of the lattice impedes tunneling.

From this analysis, it seems clear that the many body dynamics could not have changed on the time scale of the field ramp either due to further cooling or recoherence. Additional evidence can be obtained from Fig. 7-10, where the width of central momentum peak is seen to fully recohere only after 500 μs. Previous experiments have also established the non-adiabaticity of the field ramp with respect to many body dynamics in the bulk [82], and it likely remains true for the lattice system.

Lifetime of pairs at low magnetic fields

The former measure highlights another problem with keeping on any kind of confinement when ramping magnetic fields out of the strongly-interacting region. During the ramp, the loosely bound $^6Li_2$ pairs are transferred into deeper bound states which have much shorter lifetimes. If confinement is tight and density is high, this problem is exacerbated. Since the volume of the cross dipole trap is small, the numbers are also low and care has to be taken such that signal to noise is not degraded past resolution.

The most dramatic manifestation of this effect came when we were experimenting with cross-dipole traps of different beam waists. Using a combination of two perpendicular beams with waists of 20 μm and a 60 μm respectively, we created a crossed dipole trap and attempted to characterize the condensate obtained using the same field ramp as before. The high densities and small trap volume resulting from such focused beams meant that switching off the COT simultaneously with the ramp down of the magnetic field still resulted in catastrophic losses (Fig. 7-6) and some short time-of-flight had to be given before starting the field ramp.

Had we left the COT on until the field had fully ramped down, the $^6Li_2$ would have fully decayed and heated, leading to the mistaken conclusion that a stable trap cannot be made from these two beams due to beam profile imperfections etc.

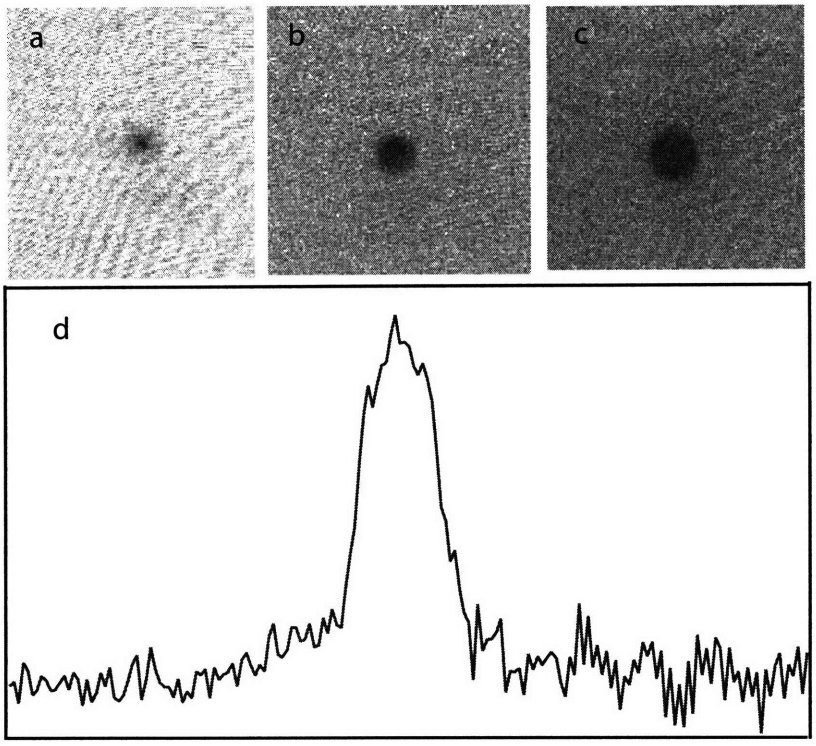

Figure 7-6: The bimodal signature for a small $^6Li_2$ condensate can be easily masked by collisional decay during the field ramp. Shown here are three absorption images of a $^6Li_2$ condensate in time-of-flight from the same crossed-dipole trap, differing only in the elapsed time t after the turn-off of the trap and before the magnetic field ramp down. (a) shows a characteristic image for $t = 0$, (b) $t = 10\mu$s and (c) $t = 50\mu$s. The strong interactions during the initial expansion quickly lowers the density, resulting in a larger but colder sample. (d) shows a twice-integrated density profile corresponding to (c) demonstrating clear bimodality.

"Squeezing out of fermions"

Another complication surfaced when we began setting up an additional one-dimensional lattice along a convenient axis to study two-dimensional systems (see Chapter 8). At the time, we were using a large crossed-dipole trap with waists of 80 μm, and trapping frequencies of ≈ 50 Hz. Upon imposition of the 1 D lattice with beam waist of 200 μm and repeating the switch-off procedure as before, superfluidity was lost and no interference fringes were seen. Puzzlingly, the same lattice beam was well-behaved with bosons.

It turns out that this loss was due to the pairs being "squeezed out" of the confining potential and into the axial extent of the lattice beam. The large admixture of atomic character in the $^6Li_2$ pairs (section 6.1) implies Pauli exclusion and the imposition of the lattice beam reduces the number of states available for occupation. If the external confinement is very shallow, the fermion pairs will be forced out. By increasing the depth of the cross-dipole trap ten-fold before applying the optical lattice, this problem was solved.

7.3.2 Definition of quantities

To facilitate further discussions, I define commonly used terms and give numerical values for the quantities used in [87]:

Fermi energy The non-interacting Fermi energy of N particles in a harmonic trap is given by

$$E_F = (6N)^{1/3}\hbar\widetilde{\omega} \tag{7.13}$$

where $\widetilde{\omega}$ is average trapping frequency. With 200,000 pairs and trapping frequencies $\omega_{x,y,z} = 2\pi \times (270, 340, 200)$ Hz, $E_F = k_B \times 1.4\mu$K in our system.

Molecular recoil energy Throughout, we will use the molecular recoil energy which is smaller than the atomic recoil by a factor of 2:

$$E_R = \frac{\hbar^2\pi^2}{4ma_L^2} = 15\text{kHz} \tag{7.14}$$

for $^6Li_2$ and $a_L = 532$nm. Similarly, lattice depth s will be quoted in units of molecular recoil. Note that quoted this way, s is a factor of 4 larger than the equivalent number for atoms in the lattice with the same optical power.

Filling factor The filling factor is the number of particles per site. Due to the external harmonic confinement, there exists a spatial variation of the filling factor, from a peak value in the center to a minimum at the edges. We will define a peak filling factor in

the unitarity regime where all our measurements have taken place and by assuming that the atoms do not move around significantly when the lattice is applied. From Eq. 4.29, this is calculated to be

$$n_p = 0.89 \approx 1 \tag{7.15}$$

Note that this is in contrast to the characteristic filling factor that exists within the literature, defined as [90, 98]

$$n_c = \frac{N_F d^3}{\zeta^3} \tag{7.16}$$

$$\zeta = \sqrt{2J/M\omega_L^2} \tag{7.17}$$

where ζ is the spatial extent of the wavefunction in the lowest band and J is the tunneling term. It is difficult for us to use this definition, since J is not clearly defined for a strongly interacting system.

Adiabaticity condition To load atoms into the ground state of an optical lattice without excitation into the higher bands, the turn on of the lattice has to be slow with respect to the energy difference to the next highest band. For a non-interacting system, this condition for a condensate with zero momentum is given by

$$|\langle i,q|\frac{\partial H}{\partial t}|0,q\rangle| << \frac{\Delta E^2(q,t)}{\hbar} \tag{7.18}$$

$$\Rightarrow \frac{dV_0}{dt} << 16E_R^2/\hbar \tag{7.19}$$

where ΔE is the energy difference between the ground state and the first excited state. Given recoil energies in the kHz, this condition is easily satisfied. For $^6Li_2$, the right hand side evaluates to 4 μs per recoil of lattice depth and our experiment easily satisfies Eq. 7.19 by ramping to 10 E_r in 20 ms.

Again, there is a caveat for a strongly interacting system as as interactions can modify the dispersion, rendering this condition invalid.

7.4 Superfluidity of $^6Li_2$ in Shallow Lattices

Notwithstanding the lack of a full theoretical understanding, for a sufficiently shallow lattice, intuition suggests that no drastic changes should occur. If we begin with a strongly-interacting superfluid of $^6Li_2$ pairs in the crossover, they should remain so when loaded into an infinitely shallow lattice. Through quantum mechanical tunneling, the superfluid

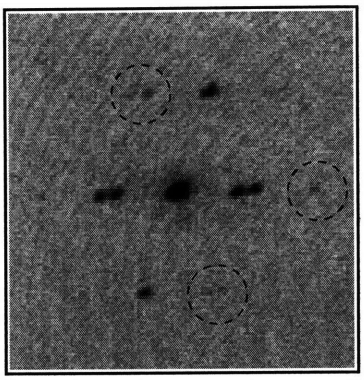

Figure 7-7: Interference fringes of ^{6}Li pairs from a three-dimensional optical lattice with $s = 4$ after 6 ms ballistic expansion. The dashed circles highlight the areas where second order momentum peaks corresponding to momentum transfers of $2\,\hbar(\mathbf{k_1}+\mathbf{k_2})$ could also be seen.

maintains a macroscopic order parameter, establishing a fixed phase difference between each well. If the lattice is suddenly switched off, this long range phase coherence manifests as sharp interference fringes after ballistic expansion, reflecting the free-momentum decomposition of the ground state in the optical lattice (Eq. 7.7). This then is the commonly used experimental signature for inferring superfluidity of atoms in an optical lattice [18].

In the experiment reported in [87], a $^6Li_2$ condensate held in the cross dipole trap is adiabatically loaded into the three dimensional optical lattice (Fig. 7-4). The lattice is linearly ramped to varying lattice heights before the switch-off procedure allows the atoms to undergo ballistic expansion.

7.4.1 Phase coherence

Fig. 7-7 shows our main result. The strikingly sharp interference peaks confirms the presence of long range phase coherence. The observed separation of the peaks in time-of-flight of $d = 2\hbar k/m$ also confirms that the relevant mass m is that of a pair, and not of isolated atoms. Assuming that the magnetic field ramp projects long range pairs into their center of mass without changing the center-of-mass momentum distribution, we have obtained evidence of superfluidity of ultracold fermions in an optical lattice.

Minimum Phase Space Density and Coherence Length

From the ratio of the width of the peaks to their separation, we can place a lower bound on the coherence length. Since this derivation neglects broadening mean-field effects, we know that it is an underestimate.

Fig. 7.4.1 (a) shows a twice integrated density profile of the interference peaks, while

(b) is a close-up of the central peak. *sep* simply scales with the time-of-flight t as

$$sep = \frac{2\hbar k_L}{m} t \tag{7.20}$$

To obtain an approximate expression for width w, we begin with the assumption of a classical thermal gas in a homogenous volume. Then coherence length is given by the de Broglie wavelength

$$\lambda_{dB} = \frac{h}{\sqrt{2\pi m k_B T}} \tag{7.21}$$

From [76], the equilibrium distribution for the velocities in the gas is just the Maxwell-Boltzmann distribution

$$f(\mathbf{v}) = n\left(\frac{m}{2\pi k_B T}\right)^{3/2} e^{-m(\mathbf{v}-\mathbf{v_0})^2/2k_B T} \tag{7.22}$$

$$\sigma_v = \sqrt{k_B T/m} \tag{7.23}$$

where n is density. Assuming perfect ballistic expansion and a negligible initial size, the spatial distribution after long time-of-flight is just $f(x \rightarrow vt)$. More specifically, the gaussian width of the spatial distribution is just

$$w = \sigma_x = \sigma_v t \tag{7.24}$$

The ratio sep/w can then be expressed as

$$\frac{sep}{w} = \frac{2\hbar k_L}{m\sigma_v} \tag{7.25}$$

$$= \frac{h}{a_L\sqrt{m k_B T}} \tag{7.26}$$

using $k_L = \pi/a_L$. Finally, substituting in Eq. 7.21 and eliminating the temperature dependence from Eq. 7.25, we obtain

$$\frac{\lambda_{dB}}{a_L} = \frac{1}{\sqrt{2\pi}}\left(\frac{sep}{w}\right) \tag{7.27}$$

With this, phase space density may be estimated by

$$P.S.D. = \lambda_{dB}^3 n_0 \tag{7.28}$$

$$n_0 = 1/a_L^3 \tag{7.29}$$

We measured the separation of the peaks to be 380μm with gaussian widths of 15μm, while $n_0 \approx 1$ from Eq. 4.29. This gives a coherence length of approximately 10 lattice

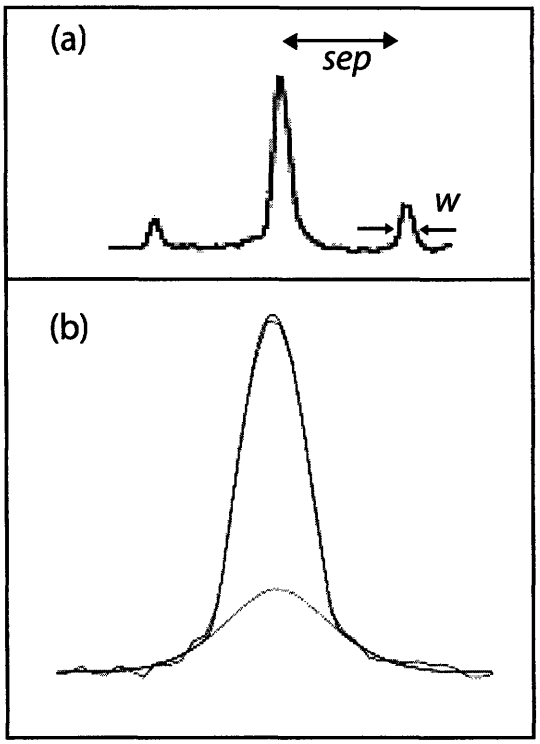

Figure 7-8: (a) Density profile of the central and first order interference peaks. The ratio of *sep/w* gives a minimum coherence length for the pairs. The width of the interference peaks was used instead of the main peak since they contained smaller numbers and had less mean-field broadening. (b) shows a close up of the central peak fitted to a bimodal distribution comprising of a gaussian and Thomas-Fermi distribution. It argues further for superfluidity of the $^6Li_2$ in the optical lattice.

sites and a corresponding minimum phase space density of 10^3, which is far in the quantum degenerate regime.

Strictly speaking, long-range phase coherence does not necessarily imply superfluidity [99, 100]. Traditionally the definition of superfluidity has instead relied on its transport properties like frictionless flow. In Chapter 8, we will describe in more detail some ongoing experiments that seek to probe the nature of the strongly interacting fermions in the lattice.

7.4.2 Density profile

In a recent work, an unambiguous way of identifying Bose condensation in an optical lattice at finite temperature was proposed [101]. The change in the momentum distribution across the condensation phase transition was calculated, taking into account both interactions and the external trapping potential, and the authors concluded that observation of a bimodal distribution of the central momentum peak can only arise from the presence of a condensate in the optical lattice. This addresses the weakness of using sharp interference peaks as proof of the superfluid state, since even uncondensed bosons in the normal state, assuming a cold enough temperature, would exhibit sharp peaks [100].

We show in Fig. 7.4.1 (b) a close up of our density profile which does indeed exhibit a bimodal distribution, further confirming that we have indeed observed superfluidity of fermions in an optical lattice.

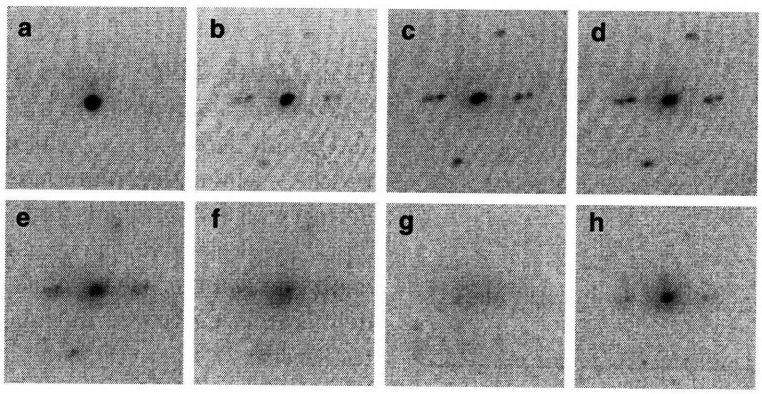

Figure 7-9: A loss of phase coherence is seen when the lattice depth is increased. Shown here are interferograms for lattice depths (a) 0 E_r , (b) 2.5 E_r , (c) 4 E_r , (d) 5 E_r , (e) 6 E_r , (f) 7 E_r , (g) 9 E_r . (g) shows how the interference fringes reappear after first ramping up to 10 E_r , before ramping down to 2.5 E_r .

7.5 Loss of Superfluidity in Deep Lattices

As the lattice depth is increased, a loss of phase coherence is seen (Fig. 7-9 (a)-(g)). Upon lowering the lattice potential, coherence returns, signaled by the reappearance of the interference peaks (Fig. 7-9 (h), Fig. 7-10).

7.5.1 Visibility

The visibility of the interference peaks can be parametrized quantitatively. Amongst experimentalists in the field, there is widespread use of the quantity

$$v = \frac{N_A - N_B}{N_A + N_B} \tag{7.30}$$

Here, N_A is the number of atoms found at a reciprocal lattice vector (interference peak) and N_B is the number of atoms found an equal distance away, but at a rotated position such that it is not at a reciprocal lattice vector. Due to the lack of perfect cubic symmetry, we introduce an alternative measure of visibility in our work, obtained from fitting the twice-integrated profile of the interference peaks (Fig. 7-11) and extracting the peak optical density from the fit parameters:

$$\text{Peak Optical Density} \propto hw \tag{7.31}$$

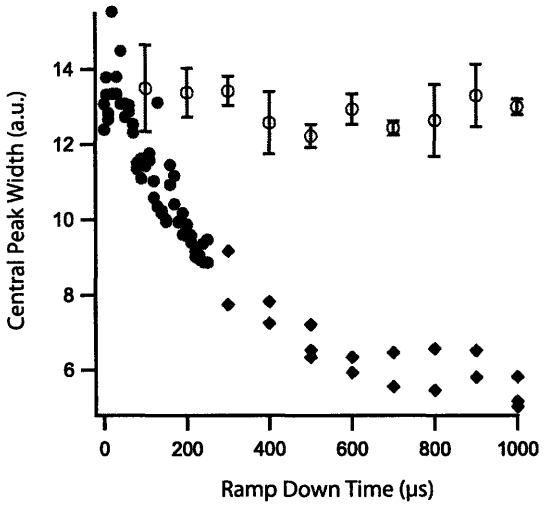

Figure 7-10: Time needed for recoherence. Filled symbols denote the central peak width of the inteferograms. Circles are gaussian widths, while the diamonds are Thomas-Fermi widths obtained from a bimodal fit. Open symbols give the gaussian width of a dephased sample, where phase coherence was deliberately destroyed during the ramp on of the lattice.

Its relation to visibility is made clear by noting that it is equivalent to the numerator in Eq. 7.30. Eq. 7.31 then defines an unnormalized visibility. Normalization was difficult for our system due to the noisy background in the data.

Using this definition, the unnormalized visibility of the interference peaks may be investigated as a function of lattice depth and magnetic field (Fig. 7-12) and hence interaction parameter $1/k_F a$. The disappearance of the peaks can be seen at 5 to 6 E_r , when the visibility falls below 0.1.

7.5.2 Superfluid-Insulator Transition

Far in the BEC limit, the loss of phase coherence of a superfluid in an optical lattice can be understood by considering on-site interactions. As the lattice depth is increased, the system has to pay an increasing energy cost to delocalize due to atom-atom repulsion. Beyond a critical lattice depth V_c, this cost becomes too high and the atoms arrange themselves in a regular array, where, for a homogeneous system, each lattice site would contain the same number of atoms. They choose not to tunnel, although in principle the barriers between sites are not yet high enough to forbid tunneling. This superfluid to a Mott-insulator transition was one of the first directly observed quantum phase transitions [18], and comes out of the Bose-Hubbard model [102, 103].

Far in the BCS limit, the superfluid-insulator transition is also easily understood. With an average filling factor of one pair of fermions (one spin up and spin down) per site, a loss of phase coherence would imply that we have a band insulator, where the fermions cannot hop, since they would then have to pay the energy cost to go to the next higher band. In order to stay superfluid, the pairing interaction Δ must be large enough to overcome the

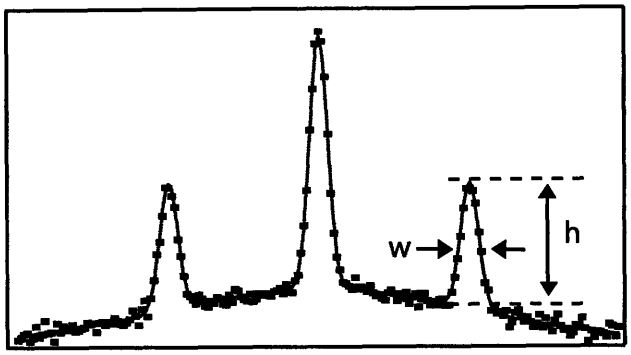

Figure 7-11: Alternative definition of visibility. Represented here is a simulated twice integrated density profile through the central momentum peak and one pair of interference peaks. By fitting gaussians to all three peaks on top of a broad gaussian background, we can extract the parameters h and w. Note that h is taken from the top of the broad gaussian background. From this, we construct a peak optical density that is proportional to hw and use it as a measure of visibility.

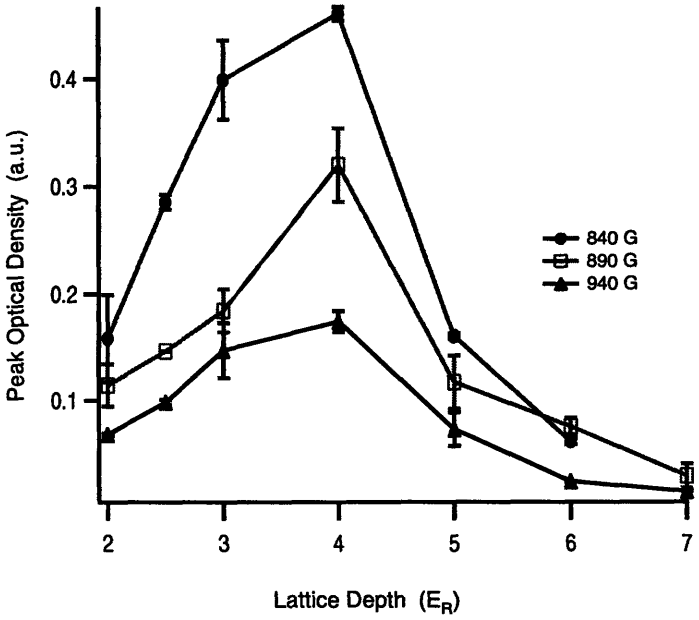

Figure 7-12: Visibility of the interference peaks as a function of lattice depth and interaction parameter. Surprisingly, the disappearance of fringes does not seem to vary with interaction strength.

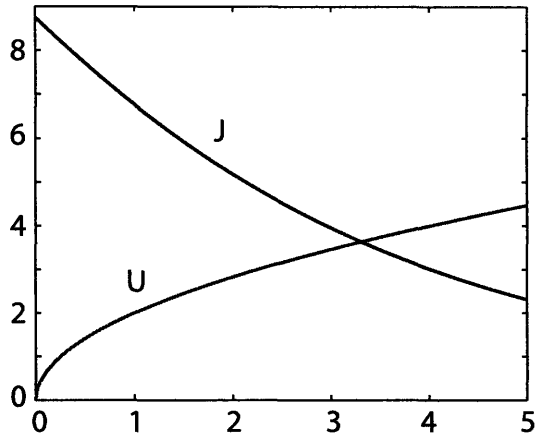

Figure 7-13: A simplistic U vs. J curve for strongly-interacting fermions. Here interaction energy U is approximated by $1/2\hbar\omega_L$ while the tunneling term J is calculated from the non-interacting band structure. Their crossing indicates the critical lattice depth at which the Mott-insulator transition is expected to occur.

band gap $\hbar\omega_L$, since only in the non-filled bands can there be number fluctuations necessary for a superfluid phase where a macroscopic order parameter exists.

These two extremes are illustrated in Fig. 7-14. What happens to strongly interacting fermions within the crossover regime is unclear, but it is likely to be an interpolation of the two. V_c for bosons has been calculated to be around 13 E_r [103], and fig. 7-13 gives a simplistic estimate of $V_c = 3E_r$ for interactions on the order of $U = \frac{1}{2}\hbar\omega_L$. Our observed value of $V_c \approx 6E_r$ falls suggestively somewhere in between the two. Recently there has been numerous of theoretical calculations [94, 95, 96] of the critical lattice depth where a strongly interacting fermionic superfluid would enter the insulating phase. Due to the strong interactions, any correct calculation will have to take into account multiple bands, greatly complicating the physical interpretation of the insulating state. However, there is reasonable agreement with at least one of them [95], and a consensus may emerge before long.

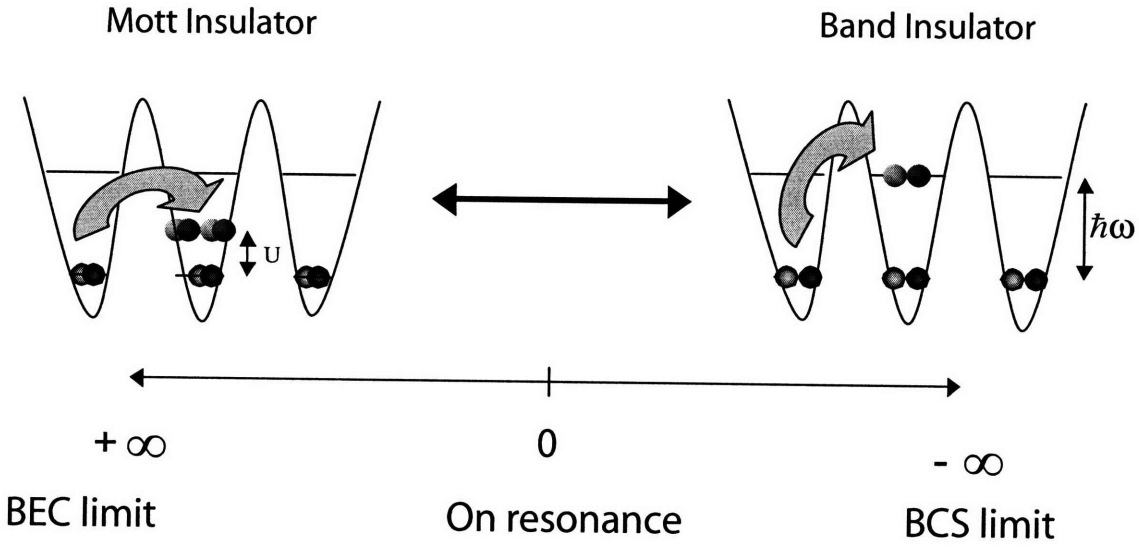

Figure 7-14: Superfluid-Insulator transition from the BEC to BCS limit for deep lattices. Far in the BEC limit, a Mott insulator occurs when interactions dominate over tunneling. Far in the BCS limit, a band insulator occurs for commensurate filling. On resonance, it is likely to be some combination of the two.

Chapter 8

Explorations

Strongly interacting fermions in optical lattices is still poorly understood and we have only scratched the surface of a blossoming field. In this chapter, I will outline our exploration of this fascinating system, summarizing some partial experiments that yielded tantalizing but inconclusive results, and discuss some future experiments that are imminent, but as yet unrealized.

8.1 Radio-frequency spectroscopy of $^6Li_2$ pairs in an optical lattice

It has been predicted that a significant shift of the position of the Feshbach resonance is possible due to additional confinement from the optical lattice [104]. The confinement shifts the energy levels of the open channel upwards and not that of the bound level, since the length scale of confinement is still much larger than the effective range of the closed channel. The magnetic field where a real two body bound state would not exist is therefore shifted. This prediction has been supported by measurements of finite binding energies above the Feshbach resonance using radio-frequency spectroscopy for 1 and 3 D lattices [105]. However, this analysis holds true only if one can treat the optical lattice as an array of harmonic potentials, valid only in the limit of deep lattices. Solving the problem for the full periodic potential is complicated, since now the center of mass and relative coordinates can no longer be separated. The obvious presence of delocalized pairs in our system as indicated by long range phase coherence suggests that a full treatment of the problem is necessary.

Nonetheless, certain qualitative behavior has to be true. At zero lattice depth, no two body bound state exists above the Feshbach resonance. In a deep lattice, one does exist. At a critical lattice depth above the Feshbach resonance, there must be a transition between these two regimes corresponding to when a bound state appears. Experimentally, one way

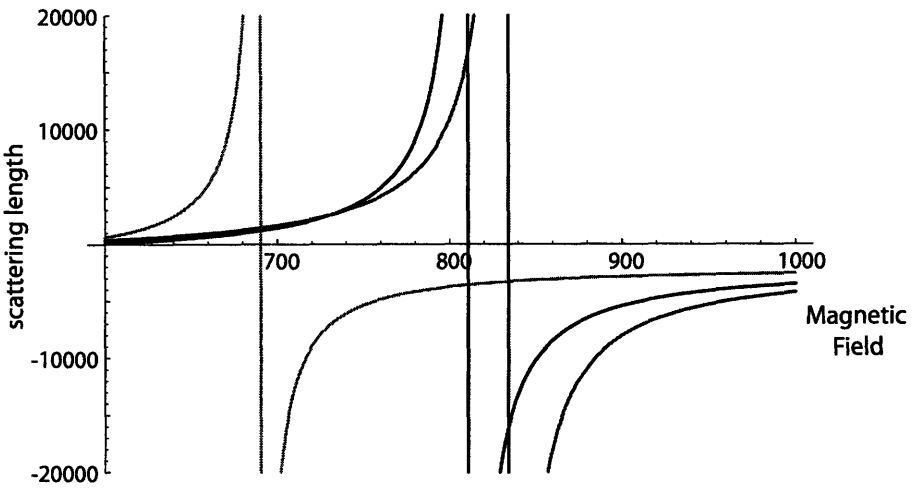

Figure 8-1: (Color in electronic version) Three s-wave Feshbach resonances are shown here, characterized by their diverging scattering length. In red is a_{12}, centered at 834 G. Here the hyperfine states of ^{6}Li is numbered in increasing order of energy (see Fig. 5-9). In green is a_{13} centered at 690 G and in blue is a_{23}, centered at 811 G [39].

of determining its presence would be to perform radio-frequency (rf) spectroscopy on the transition between one atom in the pair and an initially unoccupied state. A discrepancy from the bare transition would indicate a shift in the energy of the atom due to either mean-field or pairing effects. To disentangle the two effects requires studying their dependence on density n. A true two-body bound state would have a binding energy independent of n, while mean-field shifts scale linearly with n. If both effects are present, then at low n, the pairing shift is expected to dominate while at higher n, the mean-field shift would take over.

Unfortunately, it is experimentally difficult to vary density across a wide range, and at low densities we would begin suffering from poor signal to noise. In addition, rf measurements in ^{6}Li is complicated by the presence of broad Feshbach resonances between all three combinations of the lowest three hyperfine states (see Fig. 8-1). This implies that transitions from either state 1 or 2 to the final state 3 could still result in a strongly-interacting sample. In a tight harmonic trap (an approximation of the individual sites on an optical lattice), the solution to the two-particle problem for varying interaction strengths [106] yields a binding energy dependence on the two-body scattering length of

$$\sqrt{2}\frac{\Gamma(-E/2+3/4)}{\Gamma(-E/2+1/4)} = \frac{1}{a} \tag{8.1}$$

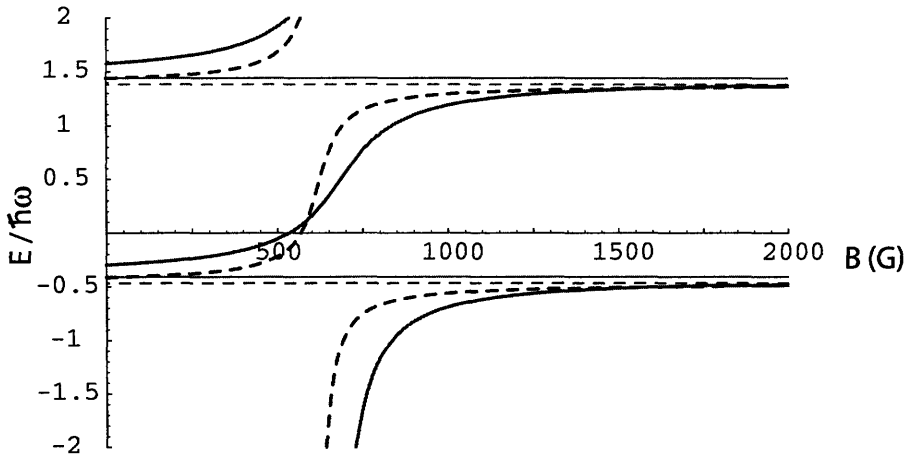

Figure 8-2: (Color in electronic version) Solid (red) line shows the energy levels of two fermions in states $|1\rangle$ and $|2\rangle$ interacting with scattering lengths given by Fig. 8-1, while dashed (blue) line shows the energy levels for atoms in states $|1\rangle$ and $|3\rangle$. For this simulation, lattice depth was 6 E_r .

The dependence of E on a is plotted in Fig. 8-2 for both the (1,2) and (1,3) state. As can be seen, there exists finite binding energy for states 1 and 3 in the vicinity of the 834 G Feshbach resonance which further complicates the interpretation of any observed rf shift. This is in contrast to the situation in the bulk phase, where no two-body bound state exists between 1 and 3 above the (1,2) resonance since the (1,3) resonance position is lower. In terms of the many body interactions, $1/k_F|a_{13}|$ is already close to 1 at 834 G, and the system is also no longer strongly interacting. Under these conditions, radio-frequency spectroscopy has already been used extensively to measure the binding energy of the $^6Li_2$ pairs [72, 107].

Nonetheless, we present here some very preliminary rf spectra of $^6Li_2$ pairs in a lattice in Fig. 8-3. We measure a confinement induced shift of 11 kHz in a 6 E_r deep lattice, which is much less than the value of 78 kHz calculated from Eq. 8.1. As a sanity check, we measured our transition frequencies in the bulk phase of 25 kHz at 822G and 411 kHz at 768G, confirming that the binding energies are larger further away from the resonance, even though the absolute values seem to be off by a factor of two from the expected values [72]. While the results are suggestive, interpretation of the spectra is complicated for the reasons discussed above and we stop short of drawing any firm conclusions.

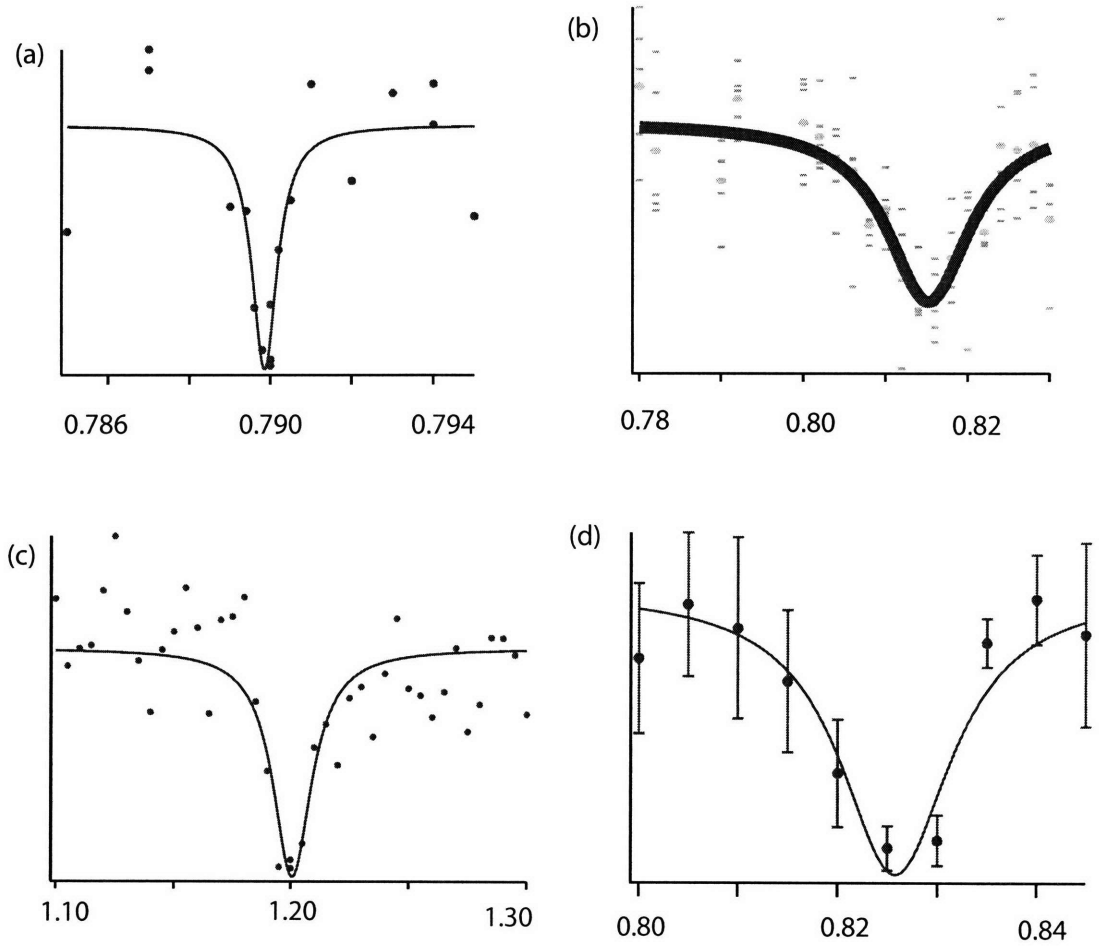

Figure 8-3: Rf spectra on the $|2\rangle \rightarrow |3\rangle$ transition. (a) is the bare atomic line at 81.7899(1) MHz, where a pure sample of $|2\rangle$'s and no $|3\rangle$'s are present. Note how much narrower the line is relative to all the others. (b) shows spectra taken for a $^6Li_2$ condensate at 822G, giving a shift of the transition frequency of $E_b = 25.3(7)$ kHz. (c) is again a $^6Li_2$ condensate, but at 768G, with $E_b = 411(2)$ kHz, and (d) is taken with the pairs localized in a lattice with 6 E_r at 822G, with $\Delta\nu = 11(1)$ kHz.

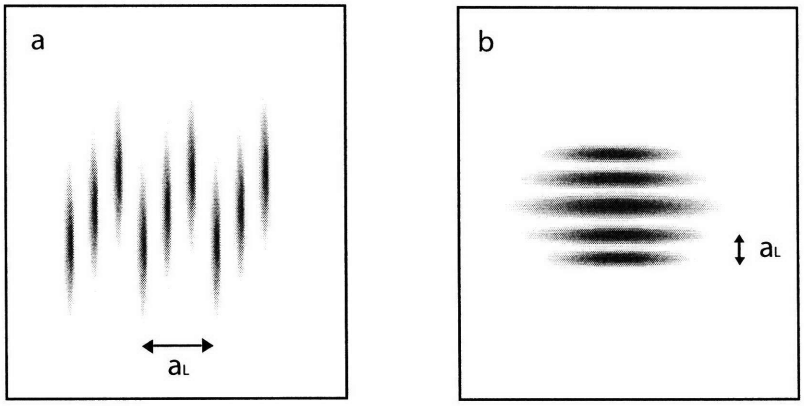

Figure 8-4: By using only two (**a**) or one (**b**) retroreflected beams, it is possible to enter the 1 or 2 D regime and study low dimensional physics. While this creates an ensemble of such systems, it has the advantage of signal amplification.

8.2 $^6Li_2$ pairs in two dimensions

On a different front, optical lattices allow easy access to the lower dimensions. A three-dimensional system can be made kinematically one (two) dimensional by freezing out two (one) degrees of freedom. In the direction of tight confinement, $\hbar\omega$ can be much greater than either k_BT or E_F, and the atoms stay in the ground state since they do not have sufficient energy to reach the next higher state. Since the length scale of the lattice spacing is set by the wavelength of the light which is typically on the order of a few hundred nanometers, we can get very tight confinement using very little optical power. Finally, optical lattices tends to create an ensemble of low dimensional systems (Fig. 8-4), which has the additional advantage of boosting the signal to noise ratio.

The two-dimensional case is a special one. The introduction to this thesis has already pointed out their relevance to the high T_c cuprates. By using a one-dimensional lattice, we can create precisely this structure, with the additional advantage that we can tune the interlayer coupling from zero through to infinitely strong. Studies on the behavior of the $^6Li_2$ pairs in the BEC-BCS crossover in two dimensions is ongoing, and I highlight here a number of issues that we would like to resolve.

8.2.1 Phase coherence

In an optical lattice, the possibility of tunneling across different lattice sites complicates the definition of dimensionality. If atoms tunnel, the system might only be quasi-2D and phase coherence could be established across the different lattice sites in the third dimension.

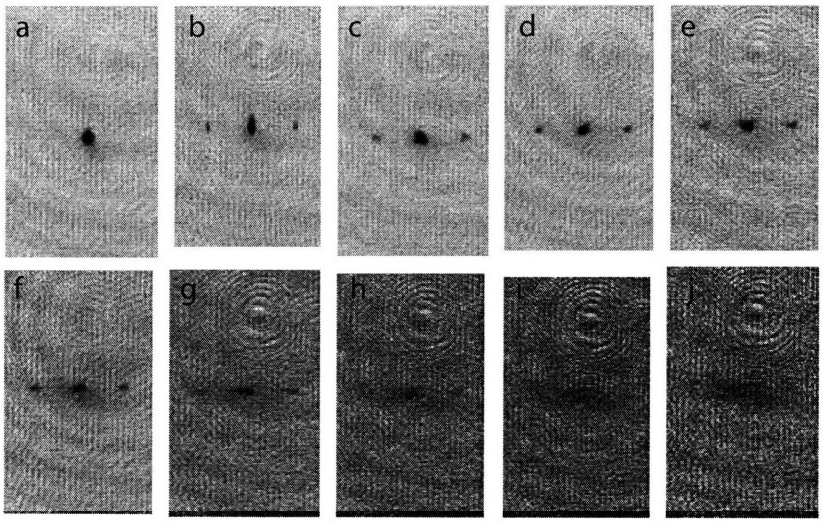

Figure 8-5: Loss of phase coherence in a 1D lattice. Images shown are for lattice depths ranging from 0 (a) to 36 E_r (j), at intervals of 4 E_r .

Kinematically we are easily in the 2D regime since E_F is on the order of one E_r and within a few recoil we would have satisfied the kinematic criterion.

We determine when the system might enter the true 2D regime by investigating the disappearance of the interference fringes in a 1D lattice. Qualitatively a similar loss of coherence is observed as in the situation with a three dimensional lattice, although the critical lattice depth V_c differs (see Fig. 8-5). Without detailed analysis, V_c appears to fall between 20 to 30 E_r . Upon ramping the lattice back down, a cold condensate is regained, indicating once again that the atoms stay in a low entropy state.

We also changed the lattice geometry and made a 1 D lattice by interfering the ingoing left and right lattice beams which are at 90 degrees to each other. The two beams are set to have zero-detuning and are phase locked at the frequency source, thereby interfering to give a lattice spacing of 752nm. From Fig. 8-6, the phase coherence seems to be lost at lower lattice depths, perhaps between 15 and 18 E_r . While our observations were not conclusive, it could have been due to additional heating caused by phase noise between the two different beams that form the lattice.

At this point, we might be tempted to assume that the pairs are unable to tunnel past$s$ = 25 E_r . However, the non-interacting tunneling amplitude t given by Eq. 7.9 evaluates to give a characteristic tunneling time scale of 53 ms. This is comparable to the rate at which we ramp up the lattice, and is certainly not long relative to the time scale of the experiment.

However, the determination of the microscopic parameters U and J of the Hubbard model in terms of the macroscopic experimental parameters a and s is not trivial for a

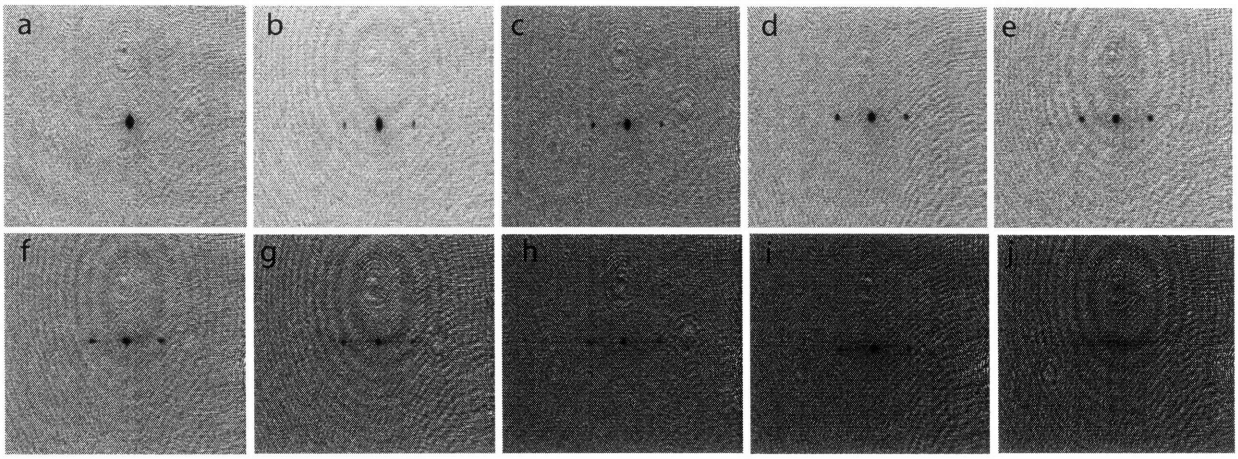

Figure 8-6: Loss of phase coherence in a 1D lattice with a larger lattice spacing. Images shown are for lattice depths ranging from 0 (a) to 18 E_r (j), at intervals of 2 E_r .

strongly interacting system. For a weakly interacting system of pairs, tunneling amplitude J is expected to vary as t^2/U which could be much less than t for $U > t$ due to the presence of virtual transitions of one half of the bound pair to a neighboring site [88].

One intriguing cause of the loss of coherence in a lattice system with finite tunneling amplitude is the establishment of a Mott phase, where atoms choose not to tunnel due to the energy cost of on-site interactions. For a bosonic system, this is not predicted to occur in a 1 D lattice since U can never become large enough to overcome t before the tunneling time scale becomes longer than the experiment. For superfluid fermions however, this transition is possible because of the reduction in the tunneling amplitude [108].

8.2.2 Modification of scattering properties

If we were to attain the two-dimensional limit, one of the first questions that could be asked is what happens to the scattering when $a > a_{ho}$? This in turn determines properties as varied as dimer lifetime, mean-field energy and superfluid pairing within the BEC-BCS crossover regime. Preliminary investigations of the lifetime suggested that they are enhanced relative to the 3D case, but effects due to the additional confinement have yet to be be fully sorted out.

8.2.3 A new setup for two-dimensional studies

A recent modification to our setup could open to door to some answers. A new retro-reflected lattice with a large beam waist of 200 μm was set up to overlap with the imaging axis (along with beams 1 and 2 in Fig. 7-4), parallel to the axis of the uniform bias field of the Feshbach resonance. While complicated to implement, this new geometry granted us two new capabilities:

- A magnetic field gradient can now be applied along the lattice direction, enabling studies of transport along the lattice and probes of its excitation spectrum. The presence of undamped Bloch oscillations could yield insight into the tunneling amplitude, and a resonance in the excitation spectrum would confirm the presence of a Mott state.

- Imaging perpendicular to the 2 D planes. The radial extent of the strongly interacting superfluid can be obtained via absorption imaging of the atoms confined in the lattice, giving a direct measurement of the mean-field energy within the crossover regime. A careful correlation of the presence of a condensate with phase coherence across lattice sites could then yield insight into whether or not interference fringes disappear due to lack of tunneling and dephasing, or due to the destruction of the superfluid.

8.3 $^6Li_2$ pairs in one dimension

Theoretical understanding of one dimensional systems is often better since the systems are simpler and exact analytics can be obtained, making experiments in 1D more predictable. Particularly for strongly interacting systems where computations in higher dimensions might be difficult, 1 D systems would be a good first step.

One of the more intriguing theoretical predictions involve pairing with a finite momentum when the Fermi seas of the two spin states are not balanced. Also known as the Fulde-Ferell-Larkin-Ovchinnikov (FFLO) state [109, 110], it postulates that the in the presence of an imbalance, some of the fermions can pair with finite momentum, giving rise to a spatially varying order parameter. This would truly be a novel superfluid phase. Beautiful work with imbalanced systems have already been done in 3 D [111] but so far observations of finite momentum pairing have been elusive. In 1 D however, there exist predictions [112] that the fraction of finite momentum pairs would be much higher and therefore much easily observable. A qualitative signature would involve observing a phase separation between the fully paired fraction and the excess fermions, where contrary to the 3D scenario, the trapped spatial distribution would show the fully paired fraction residing *outside* the spin-polarized fraction.

8.3.1 Possible setup for seeking the FFLO state in one dimension

By merely blocking the top lattice beam and tightly confining with the left and right retro-reflected lattice beam, we can have a system of 1 D tubes with long axis aligned vertically. By performing phase contrast imaging perpendicular to the tubes, the relative positions of the polarized and unpolarized fractions would yield a clear qualitative signature of the FFLO state in 1D.

Chapter 9

Conclusion

9.1 Final thoughts

It is with bittersweet feelings that I end this thesis and my stint as a graduate student. My departure coincides with that of all others who endured the rigors and vagaries of a new-old machine. With our departure goes the vast store of knowledge accumulated from experience, leaving behind distillates like this one.

Yet I believe the best is yet to be. During my tenure, I have witnessed and participated in the lab's acquisition of a vision. Now the changing of the guard liberates the new generation to realize this vision without the encumbrance of history. My doctorate was one of construction and achievement. I wish for those after me to have one of discovery and understanding.

9.2 Future challenges

The main goal of this lab is to harbor the ideal "artificial crystal", infinitely flexible in geometry and tunability of parameter, making possible fast and reliable simulations of various Hubbard models from condensed matter physics. Before that can be achieved however, there are several more challenges. Here I outline a few:

9.2.1 Accessing the repulsive branch

We currently do not have access to the half of the phase space where temperatures are low and $U > 0$. Close to the broad Feshbach resonance where the coldest temperatures of $<0.1\ T/T_F$ were reached and Bose-Einstein condensates of $^6Li_2$ observed, the strong coupling between the atomic and molecular states will always project the long range dimers into deeply bound molecules when we ramp across the resonance. The challenge is to break these molecules without increasing entropy. Possible methods include using Raman

transitions and resonant magnetic field modulation to couple back from the molecular to the atomic manifold.

9.2.2 Thermometry

Measurement of temperature in an optical lattice has to be improved. During adiabatic ramp on of the lattice, some heating is likely incurred, as evidenced by an increased thermal fraction when the lattice is ramped back down again. In this thesis, I have avoided quantifying the temperature within the lattice for want of a good thermometer. This has to change if accurate mapping of the system's phase diagram is to be done. Currently, the best methods of quantifying temperature involves measuring filling within each lattice site [105].

9.2.3 Detection

Finally, various detection techniques for the expected phases have to be developed. Noise correlation [113] has been proposed as an excellent candidate for observing the ordering of atoms in an optical lattice, but this is unlikely to work easily for ^{6}Li systems due to the large region of strong interactions and the finite time required to exit it. Another requirement for this technique - shot noise limited imaging, is also not currently within our grasp, though improvements are ongoing.

A more promising method might be to perform Bragg spectroscopy. By shining in light at angles that fulfill the Bragg condition for constructive interference in the reflected signal, the angle of light detection could also reveal the ordering of atoms within the crystal.

Appendix A

Amplification of Local Instabilities in a Bose-Einstein Condensate with Attractive Interactions

This appendix contains a reprint of Ref. [50]: J.K.Chin, J. M. Vogels, W. Ketterle, *Amplification of Local Instabilities in a Bose-Einstein Condensate with Attractive Interactions*, Physical Review Letters **90**, 160405 (2003).

Amplification of Local Instabilities in a Bose-Einstein Condensate with Attractive Interactions

J. K. Chin, J. M. Vogels,* and W. Ketterle†

Department of Physics, MIT-Harvard Center for Ultracold Atoms, and Research Laboratory of Electronics, Massachusetts Institute of Technology, Cambridge, Massachusetts 02139

(Received 20 December 2002; published 24 April 2003)

We study the collapse of large homogeneous Bose-Einstein condensates due to intrinsic attractive interactions. We observe the amplification of a local instability by seeding a momentum state $\mathbf{p}$ and suddenly switching the scattering length negative via a Feshbach resonance. We also observe the appearance of atoms in the conjugate momentum state as required by momentum conservation. For large condensates, the time scale for this depletion process becomes faster than that for global collapse.

DOI: 10.1103/PhysRevLett.90.160405 PACS numbers: 03.75.Kk, 34.50.–s, 32.80.Pj

Our current understanding of the collapse of Bose-Einstein condensates (BECs) with attractive interactions is incomplete. While the experiments in ^{7}Li provided many insights into the formation kinetics and stability [1], it was not until the discovery of externally induced Feshbach resonances [2] that it became possible to tune the value of the scattering length and study in detail the effects of an attractive mean field potential. This technique was used by Donley *et al.* to study ^{85}Rb with a negative scattering length, and they have observed rich dynamics inherent in the collapse of the condensate. Among the most intriguing observations were the formation of low energy "bursts" which were ejected out of the condensate [3]. While theoretically the enhancement of quantum fluctuations could give rise to such phenomena [4–6], there is currently no consensus on the exact mechanism by which it occurs.

Thus far, theoretical developments have been limited by having only one experimental testing ground. The experiments using ^{85}Rb were done using small condensates ($\sim 15\,000$ atoms), where the attractive mean field energy μ is comparable to the $\hbar\omega$ level spacing of the harmonic trapping potential. In this paper, we study the collapse of large sodium condensates far in the Thomas-Fermi regime ($|\mu| \gg \hbar\omega$), where the spatial profile of the condensate is relatively homogeneous. Much of the dynamics of such a system is then described by local phenomena. When the interactions become attractive, Yurovsky [5] predicts that local instabilities with momentum on the order of the (imaginary) speed of sound will undergo exponential growth. Simultaneously, momentum conservation requires atoms to be generated in conjugate momentum states. Since amplification happens on the time scale of the chemical potential h/μ, the resulting quantum evaporation of the zero momentum condensate atoms can happen faster than the global collapse where the whole condensate "implodes."

We probe for local instabilities by seeding a particular momentum state with an initial population, then suddenly switching the scattering length negative via a Feshbach resonance. At the same time, the trapping potential is turned off, so all subsequent dynamics are due only to the intrinsic attractive interactions. The resulting amplification and the associated generation of atoms in the conjugate momentum state verifies the theory. We end with a discussion on the different collapse time scales of competing processes and show that, for large condensates, this decay channel becomes dominant.

The theoretical basis for the amplification of local instabilities is the dispersion relation for the elementary excitations in a Bose-Einstein condensate:

$$\epsilon(\mathbf{p}) = \sqrt{\frac{|\mathbf{p}|^2}{2m}\left(2n_0U + \frac{|\mathbf{p}|^2}{2m}\right)}, \tag{1}$$

where n_0 is the density, $U = 4\pi\hbar^2 a/m = \mu/n_0$ is the contact potential, a is the scattering length, and m is the atomic mass. For an elementary excitation whose momentum satisfies $|\mathbf{p}|^2/2m < 2|\mu|$, an instability forms when $\mu < 0$ (i.e., $a < 0$) and oscillatory behavior gives way to exponential growth or decay. A formal derivation gives the evolution of these low momentum modes as

$$\langle \xi_{\mathbf{p}}^{\dagger}\xi_{\mathbf{p}}\rangle(t) = \frac{|Un_0|^2}{\hbar^2\lambda^2(\mathbf{p})}\sinh^2[\lambda(\mathbf{p})t], \tag{2}$$

where the growth rate $\lambda(\mathbf{p})$ is given by $|\epsilon(\mathbf{p})|/\hbar$ [Eq. (1)] when $a < 0$ [5] and $\xi_{\mathbf{p}}$ is the destruction operator for mode $\mathbf{p}$. The instability of the mode pair $(\mathbf{p}, -\mathbf{p})$ results in correlated growth, where the creation of an atom in the $+\mathbf{p}$ state is accompanied by the creation of an atom in the $-\mathbf{p}$ state. A similar phenomenon is also responsible for the four wave mixing process observed in [7,8]. At higher momentum, the energy becomes real again as the excitations now have enough kinetic energy to stabilize them against the attractive interactions.

In our experiments, we created large cigar-shaped sodium condensates in the $F = 1$, $m_F = -1$ spin state with typical atom numbers of $\sim$30 million and peak densities of 3×10^{14} cm^{-3} in a Ioffe-Pritchard magnetic trap. Following this, they were adiabatically loaded into a mode-matched 1064 nm cylindrical optical dipole trap with trapping frequencies of 250 and 2 Hz and held for 1 s

to allow transient excitations to damp out. In the next 117 ms, the axial magnetic field was ramped up to an intermediate value just short of the 1195 G Feshbach resonance [9]. Two pairs of coils coaxial with the condensates contributed to the bias field: The bias coils produced a large field of ~1200 G and the pinch coils produced a small field of ~ − 8 G. Since their mutual inductance was small, the small pinch coils could be switched off suddenly to jump up the field in under 10 μs with a negligible adverse effect on the bias field ($\leq$ 1 G). By changing the intermediate field value, we were also able to tune the scattering length a continuously from the background scattering length a_0 to zero to arbitrary negative values. The reproducibility of the resulting magnetic field was 0.4 G. At this point, the condensates were slightly compressed by a small axial magnetic field curvature, giving them radial and axial dimensions of ~15 μm and 1.5 mm, respectively, and a speed of sound $c = \sqrt{Un_0/m}$ of 8 mm/s.

We imprinted a low momentum excitation onto a stable condensate ($a > 0$) using a two photon optical Bragg transition to couple atoms from the zero momentum state to a low momentum state $\mathbf{p}$ [10]. The Bragg beams were pulsed on for 400 μs and were directed at an angle of 15° and 20°, respectively, from the long axis of the condensate, creating phonons propagating with a momentum of $m \times 2.5$ mm/s in a predominantly radial direction. With this momentum $\mathbf{p}$, the minimum value of $|a|$ required for amplification to happen is estimated to be −0.06 nm. The beams were red-detuned from the sodium D_2 line by 3 nm to minimize Rayleigh scattering, and had a frequency difference of $\Delta\omega = 2\pi \times 700$ Hz.

At this point, we changed the scattering length a suddenly and entered the Feshbach resonance by turning off the pinch coils. This technique reduced the time available for three-body decay, thereby overcoming the problematic high loss rate first observed by Inouye *et al.* [2] and gave us a well-defined initial condition similar to that in [3]. At the same instant, we also turned off the optical trapping potential to allow the system to evolve under its intrinsic attractive interactions. After a variable time of 0 to 1 ms, the magnetic fields were switched off, causing the scattering length to become positive again. Following 6 ms of ballistic expansion, a pump pulse from $F = 1$ to $F' = 2$ was applied. Radial absorption images providing the momentum distribution of the condensates were taken on the $F = 2$ to $F' = 3$ cycling transition .

The images in Fig. 1 probe the radial dynamics of the condensates and provide dramatic visual verification of quantum evaporation. Figure 1(a) shows the $+\mathbf{p}$ excitations moving out of the condensate without any amplification. In contrast, Fig. 1(b) was taken after the condensate had been held at $a = -0.82$ nm for 600 μs. Not only was the number of atoms in the $+\mathbf{p}$ momentum state significantly amplified, it was accompanied by the formation of excitations in the $-\mathbf{p}$ momentum state, here

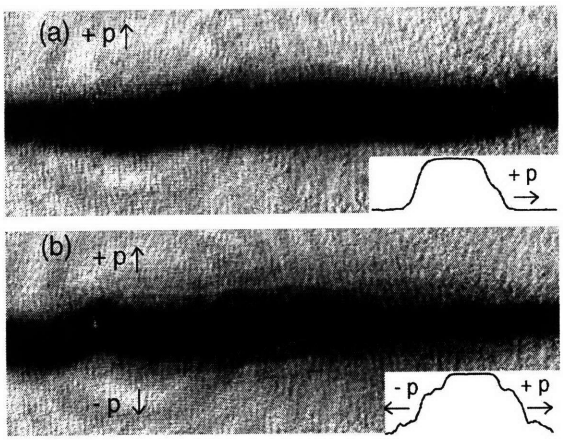

FIG. 1. Amplification of unstable excitations in a BEC with $a < 0$. In (a), the unamplified $+\mathbf{p}$ excitations are shown moving out of the condensate after 6 ms ballistic expansion. In (b), the $+\mathbf{p}$ excitations have been amplified and are accompanied by the formation of $-\mathbf{p}$ excitations after 600 μs of hold time at $a = -0.82$ nm. The field of view is 960 μm by 100 μm. The insets show a radial optical density profile in arbitrary units averaged over a ~100 μm long section of the condensate which was relatively uniform.

seen moving out of the condensate in the opposite direction. These observations clearly demonstrate the instability of a condensate with negative scattering length.

Because of the large aspect ratio of our condensates, only part of the condensate could be imaged at high magnification. However, since the $+\mathbf{p}$ and $-\mathbf{p}$ excitations were created predominantly in the radial direction, this was not a limitation. The small "kinks" that were also apparent in our condensate are most likely a result of imperfections in our optical dipole trap. Yet, rather than degrade the signal, they highlight the parallel contours between the condensate and the ridge of excitations as atoms move out with a definite momentum.

In order to perform more quantitative tests of this phenomenon, we first characterized the negative scattering length dependence on the field by directly probing the strength of the attractive interactions. As before, optically trapped condensates close to a Feshbach resonance were prepared. The confining infrared laser beam was then replaced with a repulsive 3 nm blue-detuned "antitrap" beam as we simultaneously jumped to negative scattering lengths. At the right intensity I, the antitrap beam provided the correct amount of repulsive dipole force needed to compensate for the attractive interactions within the condensate and suppressed any global contraction of size. However, this is an unstable equilibrium and any sloshing of the condensate or misalignment of the laser beam caused the condensate to be repelled. Therefore the antitrap was fine aligned to milliradian accuracy such that a condensate with $a > 0$ was ripped apart radially into a hollow cylinder. Using this method, we were able to stabilize an attractive condensate for 0.2 to 2 ms, depending on $a(B)$, before unavoidable losses became significant.

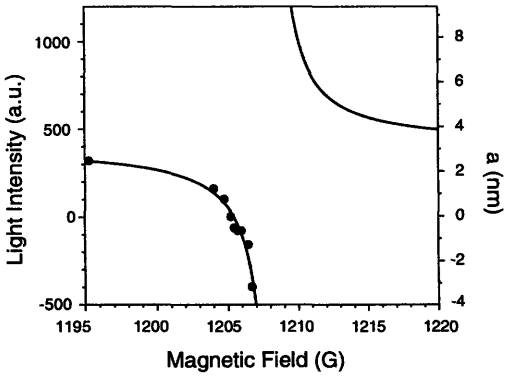

FIG. 2. Characterization of the Feshbach resonance. The light intensity needed to balance out the interatomic interactions gives the dependence of the scattering length on magnetic field. The solid line is a fit to the data.

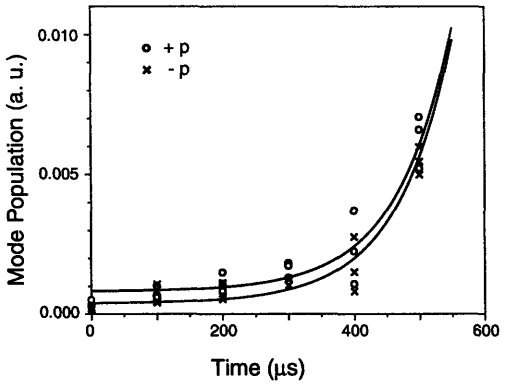

FIG. 3. Amplification of excitations in a BEC with $a < 0$. The growth of the normalized mode population in both $+\mathbf{p}$ and $-\mathbf{p}$ modes as a function of hold time at $a = -1.35$ nm is fitted to an exponential dependence according to Eq. (2), which gave a common growth rate of 5.89 ± 0.83 ms^{-1}. A variable offset accounted for the initial seeding of the $+\mathbf{p}$ mode.

The radial dimension was used to monitor the mechanical dynamics of the condensate occurring on the 250 Hz time scale of the trap frequency. For minimal distortion of the spatial image, absorption images were taken after only 2 ms of ballistic expansion necessary for the high magnetic fields to die out.

In equilibrium, $a \propto F_{\text{attractive}} = F_{\text{repulsive}} \propto I$, and we obtain the scattering length dependence on the magnetic field by plotting I vs B (Fig. 2). A red-detuned laser beam with a similar detuning of 3 nm was employed to obtain the points for positive a. By fitting the expected Feshbach curve $a(B) = a_0[1 + (\Delta B)/(B - B_0)]$ to our data, we find the width ΔB of the resonance to be (2.4 ± 0.4) G which determines the range of the magnetic field we have to work within [11]. Here, $a_0 = 3.3$ nm is the triplet scattering length at high fields [12].

A quantitative analysis of the growth in the $+\mathbf{p}$ and $-\mathbf{p}$ modes was performed by monitoring their occupation number as a function of hold time in the attractive regime (Fig. 3). The number count per mode was normalized to the number of atoms in the condensate at the end of the hold time to account for the high loss of atoms during this process due to inelastic collisions [13]. The maximum duration of amplification was limited by the lifetime of the condensate, which was about 600 μs for $a = -1.35$ nm. Following Eq. (2), an exponential dependence was fitted to the data, yielding a common growth rate of $\lambda = 5.89 \pm 0.83$ ms^{-1} for both modes. This agrees well with the theoretical value of 5.57 ms^{-1}, estimated using our initial mean field of $h \times 5$ kHz.

We also investigated the dependence of the growth rate on the strength of the interactions. By varying the scattering length and extracting λ as above, we observed a strong increase of λ with $|a|$ (Fig. 4). A fit to the theoretical prediction $\lambda(\mathbf{p}) = b_1\sqrt{|a| - b_2}$ [Eq. (1)] yielded the fit parameters $b_1 = (1.11 \pm 0.14) \times 10^8$ nm$^{1/2}$ ms^{-1} and $b_2 = 0.078 \pm 0.04$ nm, in agreement with theoretical estimates of 1.55×10^8 nm$^{1/2}$ ms^{-1} and 0.06 nm, respectively. For this sequence of measurements, the initial mean field was $\mu = h \times 4$ kHz. The large error bars reflect the high sensitivity of the dynamics to the magnetic field. In particular, the inelastic loss rates as a function of a have not yet been well characterized, which limits the accuracy of our data.

The results presented here prove conclusively that quantum evaporation is part of the complex dynamics that occur during the collapse of an attractive condensate. While we select a particular mode for observation, the effect is predicted to happen for all modes satisfying $|\mathbf{p}|^2/2m < 2|\mu|$. At short times, the pairwise emission of atoms also implies that the number of atoms in the conjugate mode pairs will be exactly correlated, although as the condensate becomes increasingly depleted, higher order effects will degrade the correlation [5].

Since quantum evaporation is intrinsic to the condensate, a natural question to ask is how large a part it plays in the unperturbed collapse of the condensate. From [5], the depletion of the condensate density n_0 is given by

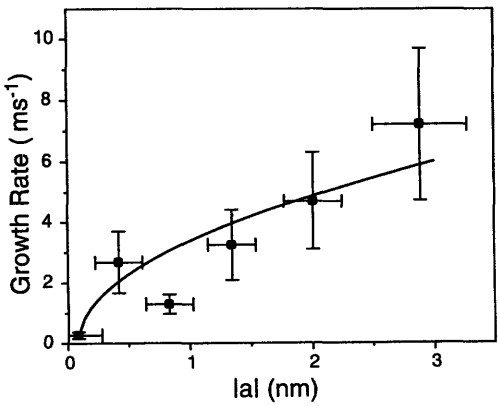

FIG. 4. Growth rate of excitations in a BEC with $a < 0$. The rate increases with the magnitude of the negative scattering length $|a|$. The solid line shows a best fit to the predicted $b_1\sqrt{|a| - b_2}$ dependence.

$$\dot{n}_0 = -4\sqrt{\frac{2\pi\hbar}{mt}}a^2 n_0^2 \exp(8\pi\hbar|a|n_0 t/m). \quad (3)$$

Using our parameters, we extract the time $t_{1/e}$ taken for n_0 to decay to $1/e$ of its original value and compare it to the observed time taken for the condensate to decay without initial seeding until it is no longer discernable (using a visibility threshold of about 10% to 20%) in Fig. 5. As both the number of unstable modes and the amplification rate increase with a, there is a significant decrease of $t_{1/e}$ with $|a|$. We also considered the effect of the initial quantum depletion ($\sim 1\%$, [14]) on $t_{1/e}$, but concluded that its impact is small.

In addition, we compare the observed collapse time to the decay time predicted for global collapse. This implosion corresponds to the unstable monopole mode and may be qualitatively described by Eq. (1) if we assume a momentum equal to $\hbar$ times the inverse size of the condensate. However, the global collapse is more accurately described by accounting for the inhomogeneous spatial profile of the condensate. The inherent pressure gradient will cause the condensate to collapse inwards and the resulting compression causes the density to increase and sharply enhance the three-body recombination loss rate, which goes like n_0^2. We model the radial evolution using the mean squared radius $R = \int r^2|\ (r)|^2 r\,dr$. For our cylindrical condensates with an aspect ratio of 100:1, an analytical solution for the resulting 2D dynamics exists [15,16], given by $\ddot{R} = 4(\frac{E}{m} - \omega^2 R)$, where E is the total energy of the system. Since $\omega = 0$ and $\frac{da}{dt} = 0$ in our experiments, E is conserved and determined from initial conditions. The time taken to reach $R = 0$ is

$$t_{\text{decay}} = \frac{1}{\omega_0}\sqrt{\frac{a_0}{|a|}}. \quad (4)$$

Equation (4) is also plotted in Fig. 5 and its intersection with $t_{1/e}$ separates the graph into two domains. For small $|a|$, global collapse is predicted to dominate over quantum evaporation while the converse is true at larger $|a|$. This is explained by noting that the decay of the condensate is dominated by the amplification of unstable modes with $\mathbf{p}_{\max} = \sqrt{2}m|c| = \hbar/\xi$, where ξ is the value of the (imaginary) healing length [Eq. (1)]. When ξ is comparable to the condensate size, the local description is invalid and global collapse occurs. In the Thomas-Fermi limit, however, ξ is small and local instabilities deplete the condensate much faster than global collapse. This is consistent with our observations in Fig. 5. We were unable to study the condensate lifetime at even more negative scattering lengths since the condensate then decayed almost instantaneously. To realize a global collapse time much slower than $t_{1/e}$ would require a combination of a weak trap with a high number of atoms, which is currently out of reach.

In conclusion, we have shown that large condensates far in the Thomas-Fermi regime undergo amplification of local instabilities when their scattering length becomes negative. We have studied the dependence of amplification rate on the magnitude of the negative scattering length and found reasonable agreement with the theory. For our parameters, this quantum evaporation process becomes faster than the global collapse.

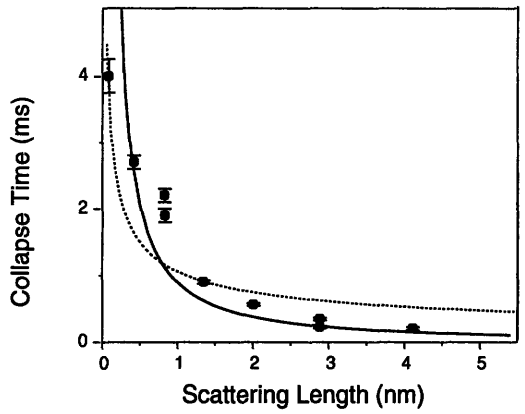

FIG. 5. Time scales for BEC decay. The observed collapse time is compared to the time taken for the condensate density to fall to $1/e$ of its original value ($t_{1/e}$) due to instability amplification [solid curve, Eq. (3)] and the expected t_{decay} for global collapse [dashed curve, Eq. (4)].

We thank K. Xu, T. Mukaiyama, and J. R. Abo-Shaeer for experimental assistance, J. Anglin for valuable comments, and A. E. Leanhardt and Z. Hadzibabic for critical reading. This work was funded by ONR, NSF, ARO, NASA, and the David and Lucile Packard Foundation.

*Present address: Laboratoire Kastler Brossel, ENS, Paris.
†Group website: http://cua.mit.edu/ketterle_group/

[1] J. M. Gerton *et al.*, Nature (London) **408**, 692 (2000).
[2] S. Inouye *et al.*, Nature (London) **392**, 151 (1998).
[3] E. A. Donley *et al.*, Nature (London) **412**, 295 (2001).
[4] R. A. Duine and H. T. C. Stoof, Phys. Rev. Lett. **86**, 2204 (2001).
[5] V. A. Yurovsky, Phys. Rev. A **65**, 033605 (2002).
[6] E. A. Calzetta and B. L. Hu, arXiv:cond-mat.
[7] L. Deng *et al.*, Nature (London) **398**, 218 (1999).
[8] J. M. Vogels *et al.*, Phys. Rev. Lett. **89**, 020401 (2002).
[9] J. Stenger *et al.*, Phys. Rev. Lett. **82**, 2422 (1999).
[10] J. Stenger *et al.*, Phys. Rev. Lett. **82**, 4569 (1999).
[11] We observe the resonance around 1208 ± 10 G, which agrees with the theoretical value within the systematic error of the magnetic field calibration which was done at low fields using rf spectroscopy.
[12] C. Samuelis *et al.*, Phys. Rev. A **63**, 012710 (2000).
[13] This is an approximation, since the loss rates for condensate and noncondensate atoms are different due to quantum statistics.
[14] K. Huang, *Statistical Mechanics* (Wiley, New York, 1987).
[15] Y. Kagan *et al.*, Phys. Rev. A **54**, R1753 (1996).
[16] Y. Kagan *et al.*, Phys. Rev. Lett. **79**, 2604 (1997).

Appendix B

Bogoliubov calculations

Beginning from the Bogoliubov transformation Eq. 3.7 and the Hamiltonian in diagonal form

$$H = \varepsilon(q) b_q^\dagger b_q,\ \varepsilon(q) = \sqrt{c^2 q^2 + (\frac{q^2}{2m})} \tag{B.1}$$

The equations of motion for a_q and $a_{-q}^\dagger$ can be obtained from the time-dependent Schroedinger equation,

$$\begin{aligned}
\frac{da_q}{dt} &= \frac{i}{\hbar}[H, a_q] \\
&= \frac{i}{\hbar}[H, ub_q - vb_{-q}^\dagger] \\
&\vdots \\
&= -\frac{i}{\hbar}[(\frac{q^2}{2m} + U)a_q + Ua_{-q}^\dagger] \\
\frac{da_{-q}^\dagger}{dt} &= \frac{i}{\hbar}[(\frac{q^2}{2m} + U)a_{-q}^\dagger + Ua_q]
\end{aligned}$$

The solution of the two coupled equations yields solutions

$$\begin{aligned}
a_q(t) &= f(t)a_q(0) + g^*(t)a_{-q}^\dagger(0) \\
a_{-q}^\dagger(t) &= f^*(t)a_{-q}^\dagger(0) + g(t)a_q(0) \\
f(t) &= \cosh[\lambda t] - \frac{i}{\hbar\lambda}(\frac{q^2}{2m} + U)\sinh[\lambda t] \\
g(t) &= \frac{iU}{\hbar\lambda}\sinh[\lambda t]
\end{aligned}$$

The growth of the mode $\langle a_q a_q^\dagger \rangle(t)$ is given by

$$a_q^\dagger a_q(t) = |f|^2 a_{-q}^\dagger a_{-q} + |g|^2 a_{-q} a_{-q}^\dagger + fg a_{-q}^\dagger a_q^\dagger + gf a_q a_{-q}$$

If the initial occupation of all modes is zero, then only the second term contributes and the expression reduces to $|g|^2 = \frac{U^2}{\lambda^2}\sinh^2[\lambda t]$, which is exactly Eq. 3.9. Otherwise, it depends on all the terms, including the cross terms $\langle a_q a_{-q}\rangle$ and $\langle a^\dagger_{-q} a^\dagger_q\rangle$. These can also be calculated and here I will just give their final forms:

$$\begin{aligned}\langle a^\dagger_q a_q\rangle &= v^2 = \langle a^\dagger_{-q} a_{-q}\rangle \\ \langle a^\dagger_{-q} a^\dagger_q\rangle &= -uv = \langle a_q a_{-q}\rangle\end{aligned}$$

Finally, collating all results gives

$$a^\dagger_q a_q(t) = |f|^2 v^2 + |g|^2(v^2+1) - 2\mathcal{R}e(fg)uv \tag{B.2}$$

where

$$\begin{aligned}|f|^2 &= \cosh^2[\lambda t] + \frac{1}{\lambda^2}(\frac{k^2}{2}+U)^2\sinh^2[\lambda t] \\ |g|^2 &= \frac{U^2}{\lambda^2}\sinh^2[\lambda t] \\ \mathcal{R}e(fg) &= \frac{U}{\lambda^2}(\frac{k^2}{2}+U)\sinh^2[\lambda t]\end{aligned}$$

Appendix C

Formation of Quantum-Degenerate Sodium Molecules

This appendix contains a reprint of Ref. [19]: K.Xu, T. Mukaiyama, J.R. Abo-Shaeer, J.K.Chin, D.E. Miller, W. Ketterle, *Formation of Quantum-Degenerate Molecules*, Physical Review Letters **91**, 210402 (2003).

Formation of Quantum-Degenerate Sodium Molecules

K. Xu, T. Mukaiyama, J. R. Abo-Shaeer, J. K. Chin, D. E. Miller, and W. Ketterle
Department of Physics, MIT-Harvard Center for Ultracold Atoms, and Research Laboratory of Electronics, MIT, Cambridge, Massachusetts 02139, USA
(Received 1 October 2003; published 21 November 2003)

Ultracold sodium molecules were produced from an atomic Bose-Einstein condensate by ramping an applied magnetic field across a Feshbach resonance. More than 10^5 molecules were generated with a conversion efficiency of ~4%. Using laser light resonant with an atomic transition, the remaining atoms could be selectively removed, preventing fast collisional relaxation of the molecules. Time-of-flight analysis of the pure molecular sample yielded an instantaneous phase-space density greater than 20.

DOI: 10.1103/PhysRevLett.91.210402 PACS numbers: 03.75.Nt, 32.80.Pj, 33.80.Ps, 34.20.Cf

Atomic Bose-Einstein condensates (BEC) provide a new window into macroscopic quantum phenomena [1]. A molecular condensate could lead to a host of new scientific explorations. These include quantum gases with anisotropic dipolar interactions, tests of fundamental symmetries such as the search for a permanent electric dipole moment, study of rotational and vibrational energy transfer processes, and coherent chemistry, where reactants and products are in coherent quantum superposition states. So far, the highly successful techniques for creating atomic BEC have not led to success for molecules. Laser cooling is difficult due to the complicated level structure of molecules [2], and evaporative cooling requires the preparation of a dense gas of molecules, where elastic collisions dominate inelastic collisions.

Alternative techniques, such as buffer gas loading [3] and Stark deceleration [4], have been successful in obtaining cold molecules. Yet these methods are still far from achieving the requisite phase-space density for BEC. The difficulty in cooling molecules directly can be circumvented by creating ultracold molecules from quantum-degenerate atomic samples. This requires molecule formation without release of energy, which can be accomplished either by photoassociation [5] or by "tuning" a molecular state via a Feshbach resonance [6] to be degenerate with the atomic state. A Feshbach resonance occurs when an applied magnetic field Zeeman shifts a molecular state to zero binding energy. By ramping an external field across a Feshbach resonance from negative to positive scattering length, translationally cold molecules in high vibrational states can be created adiabatically [7–9].

The first observation of a Feshbach resonance in ultracold atoms showed a high rate of atom loss [6,10]. Theories accounted for this loss by assuming the formation of ultracold molecules [7,8,11]. These molecules were predicted to decay vibrationally in less than 100 μs due to a two-body rate coefficient of order 10^{-10} cm^3/s. Because of this, no successful attempt was made to detect a molecular signature until atom-molecule beats were observed in ^{85}Rb, lasting about 100 μs [12]. Recent fermion experiments using magnetic field sweeps have observed molecules with lifetimes approaching 1 s [13–16]. Until now, similar experiments with bosons have been carried out only during ballistic expansion [17,18]. According to theory, the decay of molecules composed of fermionic atoms is suppressed by Pauli blocking [19], whereas molecules composed of bosons decay rapidly. This could explain the low conversion efficiency of about 5% for bosons, compared to > 50% for fermions, where more adiabatic field ramps are possible.

If highly degenerate atoms (both fermionic and bosonic) are converted adiabatically to molecules, the molecules can be created at a phase-space density exceeding 2.6, the critical value at which a uniform, ideal Bose gas condenses [20]. Previous experiments [14,18,21] have measured or estimated conditions close to or around this critical phase-space density.

Here we report the production of trapped sodium molecules from an atomic BEC. The initial phase-space density of the molecular sample was measured in excess of 20. High phase-space density could only be achieved by rapidly removing residual atoms, before atom-molecule collisions caused trap loss and heating. This was accomplished by a new technique for preparing pure molecular clouds, where light resonant with an atomic transition selectively "blasted" unpaired atoms from the trap. In contrast to spatial separation via a Stern-Gerlach method [17,18], this technique can separate out the molecules faster and does not require a large difference in the magnetic moments of the atoms and molecules.

To generate the molecules, sodium condensates in the $|F = 1, m_F = -1\rangle$ state were prepared in an optical dipole trap. The radial and axial trap frequencies of $\omega_r = 2\pi \times 290$ Hz and $\omega_z = 2\pi \times 2.2$ Hz, respectively, gave Thomas-Fermi radii of $R_r = 5$ μm and $R_z = 650$ μm, and a peak density of 1.7×10^{14} cm^{-3} for 5×10^6 atoms atoms. An adiabatic radio frequency sweep was used to transfer the atoms into the $|1, 1\rangle$ state, which has a 1 G wide Feshbach resonance at 907 G [6,22].

After 1 s equilibration in the optical trap, the molecules were generated using the field ramping scheme illustrated in Fig. 1(a). An applied magnetic field was ramped in ~100 ms to 4 G below the 907 G Feshbach resonance.

 0031-9007/03/91(21)/210402(4)$20.00

The field was generated using a pair of large bias and small antibias coils. Because molecules are only created when sweeping across the resonance from negative to positive scattering length, the field was stepped up to 913 G as quickly as possible (~1 μs) to jump over the resonance with minimal atom loss. After allowing 2.5 ms for transient field fluctuation to damp out, the field was ramped down in time τ_{down}. Because of atom-molecule coupling, part of the atomic population was transferred into the molecular state following the Landau-Zener avoided crossing. With the given width of the resonance and the atomic density, we use a simple Landau-Zener model to calculate a ramp speed of $\sim 10^4$ G/s to transfer roughly half the atoms to the molecular state [7,8,11]. However, inelastic collisions led to fast decay for both the atoms and the molecules near the resonance. We found that a faster ramp speed of $\sim 10^5$ G/s(corresponding to $\tau_{\text{down}} = 50$ μs) gave optimal results. The conversion efficiency of atoms to molecules was ~4%. Slower ramp speeds resulted in a similar number of molecules, but at higher temperature [see Fig. 1(e)].

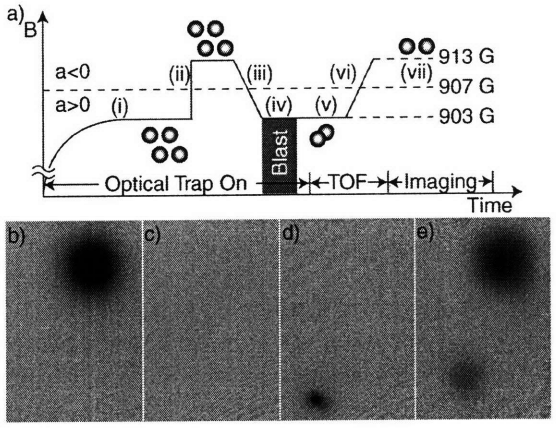

FIG. 1. (a) Experimental method for producing and detecting ultracold molecules. (i) Bose condensed atoms in an optical dipole trap are exposed to a magnetic field just below a Feshbach resonance. (ii) The field is quickly stepped through the resonance to minimize atom loss. (iii) The field is then swept back through the resonance, creating an atom-molecule mixture. (iv) Unpaired atoms are removed from the trap with resonant light, yielding a pure molecular sample. (v) The trap is switched off, allowing the molecules to expand ballistically. (vi) Finally, the magnetic field is swept back across the resonance to reconvert the molecules to atoms for imaging (vii). (b) Image of the *atomic* sample after ramping the field to produce molecules; (c) after the resonant light pulse has removed all unpaired atoms; (d) after the *molecules* ($\sim 10^5$) have been reconverted to atoms. (b),(c) were taken along the weak axis of the trap after 17 ms ballistic (time-of-flight–TOF) expansion. (e) An image showing both atomic (top) and molecular (bottom) clouds after 14 ms ballistic expansion, spatially separated by a magnetic field gradient. With 4 ms field ramp-down time, some molecules survived even without the blast pulse, but are much more heated. The field of view of each image is 1.8 mm × 1.3 mm.

The blast pulse was applied along the radial axis of the trap to minimize collisions between the escaping atoms and the molecules at rest. A 20 μs pulse of resonant light removed all atoms from the optical trap, leaving behind a pure molecular sample (see Fig. 1). At only 4 G below the Feshbach resonance, the light was still close to resonance with molecular photodissociation to low-velocity atoms, but the overlap matrix element was sufficiently diminished to leave the molecules unaffected. After a variable hold time, the optical trap was switched off and the molecules expanded ballistically for between 4 and 20 ms. The molecules were detected by converting them back to atoms with field ramp-up in $\tau_{\text{up}} = 100$ μs at the end of expansion. Varying τ_{up} between 50 μs and 4 ms did not affect the recovered atom number, though shorter τ_{up}'s recovered atoms with larger kinetic energy [23]. Thus we assume all molecules are converted back to atoms. A resonant absorption image was taken after an additional 500 μs, which allowed the imaging field to settle. The rapid conversion of molecules to atoms after a long expansion time ensured that the absorption images accurately depicted the momentum distribution of the *molecular* cloud.

Atoms and molecules were separated during the ballistic expansion by a Stern-Gerlach technique [Fig. 1(e)]. Because of trap imperfections, the large bias coils provided an additional radial gradient of the axial field of ~2.8 G/cm in the vicinity of the condensate. This value was determined from the trajectory of the falling atoms. Since the molecules have a different magnetic moment, they separate from the atoms during the ballistic expansion [Fig. 1(e)]. From the separation of the atomic and molecular clouds at different times, we determined the difference between atomic and molecular magnetic moments to be 3.2 μ_B (μ_B is the Bohr magneton), in good agreement with theory [11].

For different ramp down times τ_{down}, the time-of-flight images of the molecular cloud exhibit drastically different momentum distribution. The coldest cloud was obtained with the fastest ramp down time possible, $\tau_{\text{down}} = 50$ μs (Fig. 2). A Gaussian fit was used to determine the molecular temperature T_m and the phase-space density. Because of the rapid ramp down, the molecules had no time to adjust to the external trapping potential or any mean-field interactions. Therefore, we assume the molecules were *uniformly* created with the Thomas-Fermi profile of the original atomic BEC. The peak phase-space density is then given by

$$\text{PSD}_{\text{peak}} = \left(\frac{h}{\sqrt{2\pi k_B T_m M_m}}\right)^3 \frac{N_m}{\frac{8\pi}{15} R_r^2 R_z}, \qquad (1)$$

where h is the Planck constant, k_B is the Boltzmann constant, M_m is the molecular mass, and N_m is the number of molecules. The second factor in the equation is the peak density for a Thomas-Fermi profile.

Figure 3(a) shows the phase-space densities obtained for different holding time in the optical trap. Phase-space

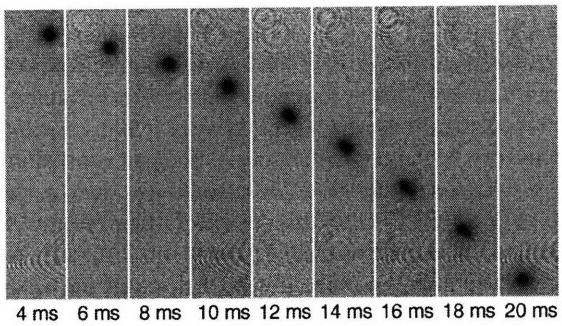

FIG. 2. Ballistic expansion of a pure molecular sample. Absorption images of molecular clouds (after reconversion to atoms) are shown for increasing expansion time after switching off the optical trap. The small expansion velocity corresponds to a temperature of ~30 nK, characteristic of high phase-space density. The images are taken along the weak axis of the trap. The field of view of each image is 3.0 mm × 0.7 mm.

densities in excess of 20 were observed, much larger than the critical value of 2.6. This demonstrates that a quantum-degenerate cloud of atoms can be transformed into a quantum-degenerate molecular gas.

The high initial phase-space density decayed rapidly (~2 ms), due to molecule loss and heating. For a pure molecular sample at a peak density of 4×10^{12} cm^{-3}, the molecule number dropped by half in 5 ms and the apparent temperature doubled in 2 ms. Since the molecules are formed in a high vibrational state with quantum number $v = 14$, losses are most likely due to vibrational relaxation. The high loss rate of the molecules is consistent with theoretically predicted two-body relaxation rate coefficients of 10^{-10} cm^3/s [9,24]. Because the loss of molecules is faster at the high densities near the bottom of the trap, it is accompanied by heating. This is in contrast to evaporative cooling, where the losses occur at the top of the trap. Such antievaporative heating gives a time constant 4 times slower than the observed heating rate. We therefore believe that the rapid increase in the apparent temperature is due to the inward motion of the molecular cloud (see below), and possibly transfer of the vibrational energy of the molecules.

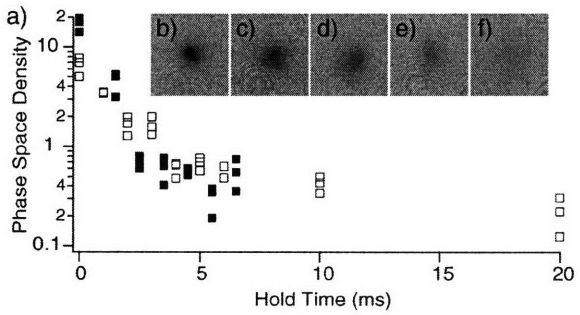

FIG. 3. Molecular phase-space density versus hold time. (a) The phase-space densities of the trapped molecules were observed to decrease significantly after a few milliseconds in the optical trap. The open and solid squares are data from two separate runs on different days. (b),(c) are absorption images of the molecular clouds after (b) 0 ms, (c) 2 ms, (d) 5 ms, (e) 10 ms, (f) 20 ms hold time in the trap. The field of view is 0.8 mm × 0.8 mm.

Our calculation of the phase-space density is conservative, since almost all errors lead to an underestimation of the value. The most critical quantity is the thermal velocity $v_{\mathrm{therm}} = \sqrt{2k_B T_m / M_m}$ obtained from the Gaussian fit of the cloud, since the phase-space density scales with the third power of v_{therm}. We determined the velocity by simply dividing the size of the cloud by the time-of-flight, without correcting for imaging resolution and initial cloud size.

Correcting for the imaging resolution of 10 μm compared to the typical cloud size of 50 μm would increase the phase-space density measurement by 6%. In addition, radial excitation of the trapped cloud (shown in Fig. 4) contributed to the size of the cloud after the ballistic expansion. From the fits, the smaller of the two Gaussian radii was used to calculate v_{therm}, assuming that the larger size was caused by radial excitations. Yet since the radial excitation can occur in two orthogonal directions, we estimate that the extracted thermal velocities were still overestimated by ~10%. We also considered magnetic focusing of the cloud due to residual field inhomogeneities. Because we use large coils (~17 cm in diameter and ~4 cm away from the condensate) to produce a homogeneous magnetic field, any residual radial curvature due to radial fields is calculated to be $\lesssim 0.1$ G/cm^2. An upper bound for the radial curvature of the axial fields was obtained from trap frequency measurements and ballistic expansion measurements as <1 G/cm^2. This can only reduce the size of the cloud by less than 2% after a typical ballistic expansion time of 17 ms.

We assume resonant absorption in determining the number of atoms. Any systematic effect such as small detuning or saturation, would lower both N_m and the Thomas-Fermi volume (proportional to $N^{3/5}$, where N is the number of condensed atoms). The net effect is an underestimate of the phase-space density. In addition, because the molecular formation process is nonlinear in

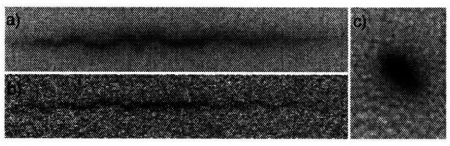

FIG. 4. Images of (a) atomic and (b) molecular clouds. These absorption images were taken after 7 ms ballistic expansion and show the axial extent of the clouds. Radial excitations in the optical trap resulting from the sudden switching of magnetic fields are manifest as snakelike patterns. Such excitations blur images (c) taken along the long axis of the trap (in 17 ms TOF), leading to an underestimate of the phase-space density. The fields of view are (a),(b) 0.6 mm × 3.2 mm, (c) 0.6 mm × 0.4 mm.

atomic density, the assumption of the atomic Thomas-Fermi volume for molecules is likely an overestimate. Furthermore, in the absence of strong mean-field repulsion (due to the much lower molecular density), the molecular cloud would not sustain the initial size of the atomic condensate [used in Eq. (1)], and shrink to a smaller size within a few milliseconds ($\sim$ radial trap period). If we assume radial thermal equilibrium while keeping the axial length fixed (as the axial trap period is 500 ms), the phase-space density would be 2 to 4 times higher than is shown in Fig. 3. To sum up, the extracted peak phase-space densities are underestimated by $\gtrsim 30\%$, and all other critical systematic effects would raise the value even further.

When a molecular cloud with high phase-space density equilibrates by elastic collisions, it should form a condensate. There is no prediction for the scattering length of the molecules, which are formed in the $|v = 14, l = 0\rangle$ state [25]. Assuming a prototypical scattering length of $100a_0$ (a_0 is the Bohr radius), we estimate the elastic collision rate between molecules to be 6 s^{-1}, which is smaller than our loss rate. Thus, the so-called ratio of good and bad collisions is smaller than 1.

Recent work on molecules composed of fermionic lithium [14,15] and potassium [26] atoms showed a dramatic increase in lifetime close to the Feshbach resonance. Theoretically, the rate of vibrational relaxation should decrease with the scattering length a_s as $\propto a_s^{-2.55}$ due to Pauli blocking [19]. In contrast, for molecules composed of bosonic atoms, the rate should increase proportionally to a_s [27]. On the other hand, the elastic collision rate is proportional to a_s^2, so for large a_s one would expect the ratio of good-to-bad collisions to exceed one. However, if this condition is met at loss rates faster than the trap frequency, the cloud can only establish local, not global equilibrium.

Whether our molecular sample is a condensate depends on one's definition of BEC. If phase-space density in excess of 2.6 (corresponding to a diagonal matrix element of the single-particle density matrix larger than 1) is sufficient, then one may regard a short-lived atom-molecule superposition state [12] as a molecular BEC. However, following this definition, a small excited state admixture in an optically trapped BEC would qualify as BEC of electronically excited atoms. If one asks for the additional requirement of a pure molecular sample, we have achieved that in this work. Another definition would require phase coherence, which could again be observed even in short-lived samples. Should one also require a lifetime of the degenerate sample exceeding the collision time (to achieve local equilibrium), the trap period (to achieve global equilibrium), or the inverse mean-field energy (the typical dynamic timescale)? In our opinion, BEC requires thermal equilibrium. High phase-space density is necessary, but not sufficient.

In conclusion, we have created a quantum-degenerate gas of 10^5 cold sodium molecules with a phase-space density >20. This was achieved with a fast magnetic field sweep through a Feshbach resonance, followed by quick removal of the remnant atoms with resonant light. This purification was necessary to avoid heating and decay of the molecules through inelastic collision processes. These processes could also be avoided by loading the atomic BEC into an optical lattice in the Mott-insulator phase with a filling factor of 2 [28,29] which, after sweeping the magnetic field through the Feshbach resonance, would result in a long-lived sample of isolated molecules.

The authors would like to acknowledge M. Xue for experimental assistance with the project. We also thank A. E. Leanhardt and M.W. Zwierlein for their critical reading of the manuscript. This research is supported by NSF, ONR, ARO, NASA, and the David and Lucile Packard Foundation.

[1] *Bose-Einstein Condensation in Atomic Gases*, Proceedings of the International School of Physics "Enrico Fermi," Course CXL, edited by M. Inguscio *et al.* (IOS Press, Amsterdam, 1999).
[2] J. T. Bahns *et al.*, J. Chem. Phys. **104**, 9689 (1998).
[3] J. D. Weinstein *et al.*, Nature (London) **395**, 148 (1998).
[4] H. L. Bethlem *et al.*, Phys. Rev. Lett. **83**, 1558 (1999).
[5] R. Wynar *et al.*, Science **287**, 1016 (2000).
[6] S. Inouye *et al.*, Nature (London) **392**, 151 (1998).
[7] F. H. Mies *et al.*, Phys. Rev. A **61**, 022721 (2000).
[8] F. A. van Abeelen and B. J. Verhaar, Phys. Rev. Lett. **83**, 1550 (1999).
[9] V. A. Yurovsky *et al.*, Phys. Rev. A **60**, R765 (1999).
[10] J. Stenger *et al.*, Phys. Rev. Lett. **82**, 2422 (1999).
[11] V. A. Yurovsky and A. Ben-Reuven, Phys. Rev. A **67**, 043611 (2003).
[12] E. Donley *et al.*, Nature (London) **417**, 529 (2002).
[13] C. A. Regal *et al.*, Nature (London) **424**, 47 (2003).
[14] J. Cubizolles *et al.*, cond-mat/0308018.
[15] S. Jochim *et al.*, cond-mat/0308095.
[16] K. E. Strecker *et al.*, Phys. Rev. Lett. **91**, 080406 (2003).
[17] S. Dürr *et al.*, cond-mat/0307440.
[18] J. Herbig *et al.*, Science **301**, 1510 (2003).
[19] D. S. Petrov *et al.*, cond-mat/0309010.
[20] K. Huang, *Statistical Mechanics* (Wiley, New York, 1987).
[21] R. Grimm, C. Salomon, and C. A. Regal, at EURESCO Conference on Bose-Einstein Condensation, San Feliu de Guixols, Spain, September 2003.
[22] F. A. van Abeelen and B. J. Verhaar, Phys. Rev. A **59**, 578 (1999).
[23] T. Mukaiyama *et al.* (to be published).
[24] P. Soldán *et al.*, Phys. Rev. Lett. **89**, 153201 (2002).
[25] A. J. Moerdijk, B. J. Verhaar, and A. Axelsson, Phys. Rev. A **51**, 4852 (1995).
[26] C. A. Regal *et al.*, cond-mat/0308606.
[27] D. S. Petrov (private communication).
[28] M. Greiner *et al.*, Nature (London) **415**, 39 (2002).
[29] D. Jaksch *et al.*, Phys. Rev. Lett. **89**, 040402 (2002).

Appendix D

Experimental Setup

This appendix contains the blueprints for building the new BEC II machine.

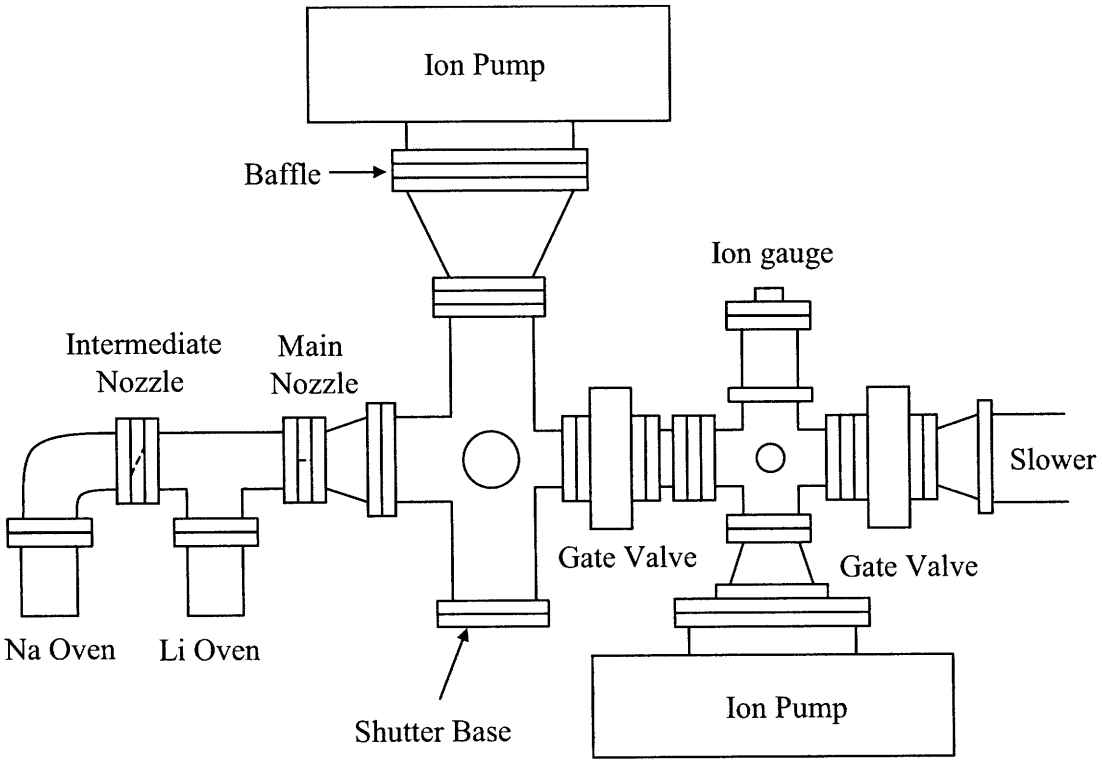

Side View

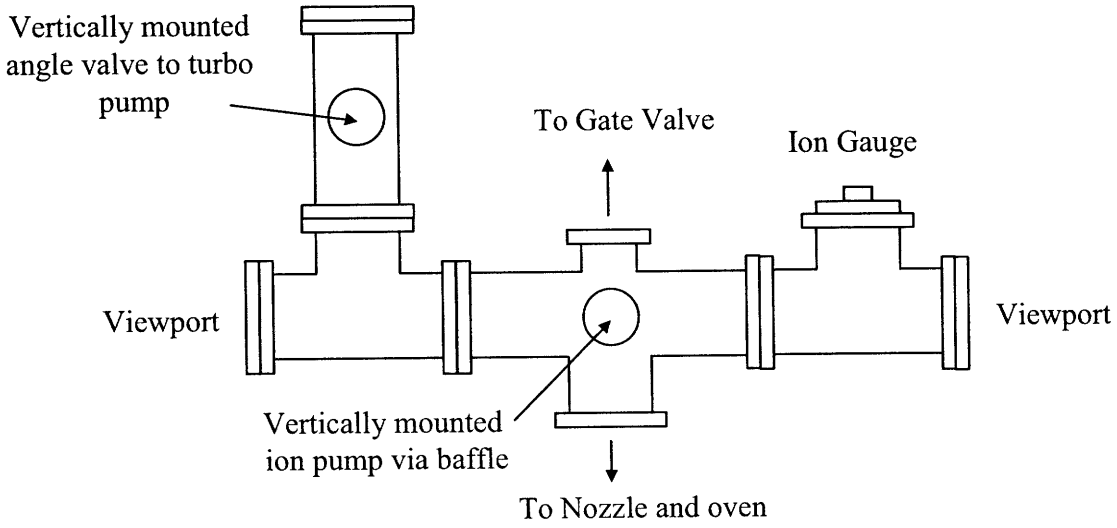

Top View

Figure D-1: Schematic of the new BEC II machine.

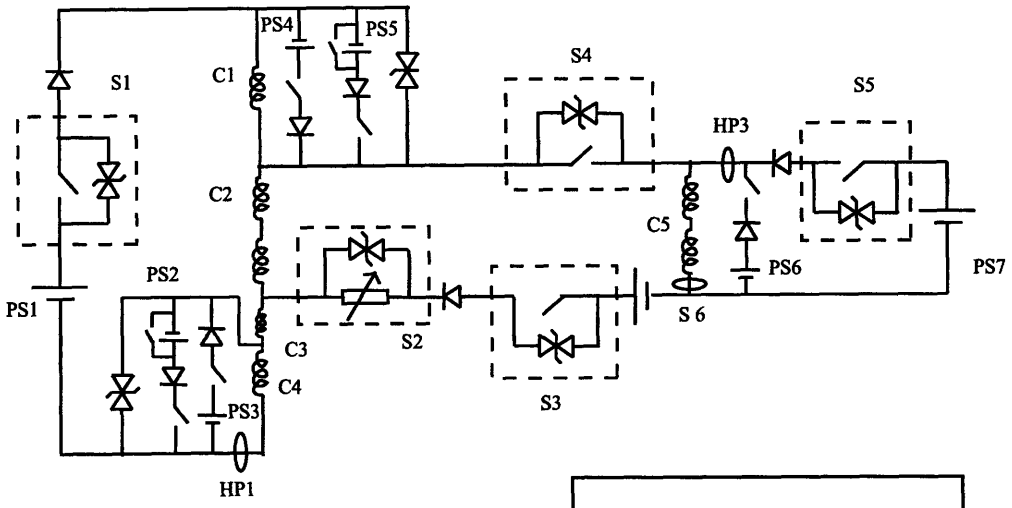

Bias and Curvature Coil Wiring Diagram

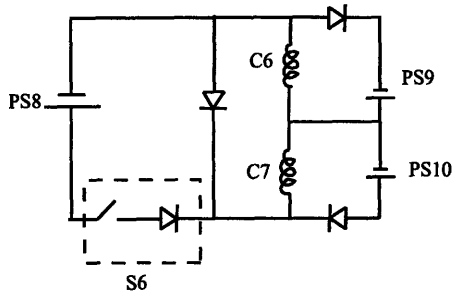

Gradient Coil Wiring Diagram

C: Coils
1, 4: Pinch (Curvature)
2: AntiBias (Feshbach)
3: Mysterious Black Coil, laser side
5: Bias (Feshbach)
6,7: Gradient (Ioffe bars)

PS: Power supply
1: Curvature
2: - Laser Pinch
3: + Laser Pinch
4: Sink Pinch
5: Big Sink Pinch
6: T-axis
7: Bias
8: Gradient
9: Top Ioffe
10: Bottom Ioffe

S: Switch (IGBT)
1: Curvature
2: Variable (analog) IGBT
3: Feshbach (main)
4: Feshbach (aux)
5: Bias

HP: Hall Probes
1: Curvature
2: Bias
3: Feshbach feedback

Figure D-2: Wiring of the various coils used for magnetic trapping and Feshbach fields.

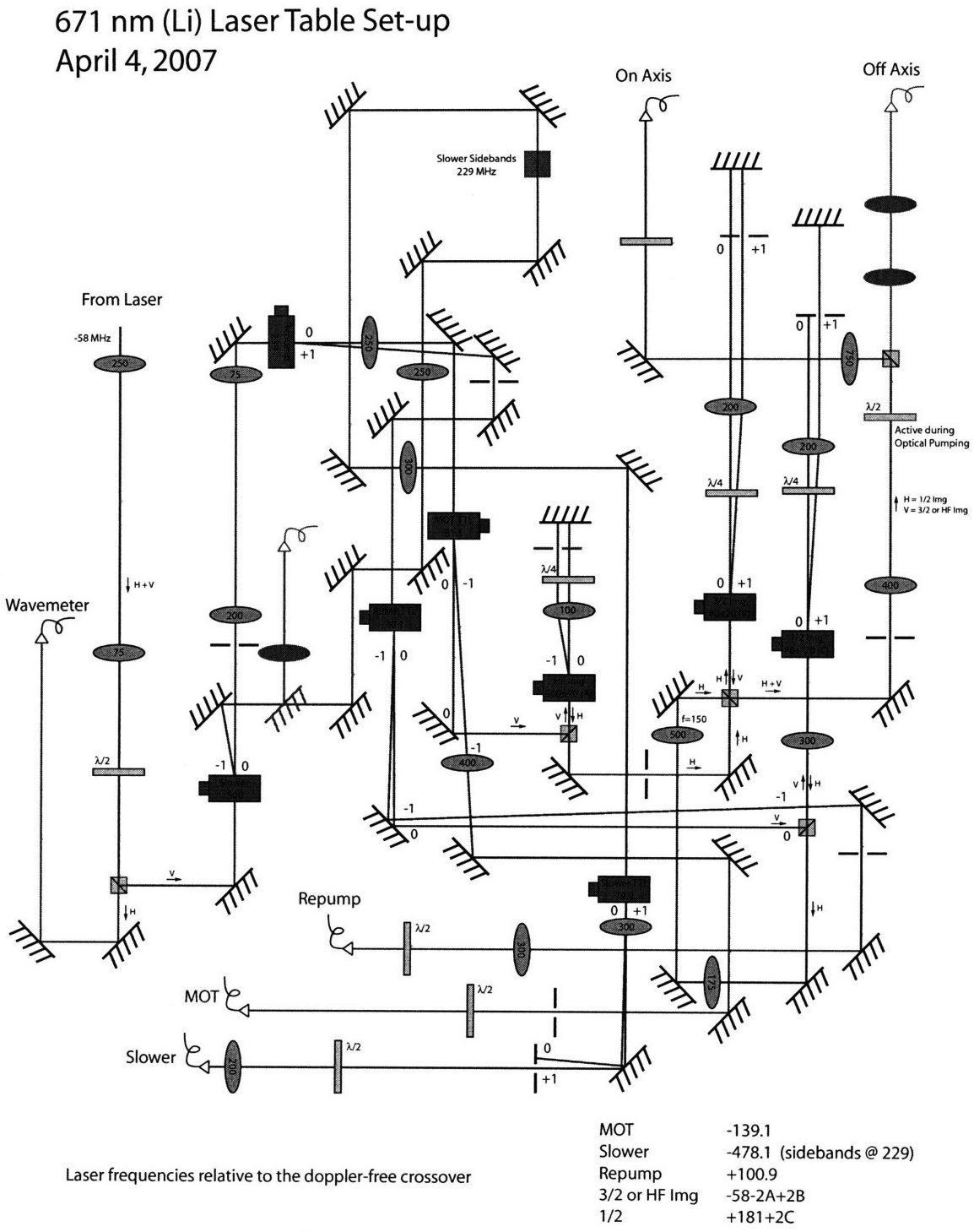

Figure D-3: Layout of the laser table for generating the different light frequencies needed for the ^{6}Li experiment.

Appendix E

Evidence for Superfluidity of Ultracold Fermions in an Optical Lattice

This appendix contains a reprint of Ref. [50]: J.K.Chin, D.E. Miller, Y. Liu, C. Stan, W. Setiawan, C. Sanner, K.Xu, W. Ketterle, *Evidence for Superfluidity of Ultracold Fermions in an Optical Lattice*, Nature **443**, 961 (2006).

LETTERS

Evidence for superfluidity of ultracold fermions in an optical lattice

J. K. Chin[1], D. E. Miller[1], Y. Liu[1], C. Stan[1]†, W. Setiawan[1], C. Sanner[1], K. Xu[1] & W. Ketterle[1]

The study of superfluid fermion pairs in a periodic potential has important ramifications for understanding superconductivity in crystalline materials. By using cold atomic gases, various models of condensed matter can be studied in a highly controllable environment. Weakly repulsive fermions in an optical lattice could undergo *d*-wave pairing[1] at low temperatures, a possible mechanism for high temperature superconductivity in the copper oxides[2]. The lattice potential could also strongly increase the critical temperature for *s*-wave superfluidity. Recent experimental advances in bulk atomic gases include the observation of fermion-pair condensates and high-temperature superfluidity[3–8]. Experiments with fermions[9–11] and bosonic bound pairs[12,13] in optical lattices have been reported but have not yet addressed superfluid behaviour. Here we report the observation of distinct interference peaks when a condensate of fermionic atom pairs is released from an optical lattice, implying long-range order (a property of a superfluid). Conceptually, this means that *s*-wave pairing and coherence of fermion pairs have now been established in a lattice potential, in which the transport of atoms occurs by quantum mechanical tunnelling and not by simple propagation. These observations were made for interactions on both sides of a Feshbach resonance. For larger lattice depths, the coherence was lost in a reversible manner, possibly as a result of a transition from superfluid to insulator. Such strongly interacting fermions in an optical lattice can be used to study a new class of hamiltonians with interband and atom–molecule couplings[14].

Previous experiments showing long-range phase coherence in Bose–Einstein condensates (BECs) and in fermion superfluids used ballistic expansion to observe the interference of two independent condensates[15], vortex lattices[8,16,17] or interference peaks after release from an optical lattice[18,19]. However, for strongly interacting fermions, elastic collisions can change the momentum distribution and wash out interference peaks. For an initially superfluid cloud, such dissipative dynamics corresponds to superfluid flow faster than the critical velocity. Consistent with this expectation is the observation that a strongly interacting Fermi superfluid initially containing distinct momentum components yielded a broad diffuse cloud after expansion (Fig. 1). This issue was addressed by using a magnetic field ramp that quickly increased the detuning from a Feshbach resonance, taking the system out of the strongly interacting regime and enforcing ballistic expansion. In previous studies of strongly interacting Fermi gases, magnetic field sweeps were applied to prevent fermion pairs above the Feshbach resonance from dissociating[6,7,20]. In contrast, our experiment required a magnetic field sweep both above and below the Feshbach resonance to avoid elastic collisions.

Our experiments used a balanced mixture of ^{6}Li fermions in the two lowest hyperfine states. Evaporative cooling produced a nearly pure fermion pair condensate that was adiabatically loaded into a three-dimensional optical lattice. A broad Feshbach resonance centred at 834 G enabled tuning of the interatomic interactions over a wide range. On resonance, a bound molecular state becomes degenerate with the open atomic scattering channel, leading to a divergence in the scattering length a. Here we explore the region of strong interactions, also known as the BEC–BCS (Bardeen–Cooper–Schrieffer) crossover, in which the magnitude of the interaction parameter $|k_F a|$ is greater than unity, and k_F is defined as the peak Fermi wavevector of a two-component non-interacting mixture of ^{6}Li atoms. In the crossover region, pairing occurs as a result of many-body interactions. Below resonance, for strong interactions, the bare two-body state has a bond length larger than the interatomic spacing and is irrelevant. In a lattice, atom pairs above and below the resonance can be confined to one lattice site[11], and crossover physics may require an occupation larger than or equal to one.

The peak pair filling factor of the lattice was about unity. At this density in the bulk, the fermion pair size is on the order of $1/k_F = 170$ nm, comparable to the lattice spacing of 532 nm. To probe the momentum distribution, we ramped the magnetic field out of the strongly interacting regime as fast as technically possible (about 150 μs) and then turned off the confining potential. Absorption

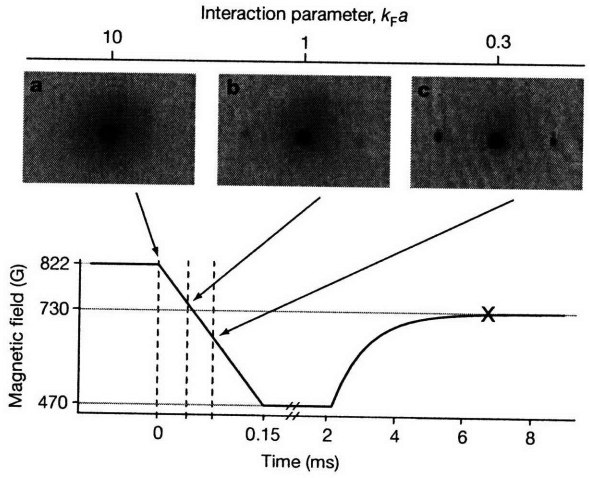

Figure 1 | Dissipative collisions during expansion of a strongly interacting fermionic superfluid. The schematic shows the time sequence of the magnetic field ramp used throughout this paper. A one-dimensional optical standing wave was pulsed onto the superfluid at different magnetic fields B_p (indicated by arrows at 822 G (**a**), 749 G (**b**) and 665 G (**c**)) during expansion, creating particles at twice the photon recoil[30]. Absorption images taken at the time marked with the cross show distinct momentum peaks only at magnetic fields $B_p \leq 750$ G, where $k_F a \leq 1$. At higher magnetic fields, the peaks blurred into a broad diffuse cloud as a result of the larger collision cross-section.

[1]Department of Physics, MIT-Harvard Center for Ultracold Atoms, and Research Laboratory of Electronics, Massachusetts Institute of Technology, Cambridge, Massachusetts 02139, USA. †Present address: Department of Chemistry and Chemical Biology, Harvard University, Cambridge, Massachusetts 02138, USA.

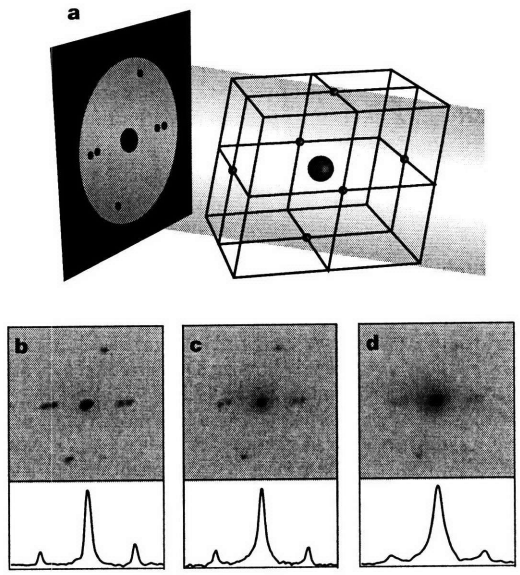

Figure 2 | Observation of high-contrast interference of fermion pairs released from an optical lattice below and above the Feshbach resonance. **a**, The orientation of the reciprocal lattice, also with respect to the imaging light. **b–d**, Interference peaks are observed for magnetic fields of 822 G (**b**), 867 G (**c**) and 917 G (**d**). The lattice depth for all images is $5E_r$, and each image is the average of three shots. The field of view is 1 mm × 1 mm. Density profiles through the vertical interference peaks are shown for each image.

images taken after 6.5 ms of expansion reveal sharp peaks at the reciprocal lattice vectors—the signature of long-range coherence, a strong indicator for superfluidity.

We observed these interference peaks at magnetic fields both above and below the Feshbach resonance (Fig. 2). The six first-order diffracted peaks are clearly visible around the zero momentum fraction and their positions correspond to the expected momentum quanta of $2\hbar k_L$ carried by molecules of mass $2m$, where k_L is the lattice wavevector. At high magnetic fields (Fig. 2d) the visibility of the interference peaks decreased and some additional heating was observed. This degradation could be due to a higher fraction of thermal atoms as we approached the BCS limit, but it was not studied in detail.

The narrow interference peaks clearly reveal the presence of a macroscopic wavefunction possessing long-range phase coherence. The separation between the interference peaks relative to their width gives an estimate of the coherence length of about ten lattice sites. This estimate is a lower bound, because effects of finite resolution and mechanisms of residual broadening have been neglected. With unity occupation, and in the absence of any discernible background at magnetic fields near the Feshbach resonance, this implies a minimum phase space density of 10^3 and shows that our samples are deep in the quantum-degenerate regime. In previous studies of ultracold Bose and Fermi gases, the appearance of a condensate fraction and long-range phase coherence was shown to occur concurrently with the possibility to excite superfluid flow[8,16,17,21]. Superfluid hydrodynamics is usually regarded as the direct proof for superfluidity. However, all reports of superfluidity of bosons in three-dimensional optical lattices have relied solely on observations of sharp interference peaks and inferred superfluidity from the established connection between long-range coherence and superfluidity[19,22]. Similarly, our observations directly show long-range coherence and indirectly show superfluidity of fermion pairs in an optical lattice.

For deep lattices, breakdown of superfluid behaviour has been observed for weakly interacting BECs of different bosonic species[19,23]. This phase transition to the Mott-insulator state occurs when on-site interactions start to suppress atom number fluctuations and the system undergoes a transition from a delocalized superfluid

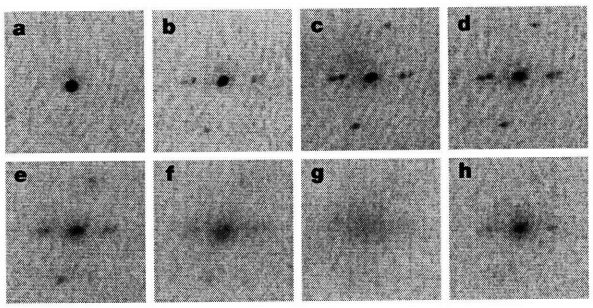

Figure 3 | Interferograms of fermion pairs released from different lattice depths V_0 at a field of 822 G. Values of V_0 are $0E_r$ (**a**), $2.5E_r$ (**b**), $4E_r$ (**c**), $5E_r$ (**d**), $6E_r$ (**e**), $7E_r$ (**f**), $9E_r$ (**g**) and $2.5E_r$ (**h**). **a–g** were taken after an adiabatic ramp up to the final V_0, whereas **h** was taken after first ramping up to $10E_r$ before ramping down to $2.5E_r$.

described by a macroscopic wavefunction to a product of Wannier states tightly localized at each lattice site. Experimentally, this is manifested as a smearing of the distinct $2\hbar k_L$ interference peaks.

Figure 3 shows the change in the coherence properties when the lattice depth was increased. The interference peaks became more pronounced initially, because of increased modulation of the wavefunction. The interference peaks began to smear out, rapidly giving way to a featureless cloud, beyond a critical lattice depth $V_c \approx 6E_r$, where $E_r = \hbar^2 k_L^2/4m = h \times 15$ kHz is the recoil energy. This indicates that all phase coherence had been lost. On subsequent ramping down of the lattice, interference peaks became visible again (Fig. 3h), showing reversibility of the lattice ramp.

We repeated this sequence for a wide range of initial magnetic fields, both above and below the resonance, and observed the same marked change in the interference pattern. Figure 4 displays the peak optical density of the interference peaks for different lattice depths at representative fields. Across all fields, the sharp decrease in peak optical density occurred between $5E_r$ and $6E_r$. A further increase in the magnetic field resulted in decreasing overall visibility, until interference peaks could no longer be observed regardless of lattice depth.

The loss of phase coherence with increasing lattice depth is consistent with the qualitative description of the superfluid to Mott-insulator transition. However, the usual single-band description is no longer applicable, because in the strong-coupling regime the on-site interaction strength should be comparable to the band gap $\hbar\omega$, where ω is the onsite trap frequency. Furthermore, Pauli blocking forbids the multiple occupation of the lowest state of an

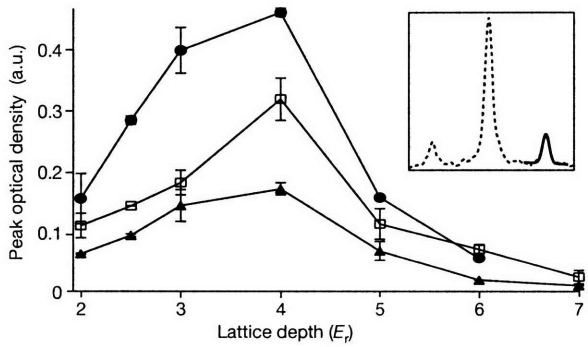

Figure 4 | Peak optical density of interference peaks for increasing lattice depths at different magnetic fields. Values of magnetic fields are 842 G (filled circles), 892 G (open squares) and 942 G (filled triangles). Peak optical densities were estimated from fits to the peaks, including background subtraction. The inset shows a sample density profile of the central and one pair of interference peaks (dotted line), with a bimodal fit to one side peak (solid line). *E*ach point is the average of three different images with six interference peaks per image. *E*rror bars show s.d.

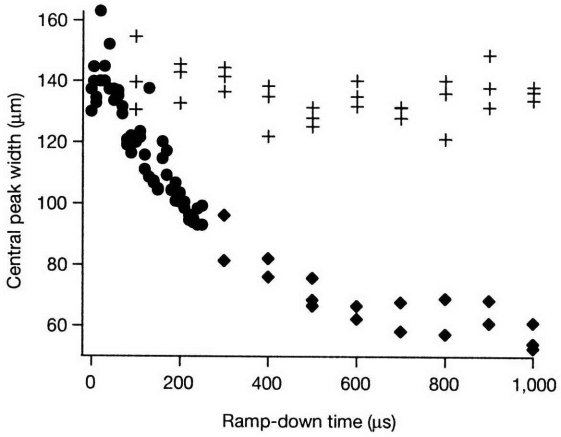

Figure 5 | Restoring coherence from a deep lattice. The width of the central peak is used as a measure of phase coherence after an adiabatic ramp up to $8E_r$, followed by a fast ramp down to $2.5E_r$ at a fixed magnetic field of 822 G. Filled circles were extracted with the use of a gaussian fit, and diamonds with a bimodal fit. Also plotted for comparison is the gaussian width of the central peak for a dephased sample, in which a field gradient was applied during the ramp up of the lattice (crosses). All points were taken for 6.5 ms time of flight.

individual lattice site by identical fermions, and modification of the single-particle tunnelling rate is expected as a result of virtual pair-breaking transitions[14]. One may still be tempted to use the standard bosonic Hubbard model and estimate the critical lattice depth V_c for an assumed value of onsite interaction energy $U = \hbar\omega$ and non-interacting, single-particle tunnelling J, but the obtained $V_c \approx 3E_r$ is significantly smaller than our observation, which is in turn much smaller than the $V_c > 10E_r$ observed for weakly interacting atomic BECs[19,23]. Together with the observed insensitivity of V_c to the magnetic field, this shows that models based on weak interactions are inadequate.

Figure 3h shows the reversibility of the transition from a long-range coherent state to a state without strong coherence. We now study the timescale for this recoherence, by analogy with similar measurements performed across the transition from superfluid to Mott insulator in atomic BECs[19]. Figure 5 shows that phase coherence was restored on a submillisecond timescale, on the order of the single-particle tunnelling time of about 500 μs (for a shallow lattice of $2.5E_r$). When the same lattice ramp sequence was applied to a superfluid that had been dephased by a magnetic field gradient[19], the system did not regain phase coherence on the timescales that we probed. Evaporative cooling is therefore negligible during this time. The short recoherence time of the condensate is evidence that the system stayed in its ground state or at least in a low-entropy state when the lattice was ramped up.

Figure 5 also provides evidence that the system could not recohere during the 150-μs magnetic field ramp. In Fig. 3h, the central peak is well fitted by a bimodal distribution with a width of 35 μm, in clear contrast to the gaussian width of 105 μm obtained from Fig. 5 after 150 μs. We therefore conclude that the observed interference patterns in Fig. 1 reflect the coherence of the cloud at the initial magnetic field, in the strongly interacting regime.

We have shown long-range phase coherence of fermion pairs in an optical lattice in the BEC–BCS crossover region by observing sharp interference peaks during ballistic expansion. This indicates that we have achieved *s*-wave pairing and superfluidity in a lattice potential. Further studies will reveal how the pair wavefunction is affected by confinement[24], and whether the lattice shifts the BEC–BCS crossover away from the Feshbach resonance[25]. The loss of coherence during the lattice ramp up and the rapid recoherence are characteristic of a Mott insulator. However, definitive proof will require a better understanding of the unitarity-limited interactions in such a Fermi system. Recent theoretical work[14,26] predicts that strongly interacting fermions in an optical lattice feature multiband couplings and next-neighbour interactions and can realize the important t–J and magnetic XXZ models of condensed-matter theory. This demonstrates that such atomic systems are an ideal laboratory for the exploration of novel condensed-matter physics.

METHODS

Clouds of superfluid fermion pairs were created in a new experimental setup[27,28] by using techniques similar to those described elsewhere[8]. In brief, a combination of laser cooling and sympathetic cooling of spin-polarized fermions by bosonic ^{23}Na was followed by a spin transfer to create a two-component Fermi gas, allowing further cooling through direct evaporation of the fermions. As the fermions cooled, they formed pairs that Bose-condensed.

Estimates of the scattering length, and hence the interaction parameter, from the magnetic field were obtained with $a(B) = -1{,}405a_0[1 + 300/(B - 834)][1 + 0.0004(B - 834)]$ (ref. 29), where B is measured in gauss and a_0 is the Bohr radius. The calibration of the magnetic field in our system had an uncertainty of about 5 G.

Evaporation was performed at a magnetic field of 822 G, at which strong interactions permitted efficient evaporation. An estimated average final number of $N \approx 2 \times 10^5$ ^{6}Li pairs and harmonic trapping frequencies of $\nu_{x,y,z} = (270,340,200)$ Hz gave a trap depth of 1.7 μK and a Fermi energy of $E_F = k_B \times 1.4\,\mu K$, where $E_F = \hbar\bar{\omega}(6N)^{1/3}$ and $\bar{\omega}$ is the average trapping frequency. After evaporation, the magnetic field was brought to a desired value B_0 in 20 ms and the condensate was allowed to equilibrate for a further 200 ms. Before ramping to values of B_0 on the BCS side, we also recompressed the optical trap to (340,440,270) Hz and 2.2 μK depth in 100 ms to accommodate the larger Fermi clouds above the resonance[7].

A three-dimensional optical lattice was formed from three optical standing waves, oriented such that the resulting unit cell had a sheared cubic structure, with one axis tilted about 20° from the normal for reasons of optical access (see Fig. 1a)[23]. The incident laser beams were focused down to the condensate with waists of about 90 μm, then retroreflected and overlapped at the condensate to generate the standing-wave potentials. All lattice light was derived from a 1,064-nm single-frequency fibre laser, and each beam was detuned by tens of MHz with respect to the others to eliminate interference between different beams.

The lattice potential was imposed on the condensate by adiabatically increasing the intensity of the laser beams to a variable final value V_0. The calibration of V_0 had an uncertainty of about 20%. A simple linear ramp with a constant rate dV_0/dt of $0.5E_r\,ms^{-1}$ was used unless otherwise specified. This satisfies the inter-band adiabaticity condition of $dV_0/dt \ll 16E_r^2/\hbar$.

Ballistic expansion for the detection of the different momentum components was provided by a magnetic field sequence (shown in Fig. 1) that quickly brought the system out of the strongly interacting regime when all confinement was switched off. During the magnetic field ramp of about 150 μs, the lattice potential was kept on. The first 2 ms of expansion took place at 470 G, at which the molecules are tightly bound, before the field was ramped back up to 730 G in the next 4.5 ms, at which the weakly bound molecules strongly absorb light near the atomic resonance line and could be observed by absorption imaging. The specific magnetic field sequence was chosen to minimize collisions within technical capabilities.

Received 29 June; accepted 25 August 2006.

1. Hofstetter, W., Cirac, J. I., Zoller, P., Demler, E. & Lukin, M. D. High-temperature superfluidity of fermionic atoms in optical lattices. *Phys. Rev. Lett.* 89, 220407 (2002).
2. Scalapino, D. J. The case for $d_{x^2-y^2}$ pairing in the cuprate superconductors. *Phys. Rep.* 250, 329–365 (1995).
3. Greiner, M., Regal, C. A. & Jin, D. S. Emergence of a molecular Bose–Einstein condensate from a Fermi gas. *Nature* 426, 537–540 (2003).
4. Jochim, S. *et al.* Bose–Einstein condensation of molecules. *Science* 302, 2101–2103 (2003).
5. Zwierlein, M. W. *et al.* Observation of Bose–Einstein condensation of molecules. *Phys. Rev. Lett.* 91, 250401 (2003).
6. Regal, C. A., Greiner, M. & Jin, D. S. Observation of resonance condensation of fermionic atom pairs. *Phys. Rev. Lett.* 92, 040403 (2004).
7. Zwierlein, M. W. *et al.* Condensation of pairs of fermionic atoms near a Feshbach resonance. *Phys. Rev. Lett.* 92, 120403 (2004).
8. Zwierlein, M. W., Abo-Shaeer, J. R., Schirotzek, A., Schunck, C. H. & Ketterle, W. Vortices and superfluidity in a strongly interacting Fermi gas. *Nature* 435, 1047–1051 (2005).

9. Modugno, G., Ferlaino, F., Heidemann, R., Roati, G. & Inguscio, M. Production of a Fermi gas of atoms in an optical lattice. *Phys. Rev. A* 68, 011601(R) (2003).
10. Köhl, M., Moritz, H., Stöferle, T., Gunther, K. & Esslinger, T. Fermionic atoms in a three-dimensional optical lattice: observing Fermi surfaces, dynamics, and interactions. *Phys. Rev. Lett.* 94, 080403 (2005).
11. Stöferle, T., Moritz, H., Gunther, K., Kohl, M. & Esslinger, T. Molecules of fermionic atoms in an optical lattice. *Phys. Rev. Lett.* 96, 030401 (2006).
12. Volz, T. *et al.* A Mott state of molecules. *Condensed Matt.* (submitted); preprint at <http://arxiv.org/abs/cond-mat/0605184> (2006).
13. Winkler, K. *et al.* Repulsively bound atom pairs in an optical lattice. *Nature* 441, 853–856 (2006).
14. Duan, L-M. Effective Hamiltonian for Fermions in an optical lattice across a Feshbach resonance. *Phys. Rev. Lett.* 95, 243202 (2005).
15. Andrews, M. R. *et al.* Observation of interference between two Bose condensates. *Science* 275, 637–641 (1997).
16. Madison, K. W., Chevy, F., Wohlleben, W. & Dalibard, J. Vortex formation in a stirred Bose–Einstein condensate. *Phys. Rev. Lett.* 84, 806–809 (2000).
17. Abo-Shaeer, J. R., Raman, C., Vogels, J. M. & Ketterle, W. Observation of vortex lattices in Bose–Einstein condensates. *Science* 292, 476–479 (2001).
18. Anderson, B. P. & Kasevich, M. A. Macroscopic quantum interference from atomic tunnel arrays. *Science* 282, 1686–1689 (1998).
19. Greiner, M., Mandel, O., Esslinger, T., Hänsch, T. W. & Bloch, I. Quantum phase transition from a superfluid to a Mott insulator in a gas of ultracold atoms. *Nature* 415, 39–44 (2002).
20. Schunck, C., Zwierlein, M. W., Schirotzek, A. & Ketterle, W. Superfluid expansion of a strongly interacting Fermi gas. *Condensed Matt.* (submitted); preprint at <http://arxiv.org/abs/cond-mat/0607298> (2006).
21. Onofrio, R. *et al.* Observation of superfluid flow in a Bose–Einstein condensed gas. *Phys. Rev. Lett.* 85, 2228–2231 (2000).
22. Schori, C., Stöferle, T., Moritz, H., Köhl, M. & Esslinger, T. Excitations of a superfluid in a three-dimensional optical lattice. *Phys. Rev. Lett.* 93, 240402 (2004).
23. Xu, K. *et al.* Sodium Bose–Einstein condensates in an optical lattice. *Phys. Rev. A.* 72, 043604 (2005).
24. Moritz, H., Stöferle, T., Gunter, K., Köhl, M. & Esslinger, T. Confinement induced molecules in a 1d Fermi gas. *Phys. Rev. Lett.* 94, 210401 (2005).
25. Koetsier, A. O., Dickerscheid, D. B. M. & Stoof, H. T. C. BEC–BCS crossover in an optical lattice. *Condensed Matt.* (submitted); preprint at <http://arxiv.org/abs/cond-mat/0604186> (2006).
26. Gubbels, K. B., Dickerscheid, D. B. M. & Stoof, H. T. C. Dressed molecules in an optical lattice. *Condensed Matt.* (submitted); preprint at <http://arxiv.org/abs/cond-mat/0605056> (2006).
27. Hadzibabic, Z. *et al.* Fifty-fold improvement in the number of quantum degenerate fermionic atoms. *Phys. Rev. Lett.* 91, 160401 (2003).
28. Stan, C. A. & Ketterle, W. Multiple species atom source for laser-cooling experiments. *Rev. Sci. Instrum.* 76, 063113 (2005).
29. Bartenstein, M. *et al.* Precise determination of ^{6}Li cold collision parameters by radio-frequency spectroscopy on weakly bound molecules. *Phys. Rev. Lett.* 94, 103201 (2004).
30. Gould, P. L., Ruff, G. A. & Pritchard, D. E. Diffraction of atoms by light: the near-resonant Kapitza–Dirac effect. *Phys. Rev. Lett.* 56, 827–830 (1986).

Acknowledgements We thank E. Demler, Z. Hadzibabic and M. Zwierlein for discussions. This work was supported by the NSF, the Office of Naval Research and NASA.

Author Information Reprints and permissions information is available at www.nature.com/reprints. The authors declare no competing financial interests. Correspondence and requests for materials should be addressed to J.K.C. (jitkee@mit.edu).

Appendix F

Critical Velocity of a Superfluid Fermi Gas in the BEC-BCS crossover

This appendix contains a reprint of Ref. [50]: D.E. Miller, J.K.Chin, Claudiu Stan, Yingmei Liu, Christian Sanner, Widagdo Setiawan, W. Ketterle, *Critical Velocity of a Superfluid Fermi Gas in the BEC-BCS crossover*, Physical Review Letters **90**, 160405 (2003).

Critical velocity for superfluid flow across the BEC-BCS crossover

D. E. Miller, J. K. Chin, C. A. Stan*, Y. Liu, W. Setiawan, C. Sanner and W. Ketterle †
Department of Physics, MIT-Harvard Center for Ultracold Atoms, and Research Laboratory of Electronics, MIT, Cambridge, MA 02139
(Dated: July 17, 2007)

Critical velocities have been observed in an ultracold superfluid Fermi gas throughout the BEC-BCS crossover. A pronounced peak of the critical velocity at unitarity demonstrates that superfluidity is most robust for resonant atomic interactions. Critical velocities were determined from the abrupt onset of dissipation when the velocity of a moving one dimensional optical lattice was varied. The dependence of the critical velocity on lattice depth and on the inhomogeneous density profile was studied.

PACS numbers: 03.75.Kk, 03.75.Lm, 03.75.Ss

The recent realization of the BEC-BCS crossover in ultracold atomic gases [1] allows one to study how bosonic superfluidity transforms into fermionic superfluidity. The critical velocity for superfluid flow is determined by the low-lying excitations of the superfluid. For weakly bound fermions, the (Landau) critical velocity is proportional to the binding energy of the pairs, which increases monotonically along the crossover into the BEC regime. However, the speed of sound, which sets the critical velocity for phonon excitations, is almost constant in the BCS regime, but then decreases monotonically on the BEC side, since the strongly bound molecules are weakly interacting. At the BEC-BCS crossover, one expects a rather narrow transition from a region where excitation of sound limits superfluid flow, to a region where pair breaking dominates. In this transition region, the critical velocity is predicted to reach a maximum [2, 3, 4]. This makes the critical velocity one of the few quantities which show a pronounced peak across the BEC-BCS crossover in contrast to the chemical potential, the transition temperature [5], the speed of sound [6, 7] and the frequencies of shape oscillations [8], which all vary monotonically.

In this paper, we report the first study of critical velocities across the BEC-BCS crossover, where a Feshbach resonance allows the magnetic tuning of the atomic interactions, and find that superfluid flow is most robust near the resonance. Our observation of a pronounced maximum of the critical velocity is in agreement with the predicted crossover between the two different mechanisms for dissipation.

Critical velocities have been determined before in atomic BECs perturbed by a stirring beam [9, 10, 11] as well as by a 1D moving optical lattice [12]. In both cases, the inhomogeneous density of the harmonically trapped sample had to be carefully accounted for in order to make quantitative comparisons to theory. Here we mitigate this problem by probing only the central region of our sample with a tightly focused moving lattice formed from two intersecting laser beams. For decreasing lattice depths, the critical velocity increases and, at very small depths, approaches a value which is in agreement with theoretical predictions.

In our experiments, we first create a superfluid of ^{6}Li pairs according to the procedure described in previous work [13]. Forced evaporative cooling of an even mixture of the two lowest hyperfine states is performed at a magnetic field of 822 G, on the BEC side of a broad Feshbach resonance centered at $B_0 = 834$ G. This results in a nearly pure Bose-Einstein condensate of $N \approx 5 \times 10^5$ pairs in a cross optical dipole trap with harmonic trapping frequencies $\nu_{x,y,z} = (65, 45, 50)$ Hz. The Fermi energy of the system is $E_F = h\bar{\nu}\,(6N)^{1/3} = h \times 7.6$ kHz. To form the moving lattice, we focus two phase-locked 1064 nm laser beams to intersect at the sample with an angle of $\sim 90°$ (see Figure 1). The resulting 1D lattice has a spatial period of $\lambda_L = 0.75\,\mu$m. A frequency difference between the two beams of $\Delta\nu$ causes the lattice to move with velocity $v_L = \lambda_L\,\Delta\nu$. The beams have e^{-2} waists of 20 μm and 60 μm respectively, and address a relatively homogeneous region at the center of the cloud which has Thomas-Fermi radii $R_{x,y,z} = (63, 91, 82)\,\mu$m. The minimum density at the position of the e^{-2} waist is 42% of the central density.

The lattice which necessarily varies in depth across the sample, is characterized by its peak depth V_0 specified in units of E_F or the recoil energy $E_r = h^2/(8m\lambda_L^2) = h \times 7.3$ kHz, where m is the molecular mass. The lattice depth is calibrated using Kapitza-Dirac scattering. Due to the inhomogeneity of the lattice, the uncertainty is 40%. The lattice depths explored in this work are sufficiently small such that motion induced in the laboratory frame is negligible, in contrast to [14].

The lattice moving at a constant velocity is adiabatically ramped up and held for a time t up to 2 s, after which the lattice is ramped down and all confinement is switched off. As in previous work [13], a fast magnetic field ramp is used to reduce strong interactions in order

*Present address: Department of Chemistry and Chemical Biology, Harvard University, Cambridge, Massachusetts 02138
†Website: cua.mit.edu/ketterle_group

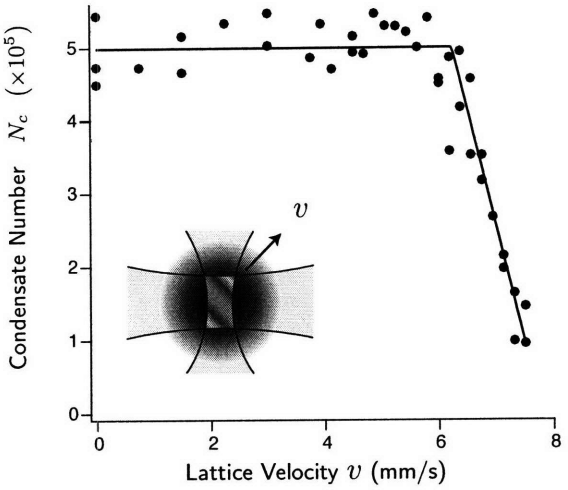

FIG. 1: Onset of dissipation for superfluid fermions in a moving optical lattice. (inset) Schematic of the experiment in which two intersecting laser beams produced a moving optical lattice at the center of an optically trapped cloud (trapping beams not shown). Number of fermion pairs which remained in the condensate N_c after being subjected to a $V_0 = 0.2\,E_F$ deep optical lattice for 500 ms, moving with velocity v_L, at a magnetic field of 822 G ($1/k_F a = 0.15$)) An abrupt onset of dissipation occurred above a critical velocity v_c, which we identify from a fit to Equation 1.

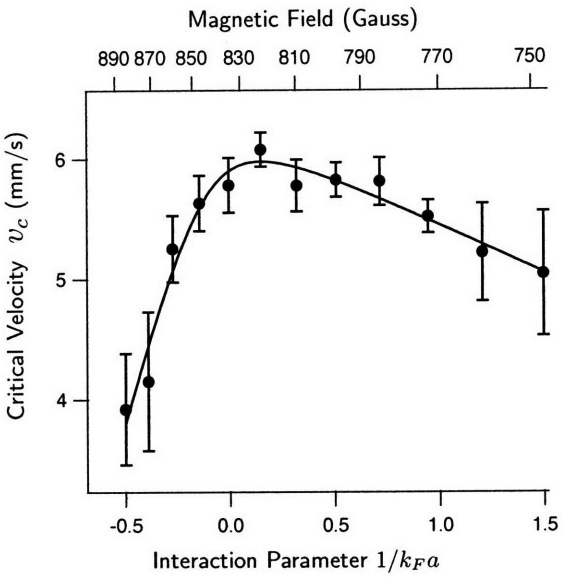

FIG. 2: Critical velocities throughout the BEC-BCS crossover. A pronounced maximum was found at resonance. Data is shown for a $V_0 = 0.2\,E_F$ deep lattice, held for t=500 ms. The solid line is a guide to the eye.

to probe the center-of-mass momentum distribution of the pairs. Subsequently, absorption imaging is done on the atomic resonance line at 730 G. A bimodal fit reveals the number of pairs remaining in the condensate N_c, providing a measure of the heating incurred during application of the moving lattice.

Figure 1 illustrates the characteristic dependence of dissipation on the velocity of the moving lattice. At low velocities, the sample is unaffected. Above some critical velocity v_c, dissipation sets in abruptly. We determine v_c from a fit of N_c to the intersection of two lines with slopes 0 and α:

$$N_{cond}(v) = N_{cond}(0) \times [1 - max(0, \alpha \times (v - vc))] \quad (1)$$

The critical velocity which we obtain from this procedure is consistent for a large range of hold times, varying by less than 15% when the hold time t is changed by a factor of 20. We explore the BEC-BCS crossover by adiabatically ramping the magnetic field to different values after evaporation and repeating the measurement as before. The crossover is parameterized by the interaction parameter $1/k_F a$, where k_F is the Fermi wavevector and a is the B-field dependent s-wave scattering length [15]. Again, we observe a threshold for dissipation.

Figure 2 shows the measured critical velocity throughout the BEC-BCS crossover. The maximum near resonance is consistent with the picture of a crossover between two different types of excitation, as discussed in the introduction, and confirms that superfluidity is most robust on resonance.

To illuminate the role of the inhomogeneous density distribution, we performed experiments in which the entire sample was perturbed by a uniform lattice. Lattice beams with 80 μm waists probed a more tightly confined sample of 2×10^5 pairs, with spatial extent $R_{TF} \simeq 37\mu$m. The onset of dissipation seen in Figure 3 is still striking, but now loss is observed at much lower lattice velocities, in spite of a larger Fermi energy $E_F = h \times 12.4$ kHz. Moreover, the onset of dissipation is slightly more gradual. When the magnetic field was varied across the Feshbach resonance, we again found a maximum of the critical velocity near resonance. The lowering of the critical velocity due to the inhomogeneous density profile is expected, since at lower density, both the speed of sound and (on the BCS side) the pairing energy decrease. Although the critical velocity should approach zero in the low density wings of the cloud, we still observe a sudden onset of dissipation at a finite velocity, similar to studies in Ref. [9, 10, 11], where a laser beam pierced through the whole condensate, but in contrast to studies reported in [12].

In the limit of vanishing perturbation, the critical velocity should be given by the Landau criterion. In Figure 4 we address the effects of a finite lattice potential in the original lattice configuration, as depicted in Figure 1. The critical velocity is shown to be a decreasing function of V_0, saturating in the limit of low lattice depth ($V_0 \leq 0.03\,E_F$). This behavior is consistent with numerical simulation [4, 16]. Measurements at the smallest lattice depths had large uncertainties, as the hold time required to observe a heating effect of the lattice

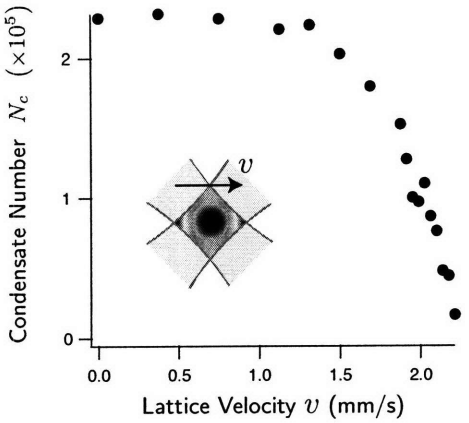

FIG. 3: Effects of density inhomogeneity on the critical velocity. A configuration in which the lattice beams (80μm) were larger than the trapped sample (37μm) results in loss in the condensate number N_c at significantly lower velocity. Data is shown for a $V_0 = 0.15\,E_F$ deep optical lattice held for 200 ms at a magnetic field of 822 G.

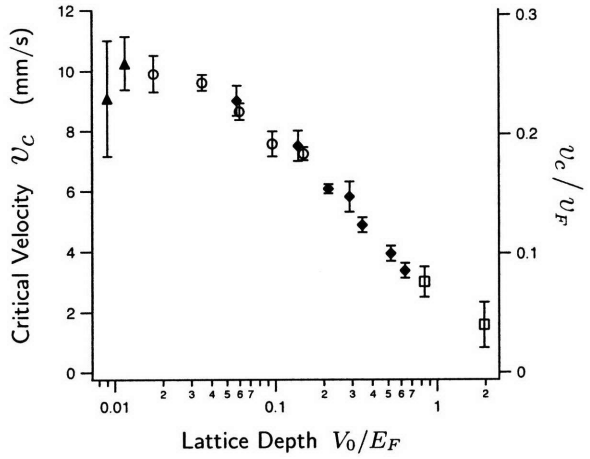

FIG. 4: Critical velocities at different lattice depths. The results show v_c to be a decreasing function of lattice depth V_0. In the limit of low V_0, v_c converges to a maximum value of 0.25 v_F. Data was taken near resonance, at 822 G ($1/k_F a = 0.15$) for hold times t = 250 ms, 500 ms, 1000 ms, 2000 ms (squares, diamonds, circles, triangles).

approached the natural lifetime of our sample. For this reason we studied the field dependence (Figure 2) at an intermediate lattice depth, where v_c was more well defined.

For comparison with theory we reference the local Fermi velocity at the trap center $v_F = v'_F\,(1+\beta)^{-1/4}$ = 39 mm/s, where $v'_F = \sqrt{2E_F/m}$ is the Fermi velocity of a non-interacting gas at the trap center, and $\beta = -0.58$ is a universal parameter characterizing unitarity limited interactions [17, 18, 19]. For vanishing lattice depth, the observed critical velocity at unitarity approaches $v_c/v_F = 0.25$. If we use the local Fermi velocity $v_{F,w}$ at the e^{-2} waist of the lattice, we obtain $v_c/v_{F,w} = 0.34$. The difference between these values indicates the uncertainty due to residual density inhomogeneity. The local speed of sound in a Fermi gas at unitarity is

$$c_s = v_{F,loc}\,(1+\beta)^{1/2}/\sqrt{3} = 0.37\,v_{F,loc}\ . \qquad (2)$$

The critical velocity for pair breaking is

$$v_{pair} = \left((\sqrt{\Delta^2+\mu^2}-\mu)/m\right)^{1/2} = 0.34\,v_{F,loc} \qquad (3)$$

with $\Delta = 0.50\,v^2_{F,loc}/2m$ [17, 19] and $\mu = (1+\beta)\,v^2_{F,loc}/2m$. These two values should provide approximate upper bounds to the critical velocity at unitarity [2, 3]. It seems natural that the combination of both excitation mechanisms lowers the critical velocity further. Within these uncertainties, and those of the density, the theoretical predictions agree with the experimental results.

Up until now, we have deferred a discussion of how the moving lattice couples to the excitations. In a pure system at zero temperature, one would expect the excitation spectrum to exhibit discrete resonances, where the perturbation couples only to modes with the k-vector of the lattice. On the other hand, at finite temperature, it is possible that the lattice drags along thermal atoms which are point-like perturbations and can create excitations at all k-vectors. Our observation that the dissipation sets in at a certain threshold velocity and increases monotonically with velocity is consistent with the participation of the thermal component.

We further elucidated the role of thermal excitations, by varying the temperature. Gradually reducing the trap depth from U_0 to U_{min}, during exposure to a lattice moving above v_c, will suppress the accumulation of a thermal component. The lifetime in this case exceeded that for a sample held at a fixed depth of either U_0 or U_{min}. For Bose-Einstein condensates, theoretical papers emphasized the role of the thermal component in the Landau damping process in a moving lattice [20, 21]. This was confirmed qualitatively in an experiment at Florence [12] in which the lifetime of the sample was drastically improved by eliminating the thermal atoms.

In our experiments, the clouds heated up during the exposure to the moving lattice. Figure 5 shows the increase in the number of thermal atoms and the loss in the total number of atoms due to evaporative cooling. In an idealized model, where density is fixed, constant dissipation would result in a linear decrease in the number of atoms due to evaporative cooling. Our data show an accelerated decrease, possibly reflecting increased dissipation due to the increasing fraction of thermal atoms. However, an accurate model should include the change in density (and therefore critical velocity) during the exposure time. Additional impurity atoms (e.g. sodium atoms) could cause dissipation even at zero temperature and would allow more controlled studies of the dissipa-

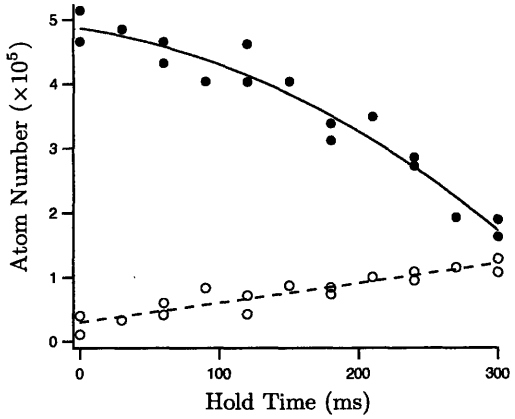

FIG. 5: Number of pairs which remained in the condensate N_c (filled circles) and thermal component N_{th} (open circles) after being held in a $V_0 = 0.35\,E_F$ deep optical lattice moving with velocity $v_L = 6$ mm/s for a variable hold time. The thermal component shows a linear increase (dashed line), whereas N_{cond} showed an accelerated loss, and is fit to a quadratic function (solid line).

tion mechanism. Unpaired atoms in clouds with population imbalance may not play this role because of phase separation effects [22].

Another possible dissipation mechanism in a lattice is the creation of two excitations through a dynamical or modulational instability. Such an instability [23] occurs already for weakly interacting particles moving through a lattice with momentum q, when they collide and scatter into states with momenta $q \pm \delta q$, analogous to optical parametric generation [24]. This process is energetically possible only above $0.5\,q_B$, where $q_B = h/2\lambda_L$ is the Bragg momentum which defines the edge of the Brillouin zone. This corresponds to a velocity $v = 11$ mm/s for fermion pairs (and twice this value for single atoms). Since the highest critical velocities we observe are slightly below this threshold, and strongly decrease already for relatively small V_0, it is very unlikely, that dynamical instabilities play a role in our experiments. Moreover, such instabilities should be strongly modified by Pauli blocking. For our ratio of local Fermi momentum to the Bragg momentum of 0.9, the first band is nearly full in the center of the cloud. For Bose-Einstein condensates, it has been recently predicted [25] and experimentally shown [14] that strong interactions can lower the threshold for the dynamical instability, close to the Mott-insulator transition. The range of 1-D lattice depths explored here ($V_0 \leq 2\,E_r$) is far from the 1D Mott-insulator regime. We have observed the loss of coherence which typically accompanies the superfluid to Mott insulation transition to occur only beyond $V_0 \simeq 25\,E_r$.

In conclusion, we have used a novel optical lattice geometry to determine critical velocities in the BEC-BCS crossover without the complications of strong density inhomogeneity. This configuration could be applied to studies in atomic Bose gases which so far have been limited by the inhomogeneous density [9, 10, 11, 12]. In addition, it would be interesting to study dynamical instabilities for fermions and the role of Pauli blocking. The authors would like to thank Aviv Keshet for experimental assistance. This research has been supported by the NSF and the Office of Naval Research.

[1] S. Giorgini, L. P. Pitaevskii, and S. Stringari, preprint condmat/0706.3360 .
[2] R. Sensarma, M. Randeria, and T.-L. Ho, Phys. Rev. Lett. **96**, 090403 (2006).
[3] R. Combescot, M. Y. Kagan, and S. Stringari, Phys. Rev. A **74**, 042717 (2006).
[4] A. Spuntarelli, P. Pieri, and G. C. Strinati, pre-print /condmat/0705.2658 .
[5] C. A. R. Sá de Melo, M. Randeria, and J. R. Engelbrecht, Phys. Rev. Lett. **71**, 3202 (1993).
[6] R. Haussmann, W. Rantner, S. Cerrito, and W. Zwerger, Phys. Rev. A **75**, 023610 (2007).
[7] J. Joseph *et al.*, Phys. Rev. Lett. **98**, 170401 (2007).
[8] A. Altmeyer *et al.*, Phys. Rev. Lett. 98, 040401 (2007) **98**, 040401 (2007).
[9] C. Raman *et al.*, Phys. Rev. Lett. **83**, 2502 (1999).
[10] R. Onofrio *et al.*, Phys. Rev. Lett. **85**, 2228 (2000).
[11] C. Raman *et al.*, J. Low Temp. Phys. **122**, 99 (2001).
[12] L. De Sarlo *et al.*, Phys. Rev. A **72**, 013603 (2005).
[13] J. Chin *et al.*, Nature **443**, 961 (2006).
[14] J. Mun *et al.*, preprint condmat/0706.3946 .
[15] M. Bartenstein *et al.*, Phys. Rev. Lett. **94**, 103201 (2005).
[16] S. Ianeselli, C. Menotti, and A. Smerzi, J. Phys. B **39**, S135 (2006).
[17] J. Carlson, S.-Y. Chang, V. R. Pandharipande, and K. E. Schmidt, Phys. Rev. Lett. **91**, 050401 (2003).
[18] G. E. Astrakharchik, J. Boronat, J. Casulleras, and S. Giorgini, Phys. Rev. Lett. **93**, 200404 (2004).
[19] J. Carlson and S. Reddy, Phys. Rev. Lett. **95**, 060401 (2005).
[20] S. Tsuchiya and A. Griffin, Phys. Rev. A **70**, 023611 (2004).
[21] S. Konabe and T. Nikuni, J. Phys. B **39**, S101 (2005).
[22] Y. Shin *et al.*, Phys. Rev. Lett. **97**, 030401 (2006).
[23] B. Wu and Q. Niu, Phys. Rev. A **64**, 061603 (2001).
[24] G. K. Campbell *et al.*, Phys. Rev. Lett. **96**, 020406 (2006).
[25] E. Altman *et al.*, Phys. Rev. Lett. **95**, 020402 (2005).

Bibliography

[1] J. G. Bednorz and K. A. Mueller. Possible high-tc superconductivity in the ba-la-cu-o system. *Z. Phys. B.*, 64:189, 1986.

[2] S. N. Bose. Plancks gesetz und lichtquantenhypothese. *Z. Phys.*, 26:178, 1924.

[3] A. Einstein. Quantentheorie des einatomigen idealen gases. *Sitzungsber. Preuss. Akad. Wiss.*, Bericht 22:261–267, 1924.

[4] F. London. Electromagnetic equations of the superconductor. *Proc. Roy. Soc. London*, Ser A:A152:24, 1935.

[5] M.H. Anderson, J.R. Ensher, M.R. Matthews, C.E. Wieman, and E.A. Cornell. Observation of bose-einstein condensation in a dilute atomic vapor. *Science*, 269:198–201, 1995.

[6] K.B. Davis, M-O. Mewes, M.R. Andrews, N.J. van Druten, D.S. Durfee, D.M. Kurn, and W. Ketterle. Bose-einstein condensation in a gas of sodium atoms. *Phys. Rev. Lett.*, 75:3969–3973, 1995.

[7] B. DeMarco and D. S. Jin. Onset of fermi degeneracy in a trapped atomic gas. *Science*, 285:1703–1706, 1999.

[8] D. M. Eagles. Possible pairing without superconductivity at low carrier concentrations in bulk and thin-film superconducting semiconductors. *Phys. Rev.*, 186:456, 1969.

[9] A. J. Leggett. Diatomic molecules and cooper pairs. In *Modern Trends in the Theory of Condensed Matter. Proceedings of the XVIth Karpacz Winter School of Theoretical Physics, Karpacz, Poland, 1980,*, pages 13–27, Karpacz, Poland, 1980. Springer-Verlag, Berlin.

[10] M. Greiner, C. A. Regal, and D. S. Jin. Emergence of a molecular boseeinstein condensate from a fermi gas. *Nature*, 426:537, 2003.

[11] S. Jochim, M. Bartenstein, A. Altmeyer, G. Hendl, S. Riedl, C. Chin, J. Hecker Denschlag, and R. Grimm. Bose-einstein condensation of molecules. *Science*, 302:2101, 2003.

[12] M. W. Zwierlein, C. A. Stan, C. H. Schunck, S. M. F. Raupach, S. Gupta, Z. Hadzibabic, and W. Ketterle. Observation of bose-einstein condensation of molecules. *Phys. Rev. Lett.*, 91:250401, 2003.

[13] C. A. Regal, M. Greiner, and D. S. Jin. Observation of resonance condensation of fermionic atom pairs. *Phys. Rev. Lett.*, 92:040403, 2004.

[14] M. W. Zwierlein, C. A. Stan, C. H. Schunck, S. M. F. Raupach, A. J. Kerman, and W. Ketterle. Condensation of pairs of fermionic atoms near a feshbach resonance. *Phys. Rev. Lett.*, 92:120403, 2004.

[15] V. Bagnato and D. Kleppner. Bose-einstein condensation in low-dimensional traps. *Phys. Rev. A*, 44:7439, 1991.

[16] A. Grlitz, J. M. Vogels, A. E. Leanhardt, C. Raman, T. L. Gustavson, J. R. Abo-Shaeer, A. P. Chikkatur, S. Gupta, S. Inouye, T. Rosenband, and W. Ketterle. Realization of bose-einstein condensates in lower dimensions. *Phys. Rev. Lett.*, 87:130402–4, 2001.

[17] B. Paredes, A. Widera, V. Murg, O. Mandel, S. Folling, I. Cirac, G. V. Shlyapnikov, T. W. Hansch, and I. Bloch. Tonks-girardeau gas of ultracold atoms in an optical lattice. *Nature*, 429:277–281, 2004.

[18] M. Greiner, O. Mandel, T. Esslinger, T. W. Hansch, and I. Bloch. Quantum phase transition from a superfluid to a mott insulator in a gas of ultracold atoms. *Nature*, 415:39–44, 2002.

[19] K. Xu, T. Mukaiyama, J.R. Abo-Shaeer, J.K. Chin, D.E. Miller, and W. Ketterle. Formation of quantum-degenerate sodium molecules. *Phys. Rev. Lett.*, 91:210402, 2003.

[20] T. Mukaiyama, J. R. Abo-Shaeer, K. Xu, J. K. Chin, and W. Ketterle. Dissociation and decay of ultracold sodium molecules. *Phys. Rev. Lett.*, 92:180402, 2004.

[21] J. R. Abo-Shaeer, D. E. Miller, J. K. Chin, K. Xu, T. Mukaiyama, and W. Ketterle. Coherent molecular optics using ultracold sodium dimers. *Phys. Rev. Lett.*, 94:040405, 2005.

[22] Jamil Abo-Shaeer. *Novel Ground States of Bose-Condensed Gases.* PhD thesis, Massachusetts Institute of Technology, 2004.

[23] Kaiwen Xu. *Effects of Interaction in Bose-Einstein Condensates.* PhD thesis, Massachusetts Institute of Technology, 2006.

[24] K. Xu, Y. Liu, J. R. Abo-Shaeer, T. Mukaiyama, J. K. Chin, D. E. Miller, W. Ketterle, K. M. Jones, and E. Tiesinga. Sodium bose-einstein condensates in an optical lattice. *Phys. Rev. A*, 72:043604, 2005.

[25] K. Xu, Y. Liu, D. E. Miller, J. K. Chin, W. Setiawan, and W. Ketterle. Observation of strong quantum depletion in a gaseous bose-einstein condensate. *Phys. Rev. Lett.*, 96:180405, 2006.

[26] H. Feshbach. A unified theory of nuclear reactions. ii. *Ann. Phys.*, 19:287–313, 1962.

[27] T. Koehler, K. Goral, and P. S. Julienne. Production of cold molecules via magnetically tunable feshbach resonances. *Rev. Mod. Phys.*, 78:1311, 2006.

[28] A.J. Moerdijk, B.J. Verhaar, and T.M. Nagtegaal. Collisions of dressed ground-state atoms. *Phys. Rev. A.*, 53:4343, 1996.

[29] M. Marinescu and L. You. Controlling atom-atom interaction at ultralow temperatures by dc electric fields. *Phys. Rev. Lett.*, 81:4596, 1998.

[30] F. Fedichev, Y. Kagan, G.V. Shlyapnikov, and J.T.M. Walraven. Influence of nearly resonant light on the scattering length in low-temperature atomic gases. *Phys. Rev. Lett.*, 77:2913, 1996.

[31] F.K. Fatemi, K.M. Jones, and P.D. Lett. Observation of optically induced feshbach resonances in collisions of cold atoms. *Phys. Rev. Lett.*, 85:4462–4465, 2000.

[32] S. Inouye, M. R. Andrews, J. Stenger, H.-J. Miesner, D. M. Stamper-Kurn, and W. Ketterle. Observation of feshbach resonances in a bose-einstein condensate. *Nature*, 392:151–154, 1998.

[33] K. E. Strecker, G. B. Partridge, and R. G. Hulet. Conversion of an atomic fermi gas to a long-lived molecular bose gas. *Phys. Rev. Lett.*, 91:080406, 2003.

[34] M. G. Kozlov and L. N. Labzowsky. Parity violation effects in diatomics. *J. Phys. B*, 28:1933, 1995.

[35] A.J. Moerdijk, B.J. Verhaar, and A. Axelsson. Resonances in ultracold collisions of ^{6}li, ^{7}li and ^{2}3na. *Phys. Rev. A*, 51:4852–4861, 1995.

[36] M. Houbiers, H.T.C. Stoof, W. I. McAlexander, and R.G. Hulet. Elastic and inelastic collisions of ^{6}li atoms in magnetic and optical traps. *Phys. Rev. A*, 57:1497, 1998.

[37] K. Dieckmann, C.A. Stan, S. Gupta, Z. Hadzibabic, C.J.Schunck, and W. Ketterle. Decay of an ultracold fermionic lithium gas near a feshbach resonance. *Phys. Rev. A*, 89:203201, 2002.

[38] J. Stenger, S. Inouye, M. R. Andrews, H.-J. Miesner, D. M. Stamper-Kurn, and W. Ketterle. Strongly enhanced inelastic collisions in a bose-einstein condensate near feshbach resonances. *Phys. Rev. Lett.*, 82:2422–2425, 1999.

[39] M. Bartenstein, A. Altmeyer, S. Riedl, R. Geursen, S. Jochim, C. Chin, J. Hecker Denschlag, R. Grimm, A. Simoni, E. Tiesinga, C. J. Williams, and P. S. Julienne. Precise determination of 6li cold collision parameters by radio-frequency spectroscopy on weakly bound molecules. *Phys. Rev. Lett.*, 94:103201, 2004.

[40] D.S. Durfee. *Dynamic properties of dilute Bose-Einstein Condensates.* PhD thesis, Massachusetts Institute of Technology, 2002.

[41] W. Setiawan. A new degenerate fermi gas apparatus, 2007. Massachusetts Institute of Technology, Undergraduate Thesis.

[42] B. deMarco. *Quantum Behavior of an Atomic Fermi Gas.* PhD thesis, University of Colorado, 2001.

[43] B. Marcelis, E. G. M. v. Kempen, B. J. Verhaar, and S. J. J. M. F. Kokkelmans. Feshbach resonances with large background scattering length: Interplay with open-channel resonances. *Phys. Rev. A*, 70:012701, 2004.

[44] M. Zwierlein. *High-Temperature Superfluidity in an Ultracold Fermi Gas.* PhD thesis, Massachusetts Institute of Technology, 2006.

[45] C. C. Bradley, C. A. Sackett, and R. G. Hulet. Bose-einstein condensation of lithium: Observation of limited condensate number. *Phys. Rev. Lett.*, 78:985–989, 1997.

[46] M. Houbiers and H. T. C. Stoof. Stability of bose condensed atomic 7li. *Phys. Rev. A*, 54:5055, 1996.

[47] R. A. Duine and H. T. C. Stoof. Explosion of a collapsing bose-einstein condensate. *Phys. Rev. Lett.*, 86:2204, 2001.

[48] E. A. Calzetta and B. L. Hu. Bose-einstein condensate collapse and dynamical squeezing of vacuum fluctuations. *Phys. Rev. A*, 68:043625, 2003.

[49] V. A. Yurovsky. Quantum effects on dynamics of instabilities in bose-einstein condensates. *Phys. Rev. A*, 65:033605, 2002.

[50] J. K. Chin, J. M. Vogels, and W. Ketterle. Amplification of local instabilities in a bose-einstein condensate with attractive interactions. *Phys. Rev. Lett.*, 90:160405, 2003.

[51] A. Gammal, T. Frederico, and L. Tomio. Critical numbers of attractive bose-einstein condensed atoms in asymmetric traps. *Phys. Rev. A*, 66:043619, 2002.

[52] J. M. Gerton, D. Strekalov, I. Prodan, and R. G. Hulet. Direct observation of growth and collapse of a bose?einstein condensate with attractive interactions. *Nature*, 408:692, 2000.

[53] J. L. Roberts, N. R. Claussen, S. L. Cornish, E. A. Donley, E. A. Cornell, and C. E. Wieman. Controlled collapse of a bose-einstein condensate. *Phys. Rev. Lett.*, 86:4211, 2001.

[54] E. A. Donley, N. R. Claussen, S. L. Cornish, J. L. Roberts, E. A. Cornell, and C. E. Wieman. Dynamics of collapsing and exploding bose-einstein condensates. *Nature*, 412:295–299, 2001.

[55] E.A. Donley, N.R. Claussen, S.T. Thompson, and C.E. Wieman. Atom-molecule coherence in a bose-einstein condensate. *Nature*, 417:529–533, 2002.

[56] C. J. Pethick and H. Smith. *Bose-Einstein Condensation in Dilute Gases.* Cambridge University Press, 2001.

[57] D.E. Miller. *Optical Lattices, Bragg scattering and all that.* PhD thesis, Massachusetts Institute of Technology, 2007.

[58] C. Samuelis, E. Tiesinga, T. Laue, M. Elbs, H. Knoeckel, and E. Tiemann. Cold atomic collisions studied by molecular spectroscopy. *Phys. Rev. A*, 63:012710, 2000.

[59] L. P. Gorkhov and T. K. Melik-Barkhudarov. *Soviet Journal of Physics JETP*, 13:1018, 1961.

[60] J. Carlson, S.-Y. Chang, V. R. Pandharipande, and K. E. Schmidt. Superfluid fermi gases with large scattering length. *Phys. Rev. Lett.*, 91:050401, 2003.

[61] K. M. O'Hara, S. L. Hemmer, M. E. Gehm, S. R. Granade, and J. E. Thomas. Observation of a strongly interacting degenerate fermi gas of atoms. *Science*, 298:2179, 2002.

[62] J. Kinast, A. Turlapov, J. E. Thomas, Q. Chen, J. Stajic, and K. Levin. Heat capacity of a strongly-interacting fermi gas. *Science*, 307:1296–1299, 2005.

[63] G. B. Partridge, W. Li, R. I. Kamar, Y. a. Liao, and R. G. Hulet. Pairing and phase separation in a polarized fermi gas. *Science*, 311:503, 2006. published online 21 December 2005 (10.1126/science.1122876).

[64] Zoran Hadzibabic. *Studies of a Quantum Degenerate Fermionic Lithium Gas.* PhD thesis, Massachusetts Institute of Technology, 2003.

[65] Subhadeep Gupta. *Experiments with Degenerate Bose and Fermi Gases.* PhD thesis, Massachusetts Institute of Technology, 2003.

[66] Claudiu Stan. *Experiments with Interacting Bose and Fermi Gases.* PhD thesis, Massachusetts Institute of Technology, 2005.

[67] Yong Wei, Ge Zhang, Chenghui Huang, Lingxiong Juang, and Min Wei. High power single wavelength 1338 nm nd:yag laser. *Optics and Laser Tech.*, 38:173–176, 2006.

[68] H. J. Metcalf and P. v. d. Straten. *Laser Cooling and Trapping.* Springer, 2001.

[69] C. A. Stan and W. Ketterle. Multiple species atom source for laser-cooling experiments. *Rev. Sci. Instr.*, 76:063113, 2005.

[70] Z. Hadzibabic, S. Gupta, C. A. Stan, C. H. Schunck, M. W. Zwierlein, K. Dieckmann, and W. Ketterle. Fifty-fold improvement in the number of quantum degenerate fermionic atoms. *Phys. Rev. Lett.*, 91:160401, 2003.

[71] M. R. Andrews, C. G. Townsend, H.-J. Miesner, D. S. Durfee, D. M. Kurn, and W. Ketterle. Observation of interference between two bose condensates. *Science*, 275:637–641, 1997.

[72] C. Chin, M. Bartenstein, A. Altmeyer, S. Riedl, S. Jochim, J. Hecker Denschlag, and R. Grimm. Observation of the pairing gap in a strongly interacting fermi gas. *Science*, 305:1128, 2004.

[73] M. W. Zwierlein, J. R. Abo-Shaeer, A. Schirotzek, C. H. Schunck, and W. Ketterle. Vortices and superfluidity in a strongly interacting fermi gas. *Nature*, 435:1047–1051, 2005.

[74] G. B. Partridge, K. E. Strecker, R. I. Kamar, M. W. Jack, and R. G. Hulet. Molecular probe of pairing in the bec-bcs crossover. *Phys. Rev. Lett.*, 95:020404, 2005.

[75] S. Gupta, Z. Hadzibabic, J. R. Anglin, and W. Ketterle. Collisions in zero temperature fermi gases. *Phys. Rev. Lett.*, 92:100401, 2004.

[76] K. Huang. *Statistical Mechanics.* Wiley, New York, 1987.

[77] D. S. Petrov, C. Salomon, and G. V. Shlyapnikov. Scattering properties of weakly bound dimers of fermionic atoms. *Phys. Rev. A*, 71:012708, 2005.

[78] Y. B. Band, M. Trippenbach, J. P. Burke Jr., and P. S. Julienne. Elastic scattering loss of atoms from colliding bose-einstein condensate wave packets. *Phys. Rev. Lett.*, 84:5462, 2000.

[79] A. P. Chikkatur, A. Gorlitz, D. M. Stamper-Kurn, S. Inouye, S. Gupta, and W. Ketterle. Suppression and enhancement of impurity scattering in a bose-einstein condensate. *Phys. Rev. Lett.*, 85:483–486, 2000.

[80] C. A. Regal and D. S. Jin. Measurement of positive and negative scattering lengths in a fermi gas of atoms. *Phys. Rev. Lett.*, 90:230404, 2003.

[81] T. Bourdel, J. Cubizolles, L. Khaykovich, K. M. F. Magalhes, S. J. J. M. F. Kokkelmans, G. V. Shlyapnikov, and C. Salomon. Measurement of the interaction energy near a feshbach resonance in a 6li fermi gas. *Phys. Rev. Lett.*, 91:020402, 2003.

[82] M. W. Zwierlein, C. H. Schunck, C. A. Stan, S. M. F. Raupach, and W. Ketterle. Formation dynamics of a fermion pair condensate. *Phys. Rev. Lett.*, 94:180401, 2005.

[83] P. L. Gould, G. A. Ruff, and D. E. Pritchard. Diffraction of atoms by light: the near–resonant kapitza–dirac effect. *Phys. Rev. Lett.*, 56:827, 1986.

[84] Y. B. Ovchinnikov, J. H. Mueller, M. R. Doery, E. J. D. Vredenbregt, K. Helmerson, S. L. Rolston, and W. D. Phillips. Diffraction of a released bose–einstein condensate by a pulsed standing light wave. *Phys. Rev. Lett.*, 83:284, 1999.

[85] M. E. Gehm, S. L. Hemmer, K. M. O'Hara, and J. E. Thomas. Unitarity-limited elastic collision rate in a harmonically trapped fermi gas. *Phys. Rev. A*, 68:011603, 2003.

[86] C. Schunck, M. W. Zwierlein, A. Schirotzek, and W. Ketterle. Superfluid expansion of a rotating fermi gas. *Phys. Rev. Lett.*, 98:050404, 2007.

[87] J.K. Chin, D.E. Miller, Y. Liu, C. Stan, W. Setiawan, C. Sanner, K. Xu, and W. Ketterle. Evidence for superfluidity of ultracold fermions in an optical lattice. *Nature*, 443:961–964, 2006.

[88] W. Hofstetter, J. I. Cirac, P. Zoller, E. Demler, and M. D. Lukin. High-temperature superfluidity of fermionic atoms in optical lattices. *Phys. Rev. Lett.*, 89:220407, 2002.

[89] R. Micnas, J. Ranniger, and S. Robaszkiewicz. Superconductivity in narrow-band systems with local nonretarded attractive interactions. *Rev Mod Phys*, 62:113 – 171, 1990.

[90] M. Kohl, H. Moritz, T. Stoferle, K. Gunther, and T. Esslinger. Fermionic atoms in a three dimensional optical lattice: Observing fermi surfaces, dynamics, and interactions. *Phys. Rev. Lett.*, 94:080403, 2005.

[91] G. Roati, E. d. Mirandes, F. Ferlaino, H. Ott, G. Modugno, and M. Inguscio. Atom interferometry with trapped fermi gases. *Phys. Rev. Lett.*, 92:230402, 2004.

[92] L. Pezze, L. Pitaevskii, A. Smerzi, and S. Stringari. Insulating behavior of a trapped fermi gas. *Phys. Rev. Lett.*, 93:120401, 2004.

[93] T. Rom, T. Best, D. v. Oosten, U. Schneider, S. Foelling, B. Paredes, and I. Bloch. Free fermion antibunching in a degenerate atomic fermi gas released from an optical lattice. *Nature*, 444:733–736, 2006.

[94] L.-M. Duan. Effective hamiltonian for fermions in an optical lattice across a feshbach resonance. *Phys. Rev. Lett.*, 95:243202, 2005.

[95] H. Zhai and T.L. Ho. Superfluid-insulator transition of strongly interacting fermi gases in optical lattices, 2007. cond-mat/arxiv:0704.2957.

[96] L.M. Duan. General hubbard model for strongly interacting fermions in an optical lattice and its phase detection, 2007. cond-mat/arxiv:0706.2161.

[97] T. Koehler, K. Goral, and P. S. Julienne. Production of cold molecules via magnetically tunable feshbach resonances. *Rev. Mod. Phys.*, 78:1311, 2006.

[98] M. Rigol and A. Muramatsu. Quantum monte carlo study of confined fermions in one-dimensional optical lattices. *Phys. Rev. A*, 69:053612, 2004.

[99] R. Roth and K. Burnett. Superfluidity and interference pattern of ultracold bosons in optical lattices. *Phys. Rev. A*, 67:031602(R), 2003.

[100] R.B. Diener, Q. Zhou, H. Zhai, and T.-L. Ho. Criterion for bosonic superfluidity in an optical lattice. *Phys. Rev. Lett.*, 98:180404, 2007.

[101] W. Yi, G.-D. Lin, and L.-M. Duan. Signal of bose-condensation in an optical lattice at finite temperature, 2007. cond-mat/arxiv:0705.4352.

[102] M. P. A. Fisher, P. B. Weichman, G. Grinstein, and D. S. Fisher. Boson localization and the superfluid-insulator transition. *Phys. Rev. B*, 40:546–570, 1989.

[103] D. Jaksch, C. Bruder, J. I. Cirac, C. W. Gardiner, and P. Zoller. Cold bosonic atoms in optical lattices. *Phys. Rev. Lett.*, 81:3108–3111, 1998.

[104] A. O. Koetsier, D. B. M. Dickerscheid, and H. T. C. Stoof. Bec-bcs crossover in an optical lattice. *Phys. Rev. A*, 74:033621, 2006.

[105] T. Stoferle, H. Moritz, K. Gunther, M. Kohl, and T. Esslinger. Molecules of fermionic atoms in an optical lattice. *Phys. Rev. Lett.*, 96:030401, 2006.

[106] T. Busch, B. G. Englert, K. Rzazewski, and M. Wilkens. Two cold atoms in a harmonic trap. *Found. of Phys.*, 28:549–559, 1998.

[107] C. H. Schunck, Y. Shin, A. Shirotzek, M. W. Zwierlein, and W. Ketterle. Pairing without superfluidity: The ground state of an imbalanced fermi mixture. *Science*, 316:867–870, 2007.

[108] G. Orso and G. V. Shlyanikov. Superfluid fermi gas in a 1d optical lattice. *Phys. Rev. Lett.*, 95:260402, 2005.

[109] P. Fulde and R. A. Ferrell. Superconductivity in a strong spin-exchange field. *Phys. Rev.*, 135:A550, 1964.

[110] A.J. Larkin and Y. N. Ovchinnikov. Inhomogeneous state of superconductors. *Zh. Eksp. Teor. Fiz.*, 47:1136, 1964.

[111] M. W. Zwierlein, Andre Schirotzek, Christian H. Schunck, and W. Ketterle. Fermionic superfluidity with imbalanced spin populations. *Science*, 311:492, 2006.

[112] G. Orso. Attractive fermi gases with unequal spin populations in highly elongated traps. *Phys. Rev. Lett.*, 98:070402, 2007.

[113] E. Altman, E. Demler, and M.D. Lukin. Probing many-body states of ultracold atoms via noise correlations. *Phys. Rev. A*, 70:013603, 2004.